MS Imaging for Small Molecule, Peptide and Protein Detection in Multilayers and Bacterial Biofilms

BY

MELVIN BLAZE MUTTIKAL THOMAS
B. Sc., St. Joseph's College, Bangalore, 2000
M. Sc., St. Joseph's College, Bangalore University, Bangalore, 2002

THESIS

Submitted as partial fulfillment of the requirements
For the degree of Doctor of Philosophy in Chemistry
in the Graduate college of the
University of Illinois at Chicago, 2012

Chicago, Illinois

Defense committee:

Prof. Luke Hanley, Chair and Advisor
Prof. Scott Shippy
Prof. Yoshitaka Ishii
Prof. Lawrence W. Miller
Dr. An Li, Public Health and Sciences

DEDICATION

I dedicate this dissertation to my family, especially…

To my dad Thomas and mom Florence for their love, support and prayers

To my Brother Naveen Silvester for moral support, encouragement and motivations

And to my Little Nephew Allen Thomas

ACKNOWLEDGEMENTS

This dissertation would not have been possible without the guidance and the help of several individuals who in one way or another contributed and extended their valuable support in the preparation and completion of this research work. First and foremost, my utmost gratitude to Dr. Luke Hanley, my dissertation advisor for his guidance as I hurdle all the obstacles in the completion of this research work. To the current and former Hanley group members, I have had the pleasure to work with for their friendship, valuable discussions and good advice. Last but not the least, my family and the one above all of us, the omnipresent God, for answering my prayers for giving me the strength to plod, thank you so much Dear Lord.

MB

TABLE OF CONTENTS

TABLE OF CONTENTS (continued)

CHAPTER PAGE

TABLE OF CONTENTS (continued)

LIST OF TABLES

TABLE PAGE

LIST OF FIGURES

FIGURE PAGE

LIST OF FIGURES (continued)

FIGURE PAGE

LIST OF FIGURES (continued)

FIGURE PAGE

LIST OF ABBREVIATIONS

AFM	Atomic force microscopy
ATR-IR	Attenuated total reflectance infrared
Br_2Y	3,5-dibromotyrosine
CFU	Colony forming unit
CHCA	α-cyano-4-hydroxycinnamic acid
DFR	Drip flow reactor
DHB	2,3-dihydroxybenzoic acid
EPS	Extracellular polysaccharide
IE	Ionization energy
IS	Internal standard
LD	Laser desorption
LDPI-MS	Laser desorption postionization mass spectrometry
LOD	Limit of detection
LOQ	Limit of quantitation
MALDI-MS	Matrix assisted laser desorption ionization mass spectrometry
MS	Mass spectrometry
NMR	Nuclear magnetic resonanace
PEM	Polyelectrolyte multilayer
QCM	Quartz crystal microbalance
ROI	Region of interest
SA	Sinapinic acid
SIMS	Secondary ion mass spectrometry
SPI	Single photon ionization
TOF	Time of flight
TSA	Tryptic soy agar
TSB	Tryptic soy broth
UV	Ultra violet
VUV	Vacuum ultraviolet
XPS	X-ray photoelectron spectroscopy

SUMMARY

A universal attribute of bacterial cells is their ability to form architecturally complex communities called biofilms. Biofilms can be broadly defined as communities of microbes associated with a solid surface which are typically enclosed in an extracellular polysaccharide matrix. The structure and composition of the bacterial biofilm has a profound influence on the properties of the solid surface to which they adhere. Based on their environment biofilms can adapt their metabolism to suit their circumstances, so even a single species biofilms can have every possible metabolic state that the genome can sustain. This influence has a beneficial effect on the bacterial community, often resulting in the phenomenon of biofilm resistant to drugs and antimicrobials because any assault from antimicrobials will find the cells of each species in a variety of phenotypes. Some phenotypes will be fast growing and some will be slow growing, some will have expressed all the genes, some will be aerobic and some anaerobic. Thus, the antimicrobial used should effectively kill them all or the survivors will grow quickly and reestablish the biofilm community.

Thus the study of bacterial biofilms as often tried to understand which bacteria adhere to what surfaces, why these bacteria adhere and how they resist elimination by treatment with a variety of antimicrobial agents. Various hypotheses have been developed for the antimicrobial resistance of biofilms including their alleged ability to inhibit the diffusion of antibiotics, physiological heterogeneity due to chemical and nutrient gradients in the biofilms and the coordinated regulation of genes via the exchange of chemical signal molecules including the process of quorum sensing.

There is a need for effective analytical techniques to verify these hypotheses. When microorganisms from a biofilm are dispersed, their antimicrobial susceptibility and other

properties associated with planktonic cells are usually rapidly restored. Thus, removing bacteria from their real biofilm community, which is the most commonly employed methodology for analysis, can result in the loss of valuable information. The ability of mass spectrometry (MS) imaging techniques based on secondary ion mass spectrometry (SIMS), matrix assisted laser desorption/ionization mass spectrometry (MALDI-MS) and laser desorption postionization mass spectrometry (LDPI-MS) to probe samples directly from intact surfaces was exploited in this thesis to study chemical distributions within biofilms. Many of these measurements were pursued as a function of spatial position within the biofilm.

Evaluating protocols on a well defined synthetic model system can be beneficial to optimize an analytical technique and addressing the issues that may arise from real samples. A polyelectrolyte multilayer (PEM) composed of high molecular weight polysaccharides chitosan and alginate representing an ideal model system that simulates the extracellular polysaccharide matrix of biofilms was used in this thesis to demonstrate depth profiling strategies using C_{60}^+ ion sputtering in conjunction with X-ray photoelectron spectroscopy.

Next a comparison of SIMS and LDPI-MS protocols to probe a small molecular analyte in this multilayer model was made to highlight the features of each technique with respect to their potential application in biofilm analysis. The small molecular analyte 3,5-dibromotyrosine (Br_2Y) and multilayers with and without adsorbed Br_2Y were analyzed by LDPI-MS. Both a 7.87 eV laser and tunable 8 – 12.5 eV synchrotron vacuum ultraviolet (VUV) radiation were used in LDPI-MS to determine that desorption of clusters from Br_2Y films allowed detection by $\leq$8 eV single photon ionization. Thermal desorption and electronic structure calculations determined the ionization energy of Br_2Y to be ~8.3±0.1 eV and further indicated that the lower ionization energies of clusters permitted their detection at $\leq$8 eV photon energies. However, single photon

ionization could only detect Br_2Y adsorbed within PEMs when using either higher photon energies or matrix addition to the sample. All samples were also analyzed by 25 keV Bi_3^+ SIMS, with the negative ion spectra showing strong parent ion signal which complemented that observed by LDPI-MS. However, the negative ion SIMS appeared strongly dependent on the high electron affinity of this specific analyte and the analyte's condensed phase environment.

The feasibility of imaging proteomics on intact *Enterococcus faecalis* bacterial biofilms by MALDI-MS was also demonstrated with minimum sample preparation A heptapeptide ARHPHPH was identified from intact biofilms and planktonic cultures of two different strains of *E. faecalis*. ARHPHPH was also imaged at the boundary of cocultured, adjacent *E. faecalis* and *Escherichia coli* biofilms, appearing only on the *E. faecalis side*. Additionally, top down and bottom up proteomic approaches were combined to identify thirteen cytosolic and membrane proteins and spatially locate them within intact *E. faecalis* biofilms by MALDI-MS. Two of these proteins, enolase and GAPDH, are glycolytic enzymes known to display multiple functions in bacterial virulence in related bacterial strains. This work illustrates a powerful approach for discovering and localizing multiple peptides and proteins within intact biofilms.

The potential of LDPI-MS imaging for small molecule quantification was also demonstrated in this thesis. The N-methylpiperazine acetamide of (MPA) ampicillin was adsorbed into multilayer surface coatings. These MPA-ampicillin spiked multilayers were then shown to inhibit the growth of *E. faecalis* biofilms that play a role in early stage infection of implant medical devices. Finally, LDPI-MS imaging using 7.87 eV single photon ionization was found to detect MPA-ampicillin with the multilayers before and after biofilm growth with the limits of quantification and detection of 0.6 and 0.3 nmoles, respectively. The capabilities of LDPI-MS imaging for small molecule quantification are compared to those of MALDI-MS.

Further, these results indicate that 7.87 eV LDPI-MS imaging should be applicable to quantification of a range of small molecular species on a variety of complex organic and biological surfaces.

I. INTRODUCTION

A. Mass Spectrometry Imaging

There is a common phrase that says “A picture is worth a thousand words”. MS imaging can take snap shot mass spectral images for hundreds of different analytes in a sample from a single analysis. Each snap shot can display a unique combination of chemical and spatial information thereby allowing a view of the same sample from different perspectives.

A variety of imaging techniques are currently used optical imaging, positron tomography, atomic force microscopy, electron microscopy and scanning tunneling microscopy. These techniques are capable of generating multidimensional images with spatial resolution sometimes approaching the atomic scale.[1-3] However, most of these imaging techniques require analyte pre-selection, labeling or specific markers and therefore are limited in their application. MS imaging potentially surpasses many of these limitations, albeit at lower spatial resolution.[2, 4] MS imaging was developed over the past two decades to obtain molecular images of a wide range of analytes from atoms to molecules including peptides, proteins, lipids, metabolites and polymers on a wide variety of samples. The cross correlation of MS imaging with other imaging techniques and its continuing improvement has attracted the attention of various fields ranging from pharmaceuticals to semiconductors.[5-7]

MS imaging can be performed in two different modes, microprobe or microscope mode, which depend on how the spatial information is obtained. Microprobe mode is the most common and the simplest MS imaging method. Microprobe mode uses a focused desorption/ionization beam with a mass spectrum acquired at each co-ordinate by either rastering the sample or desorption/ionization beam. Molecular images are then reconstructed using mass spectral data

acquired at each pixel as a function of its spatial coordinates. In microscope mode, ion optics are designed to retain the spatial origin of ions generated until they are detected by a position sensitive detector.[5]

Secondary ion mass spectrometry, matrix assisted laser desorption ionization mass spectrometry and laser desorption postionization mass spectrometry are microprobe based MS imaging techniques, with each offering different capabilities.

1. Secondary Ion Mass Spectrometry (SIMS)

Figure 1 shows schematic of a typical SIMS instrument: A sample is bombarded by a focused primary ion beam with kinetic energy ranging from 1 – 100 keV, atomic collisions transfers the energy from the primary ion beam on to analyte atoms resulting in a collisional cascade.[3, 8, 9] This cascade eventually results in ejection of secondary atoms, ions and neutral molecules. The secondary ions are then separated by a reflectron time of flight or other type of mass analyzer and detected. Ions are detected at each pixel by rastering the primary ion beam across the sample or by rastering the sample with respect to a fixed primary ion beam. Molecular images are then reconstructed from the ions detected as a function of its spatial coordinates. Current SIMS imaging instruments often rely upon liquid metal ion gun sources, which produce cluster ions such as Au_3^+ and Bi_3^+ for the primary ion beam.[10-13] Cluster ions can provide nonlinear enhancement in the signal and maintain very high spatial resolution in the sub micron range for imaging applications.[14] Sputtering a sample surface by cluster ion beam such as C_{60}^+ can also be combined with X-ray photoelectron spectroscopy (XPS) or SIMS as a tool for depth profiling studies. This enables collection of depth related chemical/molecular information from a variety of organic and inorganic materials with a depth resolution of several nanometers.[15, 16]

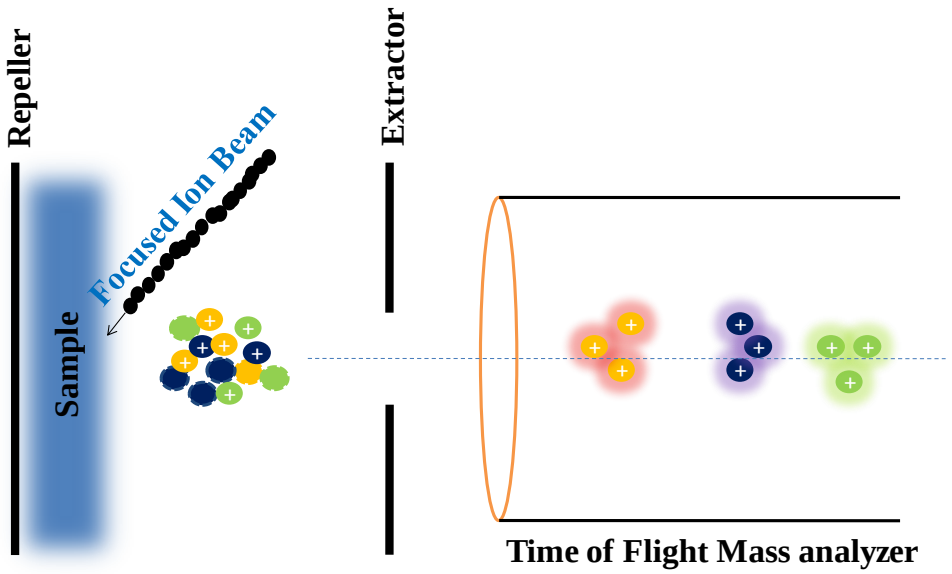

Figure 1. Schematic of a typical SIMS instrument.

2. Matrix Assisted Laser Desorption Ionization Mass Spectrometry (MALDI-MS)

Figure 2 shows schematic of a typical MALDI-MS instrument: MALDI-MS is the most versatile imaging mass spectrometry method as far as its potential application for high molecular weight analytes are concerned. It was first used to obtain molecular images of biological samples in the late 1990's. Being a soft ionization technique, it allows recording molecular images of intact large biomolecules with negligible fragmentation.[2, 17-19] For MALDI-MS imaging analysis, the sample is coated uniformly by a suitable chemical matrix such as α-cyano-4-hydroxycinnamic acid (CHCA), typically used for lower molecular weight analytes (500 to 4000 Da) or sinapinic acid (SA), typically used for higher molecular weight analytes (> 3000 Da), though several other matrices are also used in MALDI-MS. The matrix is chosen such that it is capable of absorbing the UV light in the 330 to 360 nm range of the desorption lasers commonly used in MALDI-MS. The sample is irradiated by a nanosecond pulse length UV laser and the matrix absorbs the laser energy to aid desorption and ionization of analyte compounds from the

surface. Ions are then separated based on their mass to charge ratio by a mass analyzer, often by a reflectron time of flight mass analyzer and detected.

Ions are detected at each pixel, as the desorption laser is rastered across the sample. Molecular images are then reconstructed as explained earlier.[6] Sample preparation for MALDI-MS imaging is crucial: the application of matrix to the sample prior to analysis must be standardized for consistent spectra. Matrix application for optimal MS imaging can be achieved by sublimation, dry coating, spray coating, matrix ink jet printing and manual spotting or automated spotting. Different matrix application procedures are tailored to particular kinds of analytes.[20] For example there are reports that matrix application by dry coating most favor lipid analysis, while spray coating favors protein and peptide analysis.[21]

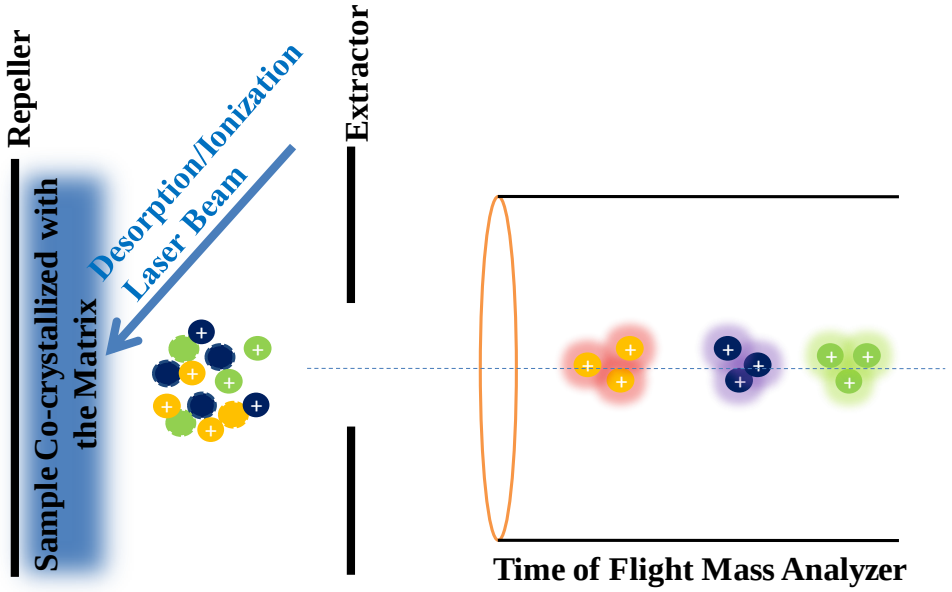

Figure 2. Schematic of a typical MALDI-MS instrument.

3. Laser Desorption Postionization Mass Spectrometry (LDPI-MS)

Figure 3 shows schematic of a typical LDPI-MS instrument. During LDPI-MS analysis, sample is irradiated by a primary 349 nm (or other wavelength) pulsed desorption laser. The

laser energy imparted to the sample aids desorption of analyte compounds from the surface as neutrals into the gas phase which are then ionized by single photon ionization (SPI), using a secondary ionization laser. The ionization laser can be a molecular fluorine laser which emits at 157.6 nm (7.87 eV) or a 118 nm (10.5 eV) radiation obtained from the ninth harmonic of the Nd:YAG laser.[22] Alternately, radiation of different photon energies from VUV synchrotron light source can be employed for SPI.[23-25] The ions are then separated by a reflectron time of flight mass analyzer and detected.

Recently ablation of a sample surface by femtosecond laser pulses was combined either with MALDI-MS or LDPI-MS as a tool for depth profiling studies. This method may allow depth related chemical/molecular information to be obtained from a variety of biological materials with high depth resolution.[26]

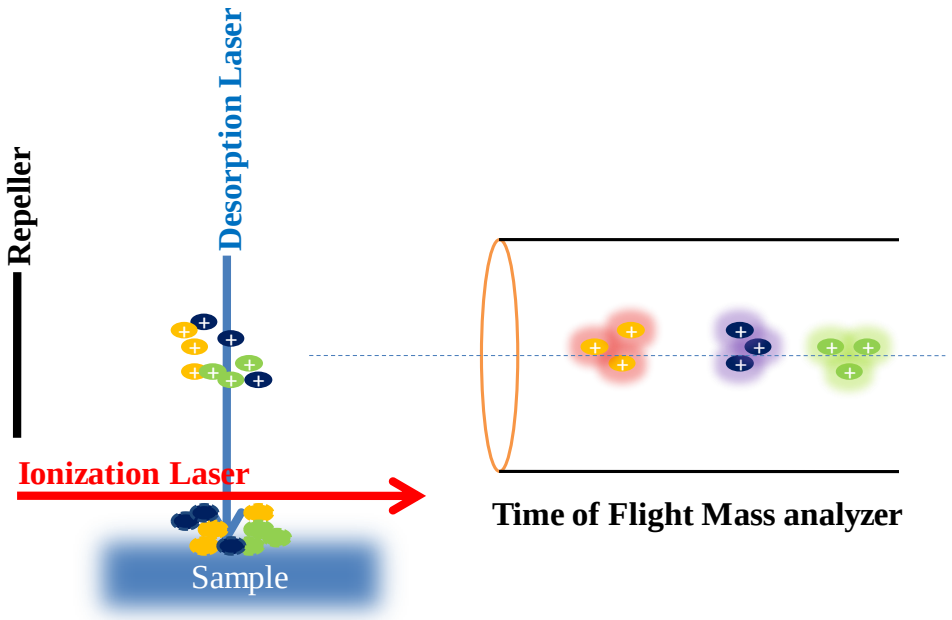

Figure 3. Schematic of a typical LDPI-MS instrument.

4. Comparison of MS Imaging Techniques

One of the major limitations in all the aforementioned techniques is the analysis time: depending on the sample size and desired spatial resolution, MS imaging can take several hours. This is because in MS imaging, microprobe based MS data are acquired spot to spot with slow and controlled rastering of sampling spot. In the case of SIMS and MALDI-MS imaging, the sample should be a conducting surface, as nonconducting samples can result in charge accumulation during analysis which adversely perturbs the energy of analyte ions.[8, 14] Also the MS imaging methods described here requires high vacuum conditions for analyses to be performed. This poses a major problem in sample preparation step particularly in sub-cellular molecular analysis, where loss or redistribution of analyte can occur and are difficult to prevent after sectioning and during sample preparation. Thus, a careful sample preparation is a prerequisite for MS imaging so that the cell fixation preserves the ion distributions within the sample without altering its composition spatially.[27] MS imaging techniques are also destructive: samples cannot be reused after analysis.

SIMS imaging has a greater potential to record molecular images of low mass analytes at spatial resolutions in sub micron scale and depth resolution in nanometer scale. However SIMS is known to suffer greater molecular fragmentation.[8, 14, 15, 28] MALDI-MS imaging has a greater potential to record molecular images of high mass analytes like proteins, polysaccharides and nucleic acids with a typical spatial resolution ~25 μm. [5, 27, 29-34] LDPI-MS imaging has a greater potential to record molecular images of low mass analytes like antibiotics, metabolites, amino acids and peptides with a spatial resolution of ~20 μm.[25, 35, 36] These different capabilities of the techniques mentioned above are due in large part to differences in their ionization mechanisms.

In the case of SIMS imaging, a major limitation is the extensive fragmentation[8] and bond breaking observed at the collision site. Typical kinetic energy of the primary ion beam in SIMS is often in the 1 – 100 keV range, making collision between the primary ion beam and the analyte highly energetic in comparison to the bond energies. However the amount of energy transferred to the analyte decreases as the lateral distance from the collision site increases. This produces fewer and fewer molecular fragmentations, resulting in the ejection of some intact molecular analytes from the first layers near the surface, provided they have enough energy to overcome the surface binding energy.[28] The ionization probability in SIMS strongly depends on the chemical environment within the sample, complicating the quantification of analytes in SIMS imaging. Surface morphology of the sample has a significant effect on SIMS data, so sample surfaces should be as flat as possible for SIMS imaging. Cleanliness of the sample is also a very important factor to be considered in SIMS imaging as any impurities adsorbed on the surface during the sample preparation can have an adverse effect on the accuracy of analysis.

The major limitation in MALDI-MS imaging is spot to spot variability observed within a single analysis, arising from differences in desorption/ionization efficiency rather than analyte concentration. This adverse effect can arise due to ion suppression, heterogeneous matrix application, detector noise, and/or sample charging and their net effect is to hinder quantification of analytes. These factors have slowed down the progress of MALDI-MS imaging for absolute quantification of analytes.[2, 7, 37] Another important challenge with MALDI-MS imaging is the sensitivity of the technique. For example considerable signal suppression can be observed for analytes desorbed from bacterial biofilms, tissues or any other surfaces when compared to that desorbed directly from MALDI plate.[38] Another major disadvantage of the technique is the relatively low spatial resolution compared to SIMS. Spatial resolution of MALDI-MS imaging

depends on several factors including the laser focus, the movement of the sample stage and the matrix crystal size. This has limited the spatial resolution to ~25 μm,[1] though some reports argue higher resolution is possible.[39]

In the case of LDPI-MS imaging, only analytes whose ionization energies are below the energy of ionization laser are detected. This has limited its application to study of analytes of lower ionization energy particularly when LDPI-MS is performed with the conventional fluorine laser (7.87 eV), which is not an issue with the 10.5 eV ionization source. However tagging of such analytes with a chromophore to reduce its ionization energy aids detection by 7.87 eV LDPI-MS.[35, 40] This selective ionization has a profound beneficial effect in the analysis of complex heterogeneous samples: it not only simplifies the MS spectra, but also minimizes background and improves sensitivity to detect analytes in picomole concentrations. However a major challenge is the spatial resolution which is dictated by the desorption laser spot size and instrument vibrations. This has limited the resolution to ~20 μm with the current instrument design.[35]

B. Bacterial Biofilms

MS imaging has recently been attracting the attention of the bacterial biofilm research community, because of its ability to obtain molecular information at a lower micron lateral resolution.[25,35,36] Bacterial biofilms are structures of microbial flora associated with surfaces in most natural environments. They are often enclosed and supported by an extracellular polysaccharide matrix which provides a stable and favorable microenvironment, protecting them from being swept away by liquid flow and from foreign invasions.[42]

Formation of bacterial biofilms involves several steps. First the bacterium approaches close to a surface and its mobility is almost completely restrained. This allows the bacterium to

find a surface for a transient association to eventually settle down to build its home. Initial interactions are supported by organelles such as type IV pili and flagella. After having chosen the neighborhood and the surface to live-in, the building up of a three dimensional biofilm starts with the secretion of exopolysaccharide to stabilize the pillars of the biofilm, eventually forming a mature biofilm. Occasionally, the biofilm-associated cells detach from the surface to initiate biofilm formation at a different location.[42]

Antimicrobial resistance and protection against host defenses are conferred to the bacterial community by biofilm formation.[42] This is because molecular pathways that regulate this biofilm formation among different species and even different strains vary greatly. Even the microenvironment within a single species biofilm is not homogenous: they vary not only in their composition but also possess microbial cells in completely different metabolic states.[43] This metabolic heterogeneity helps protect the members of the biofilm community and is also an important factor in their resistance to various antibiotics.[44]

Biofilms are responsible for a large number of medical infections and play a role in environmental and industrial processes.[43] Structure and composition of these microbial biofilm communities also depend on the properties of their anchoring surface, since the metabolism of individual microbes is affected by their environment.[45] Given that even a single species biofilm is composed of microbial cells in different metabolic states, it is critical to obtain molecular information from intact biofilms for their better understanding.[46] MS imaging of intact biofilms can provide chemical/molecular information that are not available from studies of homogenized microbial extracts, the traditional MS-based method for microbial studies.[1]

C. Research Objective

The primary research objective of this thesis was to develop and evaluate MS imaging protocols to study small molecules and proteins in bacterial biofilms at the molecular level.

Chapter 2 describes all MS imaging instruments used for the study, with a detailed explanation of their configuration and mechanics. The various sample preparation procedures used throughout the study are also explained, in addition to various general biofilm growth protocols used for study.

Chapter 3 describes the use of polyelectrolyte multilayers composed of high molecular weight polysaccharides, chitosan and alginate as a model biofilm to develop depth profiling protocols. A small molecular analyte 3,5-dibromotyrosine (Br_2Y) covalently bonded to alginate incorporated at defined depths in the multilayer system was used as a molecular probe, to evaluate the feasibility of depth profiling by C_{60}^+ ion sputtering in conjunction with X ray photoelectron spectroscopy (XPS).

Chapter 4 describes the use of the aforementioned multilayer model to develop LDPI-MS and SIMS imaging protocols. Br_2Y electrostatically adsorbed on the multilayer was probed by SIMS and by LDPI-MS at different SPI photon energies, to evaluate the effect of different photon energies for LDPI-MS analysis of Br_2Y and a comparison of LDPI-MS and SIMS are also made.

Chapter 5 describes the use of MALDI-MS imaging to identify proteins and peptide in intact *Enterococcus faecalis* bacterial biofilms and to obtain their spatial localization. MALDI-MS and tandem MS was combined with database searches to identify proteins and peptides from intact biofilms. The identified proteins and peptides were then imaged to demonstrate the feasibility of MALDI-MS imaging of proteins and peptides in bacterial biofilms.

Chapter 6 describes the use LDPI-MS imaging as a robust tool for small molecule quantification from intact polyelectrolyte multilayer surface. The multilayer surface was used here as an antimicrobial surface to anchor a small molecule antibiotic. The slow and efficient release of the small molecule antibiotic into bacterial biofilms was evaluated for its long term efficacy and LDPI-MS imaging was used to quantify the small molecule antibiotic and to evaluate the extent of its release from the multilayer surface.

Chapter 7 gives the concluding remarks and future directions for the MS imaging field. It describes the significance of the MS imaging technique in perspective of the protocols described in this thesis, the chapter also tries to address, at least partially some of the current limitations encountered with the MS imaging technique and some future prospects for this fast growing MS imaging technique.

II. EXPERIMENTAL METHODS

A. Instrumentation

1. LDPI-MS and SIMS

Two different LDPI-MS Instruments were used for MS analysis, 7.87 eV laser LDPI-MS located at the University of Illinois at Chicago and 8 – 12.5 eV synchrotron LDPI-MS located at the Chemical Dynamics Beamline at the Advanced Light Source (Lawrence Berkeley National Laboratory, Berkeley, CA).

a. 7.87 eV Laser LDPI-MS

7.87 eV laser LDPI-MS were collected using a custom built instrument at the University of Illinois at Chicago which is equipped with a 157.6 nm pulsed laser (7.87 eV) for photoionization and was described in detail elsewhere.[35] Briefly this LDPI-MS has a 349 nm Nd:YLF desorption laser operating at 100 Hz, with a spot size of ~20 μm diameter and typical desorption laser peak power density ranging from 30 to 70 MW/cm^2. For imaging MS applications, the sample was rastered at 100 – 625 μm/s with respect to the laser, so each 20 μm sample spot was sampled by ~ (3 – 20) desorption laser shots and a total of 50 – 100 laser shots were sufficient to obtain spectra with optimal signal to noise. The desorbed neutral molecules were photoionized using a 7.87 eV molecular fluorine excimer laser operating at a 100 Hz with a spot size of approximately 8 mm in the ionization region and energy of ~100 μJ/pulse. The photoionized neutrals were extracted using a pseudo-orthogonal delayed pulsed extraction and detected by a home-built two-stage reflectron time of flight mass spectrometer. Spectra were recorded at a delay of 3.9 μs between the photoionization laser and the extraction pulse. Varying this delay by a few μs affected the absolute signal, but not the overall appearance of the spectra. The instrument was also equipped with an ultrahigh vacuum compatible translation stage for sample

manipulation and a digital single lens reflex camera for real time sample viewing on a high definition television. Data acquisition and sample stage movements were computer controlled using customized software. The MS imaging data were rendered to BioMap compatible using customized software for image processing and analysis.

Calibration of the 7.87 eV LDPI-MS was performed using a standard calibration mixture consisting of sexithiophene (6T), 2,3-dihydroxybenzoic acid (DHB) and sodium at *m/z* 23.0, 154.0, 329.0, 411.0, 494.0 and 657.9. The experimental mass resolution at *m/z* 336.9 was 420, calculated using m/Δm where Δm is the full-width half-height maximum or FWHM.

b. <u>8.0 – 12.5 eV Synchrotron LDPI-MS and SIMS</u>

8.0 – 12.5 eV synchrotron LDPI-MS and SIMS were recorded using a commercial SIMS instrument (TOF.SIMS 5, ION-TOF Inc., Munster, Germany) using 25 keV Bi^{3+} primary ions.[24] The SIMS instrument was modified for LDPI-MS by the addition of a 349 nm pulsed desorption laser (Explorer, Newport) operating at 2500 Hz with a spot size of ~30 μm diameter and typical laser desorption peak power density of 1 to 10 MW/cm^2. The laser desorbed neutral molecules were photoionized by 8.0 to 12.5 eV tunable VUV synchrotron radiation from the Chemical Dynamics Beamline at the Advanced Light Source (Lawrence Berkeley National Laboratory, Berkeley, CA).[47] 143,000 laser shots on a single spot were used for recording each mass spectrum. This instrument was also used to record photoionization efficiency curves of gas phase analyte molecules by thermally heating the sample above 120°C while scanning the VUV photon energy, without any ion or laser desorption. The experimental mass resolution at *m/z* 336.90 was 980 and 1100 for LDPI-MS and negative ion SIMS, respectively.

2. MALDI-MS

MALDI-MS imaging was performed using a commercial MALDI-MS instrument (4700 TOF/TOF, AB SCIEX, Foster City, CA, USA) under MS and MS/MS mode. The MALDI-MS instrument is equipped with a 355 nm Nd: YAG laser operating at 200 Hz with a laser spot size of ~150 μm and laser power set to 2800 arbitrary units, where the maximum of 7000 arbitrary units corresponded to a laser power of ~14 μJ. Helium was used as a collision gas for MS/MS experiments. Data were acquired by commercial software (4000 Series Explorer V3, AB SCIEX). Calibration of the instrument was performed using the standard calibration mixture (mass standards kit for calibration, 4333604, AB SCIEX) at *m/z* 905.05, 1297.51, 1571.61, 2094.46, 2466.72, and 3660.19. MS image acquisition was performed using open source software (4700 Imaging V3, http://maldi-msi.org) with a raster size of 150 μm and 255 laser shots per spot. The MS images acquired were processed further using open source software (BioMap V3803, http://maldi-msi.org).

3. C_{60}^+ Sputter Source and X-ray Photoelectron Spectrometer (XPS)

C_{60}^+ sputter source consists of a home-built differentially pumped ion beam source with a commercial Wien mass filter (Colutron Research Corporation, Boulder, CO) attached to a preparative vacuum chamber kept at a base pressure of ~1×10^{9} torr for C_{60}^+ sputtering.[48, 49]

The home-built ion beam source consisting of a cylindrical reservoir in which C_{60} was loaded in its solid state and heated to produce vapors of C_{60}. The vapors of C_{60} were ionized by 80 eV electron impact to produce C_{60}^+ and C_{60}^{2+} ions. C_{60} ions formed were accelerated to 8 keV, mass separated by a Wien filter and bent at 3° angle to remove any fast neutrals before being guided by a series of lenses to bombardment the sample target at a normal angle of incident in

the preparative chamber. The C_{60}^{+} ion current produced from the source was measured using a Faraday cup with typical ion currents observed in 40 – 900 pA range over 4 mm^2 spot.[49]

The preparative chamber was connected to analytical chamber under vacuum for effective sample transfer from the preparative chamber to the XPS (analytical) chamber without exposure to atmosphere. The instrument was also equipped with a magnetic arm for sample manipulation and transfer, from and to the preparative, analytical chamber.

The XPS instrument consists of a high resolution monochromatic Al-Kα X-ray source (15 keV, 25 mA emission current, VSW MX10 with 700 mm Rowland circle monochromator) and a 150 mm hemispherical concentric analyzer with a multichannel detector (VSW Class 150), operating under constant energy analyzer mode. The photoemission angle was normal to the surface with the pass energy normally set to 22 eV for core level spectral scans and 44 eV for survey scans. The XPS instrument was calibrated to give an electron energy resolutions of 0.75 and 1.16 eV (FWHM) for Ag ($3d_{5/2}$) peak on a clean polycrystalline Ag foil at pass energy of 22 and 44 eV respectively and all XPS spectra were referenced to the aliphatic/aromatic C(*1s*) core level photoemission peak of untreated polystyrene at 285.0 eV. The XPS instrument control and acquisition were performed using the commercial software (COLLECT-W, version 8.4-A-A) and data processed and analyzed using a commercial software (SPECTRA Presenter, version 8.0-C-1).[50, 51]

B. Bacterial Growth and Treatment

A general description of the various bacterial growth conditions used in this thesis are described briefly here. Detailed descriptions of a specific bacterial growth conditions and treatments are described in each chapter, depending on the type of study.

1. Planktonic Liquid Culture Growth

All planktonic liquid cultures described in this thesis were grown either in tryptic soy broth growth media (Difco, Detroit, MI, USA) containing 10% (w/v) glucose (TSBG) or without any glucose (TSB). A 5 mL TSB or TSBG growth media was inoculated with 1 mL of bacterial solution in a sterile 15 mL test tube and incubated at 37 °C for 12 to 18 hours.

2. Membrane Colony Biofilm Growth

Figure 4 shows an optical image of a typical *Enterococcus faecalis* membrane colony biofilm grown in tryptic soy agar (TSA) growth media. All membrane colony biofilms described in this thesis were grown in TSA growth media (Difco, Detroit, MI, USA) on sterile polycarbonate membrane (Millipore, 0.20 µm pore size, 25 mm diameter, Fisher Scientific). Petri dishes were prepared with 25 mL of TSA growth media each with either two or four sterilized polycarbonate membranes, sterilized by exposing the membranes to radiation from a germicidal ultraviolet lamp (254 nm, 4.8 watts, held ~30 cm from the sample, G15T8, Osram Sylvania, Danvers, MA). Each membrane was inoculated with 40 µL of planktonic bacterial liquid culture growth, and incubated at 37 °C for several days depending on the type of study, with the TSA growth media replenished every day.

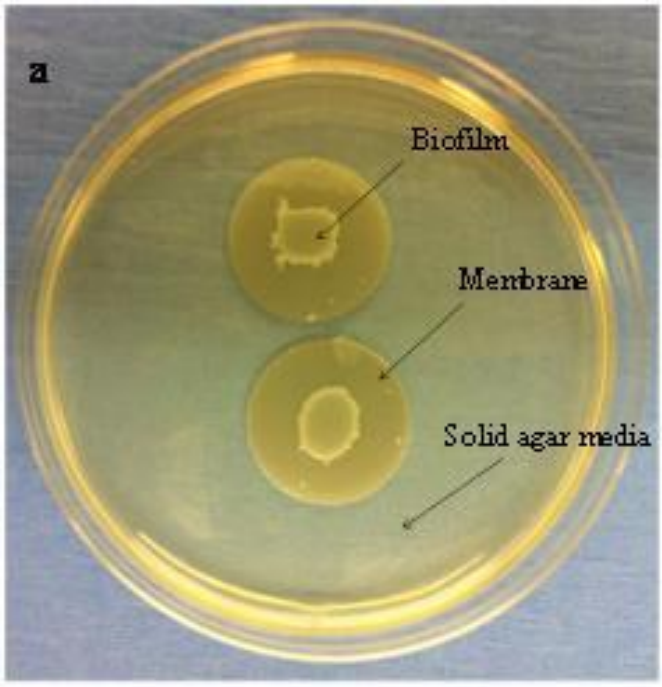

Figure 4. Optical image of *Enterococcus faecalis* membrane colony biofilms grown in tryptic soy agar growth media (TSA).

3. Biofilm Growth on Solid Substrate

Biofilms on stainless steel MALDI plates were grown either under static growth conditions or under drip flow conditions, depending on the type of study.

For static biofilm growth, a sterile stainless steel MALDI plate was placed in a Petri dish and inoculated with 1 mL of planktonic bacterial liquid culture growth and incubated for 8 to 12 hours for the initial adhesion of the bacterial cells onto the MALDI plates. After the initial adhesion, biofilms were statically grown in 10 mL TSBG growth medial at 37 °C for 7 to 10 days, depending on the type of study, while replenishing growth medium daily.

Figure 5 shows optical image of a typical *E. faecalis* biofilms grown on stainless steel MALDI plate by drip flow reactor. For drip flow biofilm growth, sterile stainless steel MALDI plates were mounted in the flow cell lanes of a sterile drip flow reactor and were inoculated with

1 mL of planktonic bacterial liquid culture, to allow initial adhesion of the cells to the MALDI plates. The reactor set-up was incubated for 24 h at 37°C with 20 mL of TSBG growth media added to each of the flow cell lanes. After 24 h of static growth, TSBG growth medium was delivered at a flow rate of ~3.6 mL/h for three or five days depending on the type of study using a peristaltic pump to each of the flow cells.

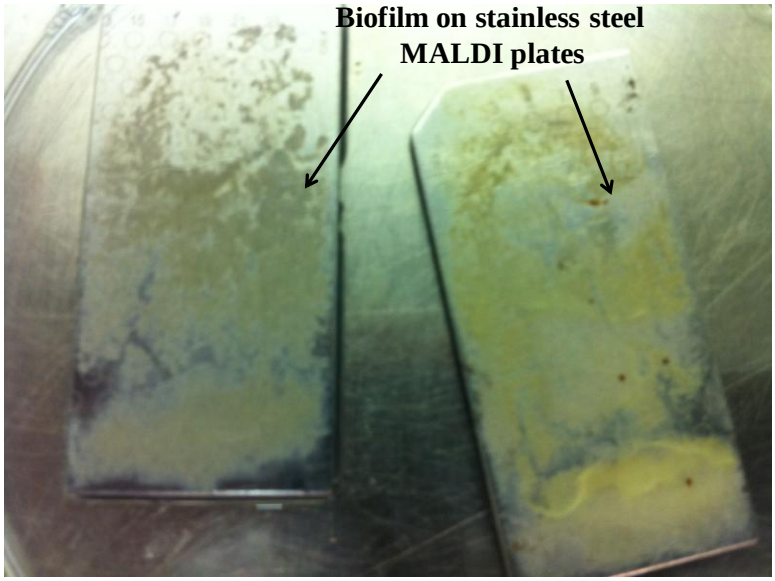

Figure 5. Optical image of *E. faecalis* biofilms grown on a stainless steel MALDI plate by drip flow reactor.

C. Polyelectrolyte Multilayer Preparation

Figure 6 shows a schematic of polyelectrolyte multilayer preparation. Polyelectrolyte multilayers were prepared on gold coated silicon substrate (Sigma-Aldrich) using two biocompatible high molecular weight polysaccharides, chitosan and alginate.[52, 53] Briefly, the substrate was cleaned by sonication in piranha solution (7:3 v/v concentrated sulfuric acid:30% hydrogen peroxide) and rinsed several times with distilled water. A cysteamine solution was used to prepare a self-assembled monolayer on the gold surface which was then reacted with a

glutaraldehyde solution, which covalently bound the first polysaccharide, chitosan. The modified substrate was then manually immersed alternately in chitosan solution (0.2% dissolved in 2% acetic acid solution) and alginate solution (2% in water) for one hour each, with intermediate aqueous rinsing. The multilayer so formed consisted of a total of 20 alternating layers of chitosan and alginate (Figure 7). Formation of the multilayer was verified by attenuated total reflectance infrared spectroscopy and X-ray photoelectron spectroscopy. A small molecule analyte was incorporated in this multilayer by covalently binding it to alginate and replacing neat alginate with the analyte bound alginate during the multilayer preparation. Alternately, a small molecule analyte was also electrostatically adsorbed on this multilayer surface.

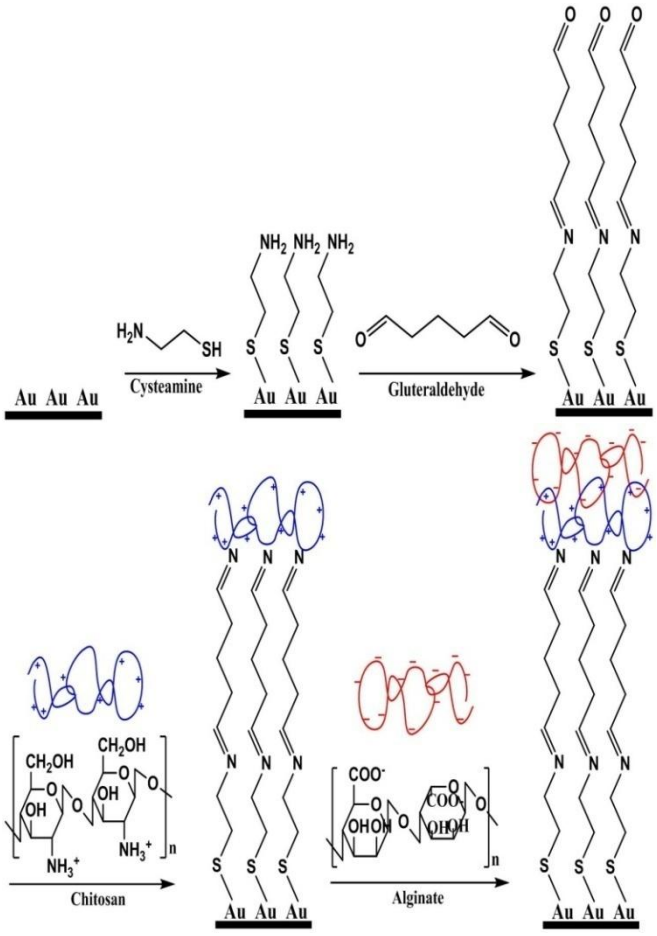

Figure 6. Schematic of polyelectrolyte multilayer preparation.

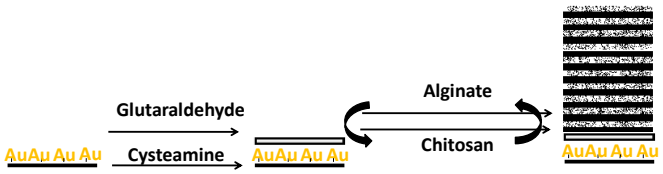

Figure 7. Preparation of polyelectrolyte multilayer consisting of a total of ten layers each of chitosan and alginate.

D. Sample Preparation for MS Analysis

The sample preparation was modified depending on the type of analysis and the type of instrument used for analysis. In this chapter, general sample preparation for MS analysis is described. Detailed sample preparation protocols for different individual studies are described in each chapter.

1. Neat Analyte Sample Preparation for MS Analysis

Neat analyte sample for SIMS and LDPI-MS was generally prepared by dissolving the analyte in a suitable solvent and spotting on conducting substrates, usually a stainless steel MALDI plate or gold coated silicon chip. Solvent was evaporated at either room temperature or at 40 – 50 °C on a hot plate prior to analysis.

For MALDI-MS analysis neat samples were prepared either as described above, except that after drying at room temperature either α-cyano-4-hydroxycinnamic acid (CHCA, Sigma Aldrich) matrix at 20 g/L concentration in 7:3 (v/v) acetonitrile:TFA (0.1% v/v in water) or sinapinic acid matrix at 20 g/L concentration in 1:1 (v/v) acetonitrile:trifluoroacetic acid (TFA, 0.1% (v/v) in water) was added and evaporated to dryness at room temperature prior to analysis. Alternately the neat analyte was directly dissolved in a suitable MALDI matrix solution and spotted on MALDI stainless steel plates and evaporated to dryness at room temperature prior to analysis.

2. Planktonic Cell Preparation for MS analysis

Bacterial liquid cell cultures were harvested by centrifugation at 7,558 g for 5 min and the supernatant discarded. The cells were washed twice with 1 mL of sterile de-ionized water, and the washing discarded. For LDPI-MS analysis the cell pellet was resuspended in 50 to 100 µL of de-ionized water and spotted on stainless steel MALDI plates and dried at room temperature prior to analysis. For MALDI-MS analysis the cell pellet was resuspended with CHCA matrix at 20 g/L concentration in 7:3 (v/v) acetonitrile:TFA (0.1% v/v in water) or with sinapinic acid matrix at 20 g/L concentration in 1:1 (v/v) acetonitrile:trifluoroacetic acid (TFA, 0.1% (v/v) in water). This whole-cell in matrix mixture was spotted on the MALDI plate, and evaporated to dryness at room temperature prior to analysis.

3. Membrane Colony Biofilm Preparation for MS Analysis

Membrane colony biofilms were removed from the agar plate and the biofilms were blotted on stainless steel MALDI plate, with care taken to maintain the spatial integrity of the biofilm cells during the transfer. The biofilm was then left in the load lock of LDPI-MS instrument for a minimum of 1 hour prior to analysis by LDPI-MS. For MALDI-MS analysis CHCA matrix at 20 g/L concentration in 7:3 (v/v) acetonitrile:TFA (0.1% v/v in water) was sprayed on the sample using an airbrush (Testors Corp., Rockford, IL, USA) at 20 psi spray pressure and dried at room temperature prior to analysis.

4. Plate Biofilm Preparation for MS Analysis

Plate biofilms after their growth cycle were washed with 5 mL de-ionized water for a minimum of three times to remove loosely attached biofilm cells and any excess nutrient growth media and were dried at room temperature prior to LDPI-MS analysis. For MALDI-MS analysis, a freshly prepared CHCA matrix at 20 g/L concentration in 7:3 (v/v) acetonitrile:TFA (0.1% v/v

in water) or sinapinic acid matrix at 20 g/L concentration in 1:1 (v/v) acetonitrile:trifluoroacetic acid (TFA, 0.1% (v/v) in water) was sprayed using an airbrush (Testors Corp., Rockford, IL, USA) at 20 psi spray pressure followed by drying for ~ 5 min between each spray cycle and finally dried in a desiccator overnight prior to analysis.

III. MULTILAYER FILM WITH BOUND BROMINATED TYROSINE FOR DEPTH PROFILING BY C_{60}^+ SPUTTERING AND X-RAY PHOTOELECTRON SPECTROSCOPY

A. Introduction

Biofilms consist of microcolonies of microbial cells typically embedded in an extracellular polysaccharide matrix adherent to solid surfaces.[42, 54-56] Biofilms are responsible for a large number of infections in humans, hence there is a need to study them.[56-60] The structure and composition of these microbial biofilm communities depend greatly on the property of surface to which they adhere.[42] The microbial cells shape their metabolism based on the environment in which they are present; hence even a single species biofilm has microbial cells with different metabolic states. Due to this chemical and structural complexity it is difficult to evaluate protocols on actual biofilms. Hence it would be appropriate to evaluate protocols on model systems. Polyelectrolyte multilayers were used here as a model biofilm to evaluate depth profiling strategies.

SIMS is one method that is well developed for MS imaging. Analysis and depth profiling studies of various model multilayer structures of biologically relevant molecules by SIMS have advanced the field to three-dimensional imaging of biological materials ranging from biological cells to brain tissues.[61] Winograd, Wucher and others have developed various models that incorporate organic multilayers and/or polysaccharides to evaluate SIMS protocols. C_{60}^+ ion sputtering and SIMS analysis of organic multilayered Langmuir-Blodgett films of barium arachidate,[62] dipalmitoyl-phosphatidylcholine-sucrose multilayered structures thereof[63] and peptide doped trehalose thin films on silicon substrate[15] have all been used to demonstrate that C_{60}^+ ion sputtering leads to less chemical damage with enhanced secondary ion

yields and better depth resolution in these organic materials. Analysis of various polymeric materials ranging from aliphatic, aromatic, fluorine containing and natural polymers including polysaccharides by XPS after C_{60}^+ ion sputtering demonstrated that C_{60}^+ ion sputtering causes very little to no chemical damage to most of these polymers[64]. These results show that C_{60}^+ sputtering in combination with SIMS and/or XPS is a promising technique with tremendous potential for three dimensional molecular imaging of biological material.

Polyelectrolyte multilayers are structurally well-defined model system for biofilms, prepared by electrostatically binding layer by layer, two naturally occurring, oppositely charged polysaccharides alginate and chitosan. The high molecular weight biopolymers alginate and chitosan in multilayers simulates the extracellular polysaccharides of biofilms, in addition to this small molecular analytes or antimicrobials can be incorporated at a well defined depth in this multilayer model. These features make multilayers excellent model to evaluate MS imaging protocols for biofilms.

This study demonstrates the use of C_{60}^+ sputtering in conjunction with XPS as a technique to do depth profiling in multilayers, with 3,5-dibromotyrosine (Br_2Y) as a probe molecule incorporated at well defined depths in the multilayer Br_2Y is covalently bound to alginate and incorporated at known depths in the multilayer. In addition to this XPS analysis was also used to demonstrate that C_{60}^+ sputtering of the multilayer surface does not impart any significant chemical damage.

B. Experimental Details

Polyelectrolyte multilayer were prepared as described in Chapter 2, with a total of 20 alternating layers of chitosan and alginate deposited as shown in Figures 6 and 7. Small molecular analyte Br_2Y was incorporated at well defined depths at fifth, tenth and fifteenth layer

from the air-multilayer interface, by replacing neat alginate with Br_2Y covalently bound to alginate.

Figure 8 shows the chemical reaction involved in binding Br_2Y to alginate. Br_2Y was covalently bound to alginate utilizing aqueous carbodiiimide chemistry as described in detail elsewhere.[65-68] Briefly, the reaction involved was a nucleophilic acyl substitution reaction, to form amide linkages between the N-terminus of the binding Br_2Y and the carboxylate moieties on the mannuronic acid and guluronic acid residues of the alginate backbone.

Alginate was suspended in 100 mM MES (2-N-morpholino ethane sulfonic acid) buffer with 300 mM NaCl at pH 6.5 to make a 1% solution of alginate. EDAC (1-ethyl-dimethylaminopropyl carbodiimide) and sulfo-NHS (N-hydroxy-sulfosuccinimide) were added to the alginate solution with stirring. After 10 min of stirring Br_2Y solution was added (100 mg of Br_2Y dissolved in 1 mL of acetonitrile and 7 mL of MES) and continued stirring for 18 hours at room temperature. The solution was then transferred to a dialysis cassette (Slide-A-Lyzer Dialysis Cassette, 3500 MWCO Thermo Scientific) and kept in a 1 L solution of deionized water containing 300 mM NaCl dialysis solution. The dialysis solution was changed every 8 hours for a total of three days. The final content in the dialysis cell was transferred to a 50 mL centrifuge tube, freeze dried and characterized by ^{13}C- nuclear magnetic resonance spectroscopy (NMR) and XPS.

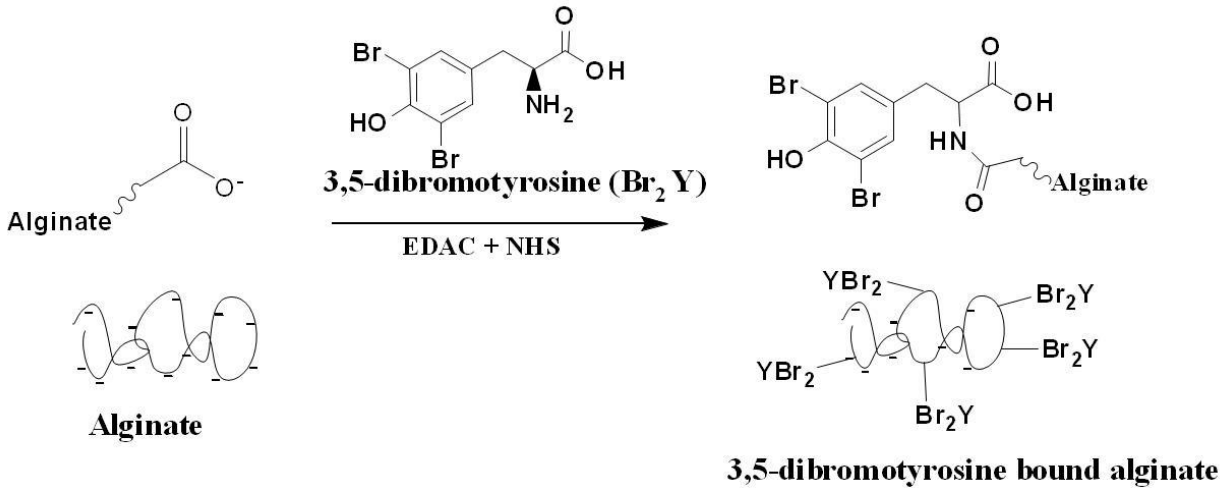

Figure 8. Chemical reaction binding 3,5-dibromotyrosine (Br_2Y) to alginate.

C_{60}^+ sputtering was performed on these polyelectrolyte multilayer samples. The amount of material removed from this polyelectrolyte multilayer during the C_{60}^+ sputtering was determined using a quartz crystal microbalance (QCM). For which the multilayer was prepared on a gold coated QCM chip instead of gold coated silicon substrate and the QCM measurements were made during C_{60}^+ sputtering. The manipulator in the preparative chamber was modified to accommodate a 6 MHz quartz crystal probe (934-000, 14 mm, gold coated, Sigma Instruments with SQC 222 controller), which was fixed to the opposite side relative to the sample holder. This allowed the same sputtering conditions for sample and QCM analysis by a simple manipulator rotation.

XPS analysis was performed before and after C_{60}^+ sputtering to gauge the extent of chemical damage caused on the polyelectrolyte multilayer due to C_{60}^+ sputtering and also to probe Br_2Y at different depths in the multilayer.

C. Results and Discussion

1. Characterization of Multilayer and Br_2Y Bound Alginate

The binding of Br_2Y to alginate was confirmed by ^{13}C-NMR spectroscopy and XPS, Br_2Y-alginate was dissolved in D_2O (~40 mg/ml) and ^{13}C-NMR was recorded (Bruker Avance 500-MHz) using a 180° pulse and typically 20000 to 40000 scans at a sample temperature of 50°C to decrease the viscocity and thereby, the line widths. Alginate is a linear polymer of glycuronan (1→4) –linked α-L-guluronate (G) and β-D-mannuronate (M) residues arranged in a non regular, blockwise pattern along the chain.[69] The spectral regions of the carbonyl groups and anomeric carbon atoms in alginate are well documented.[69-71] Figure 9 shows the ^{13}C-NMR of Br_2Y-alginate. The alginate peaks in the spectra are assigned according to the previous data for alginate.[69] C-1 carbons of (M) and (G) acids show peaks in the range 101 to 104 ppm, and each peak is separated based on the vicinal residue bonded with the carbon. Also peaks in the range 65.8 to 81.5 ppm associated with other carbon atoms in (M) and (G) residues, resonating for C-2 to C-5 were observed, The carbonyl carbon C-6 always appeared at 176.5 and 177.2 ppm in the case of neat alginate.[71] However binding of Br_2Y to alginate gave peak at 175.3 ppm corresponding to the amide C-6 carbon, confirming the binding of Br_2Y to alginate.

Binding of Br_2Y to alginate was also confirmed by XPS analysis. Figure 10 shows the XPS spectra of Br_2Y-alginate and neat alginate without Br_2Y on gold coated silicon substrate; the presence of Br ($3d^{5/2}$ and $3d^{1/2}$) peak at binding energy 69, 70 eV for Br_2Y-alginate, confirmed the binding of Br_2Y to alginate.

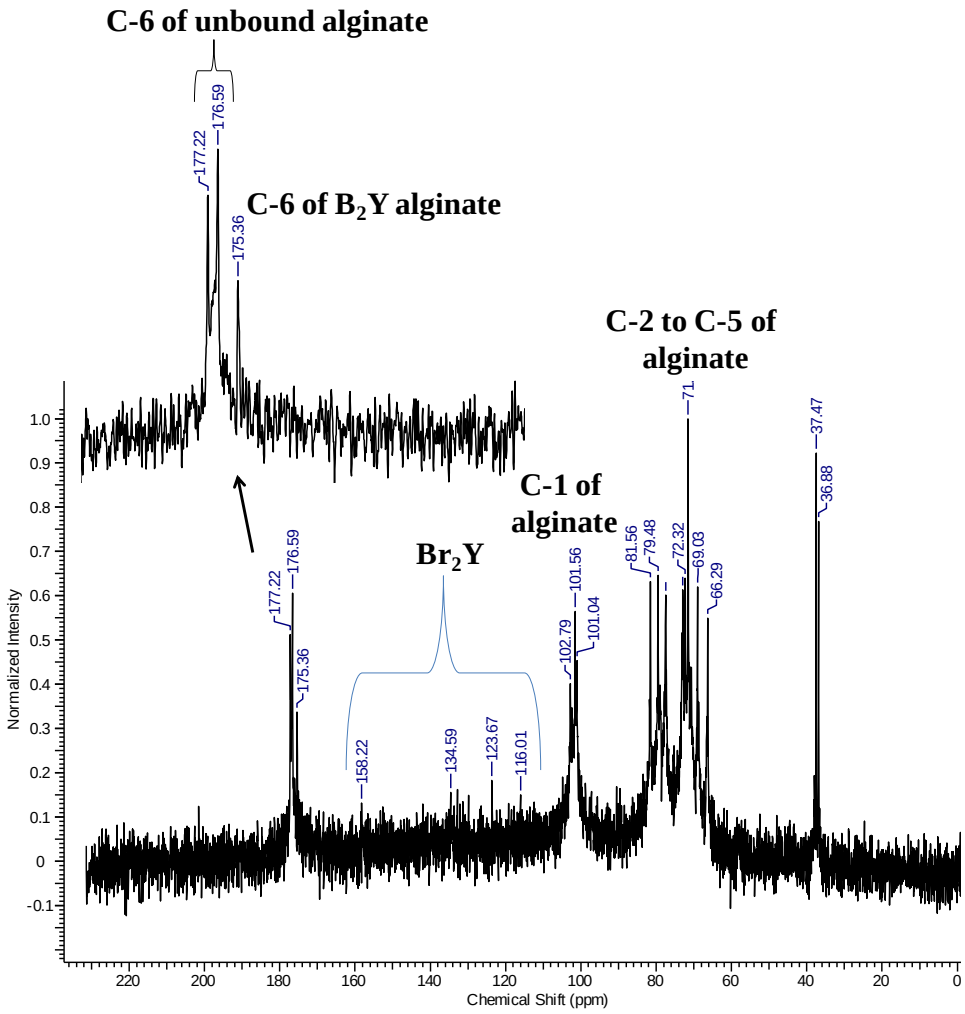

Figure 9. ^{13}C-NMR spectra of Br_2Y-alginate solution in D_2O at 50 °C confirms the binding of Br_2Y to alginate.

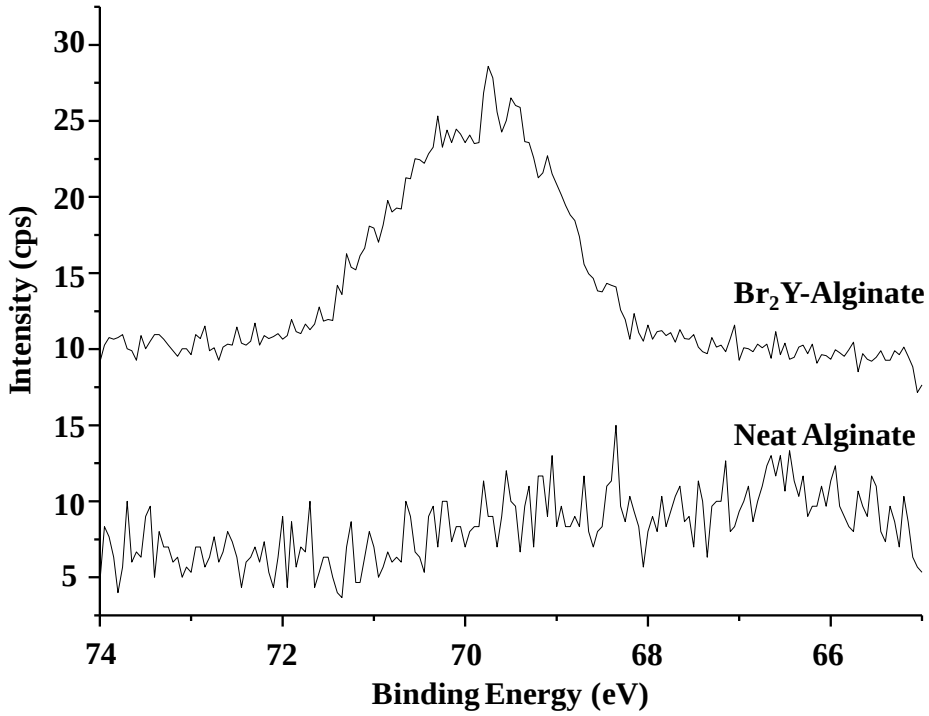

Figure 10. Br ($3d^{5/2}$ and $3d^{1/2}$) XPS core level spectra of neat alginate (bottom trace) and Br_2Y bound alginate (top trace).

Formation of chitosan-alginate polyelectrolyte multilayer was characterized by attenuated total reflectance Infrared spectroscopy (ATR-IR). Figure 11 shows the ATR-IR spectrum, bottom for control (neat gold) substrate and the top for a sample with monolayers of chitosan and alginate. Several vibrational frequencies previously assigned to chitosan and alginate was observed confirming the formation of alginate and chitosan monolayers.[72-75] The strong vibration at 1645 cm^{-1} assigned to amide I vibrations of chitosan, 1722 cm^{-1} assigned to C=O stretch of COOH of alginate, 1150 cm^{-1} antisymmetric stretch C-O-C and C-N stretch of chitosan and alginate and 3290 cm^{-1} O-H and N-H stretch of chitosan and alginate were observed.

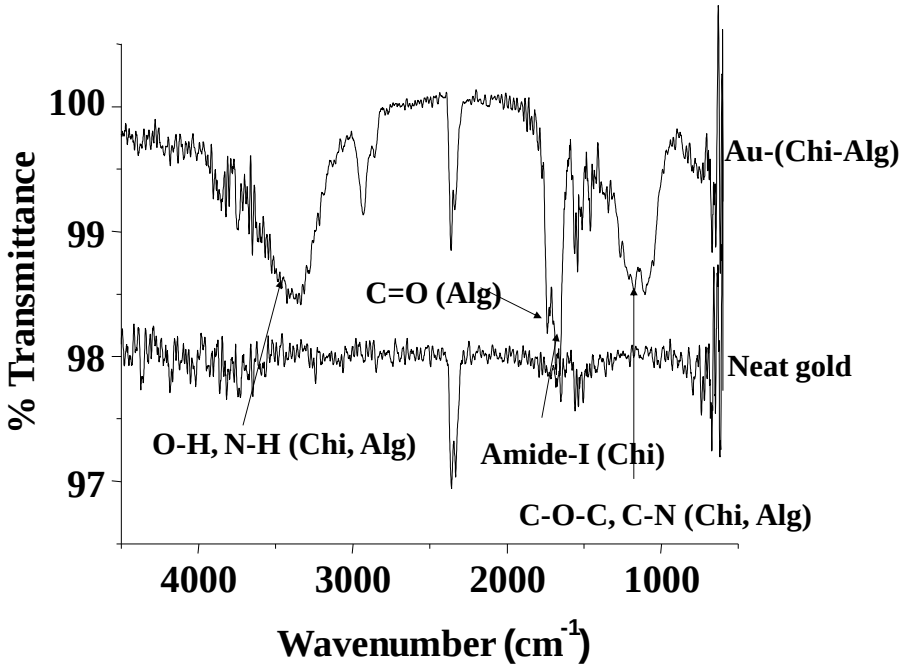

Figure 11. ATR-IR spectrum for neat gold substrate (bottom spectra) and multilayer with monolayer of chitosan and alginate (top spectra). (Alginate and chitosan are abbreviated as Alg and Chi respectively).

Figure 12 shows the ATR-IR spectra for the polyelectrolyte multilayer sample with a total of two, five and fifteen layers of chitosan and alginate. An increase in the number of layers leads to an increase in the intensity of the peaks corresponding to the group frequencies of chitosan and alginate (see above), confirming the formation of polyelectrolyte multilayer.

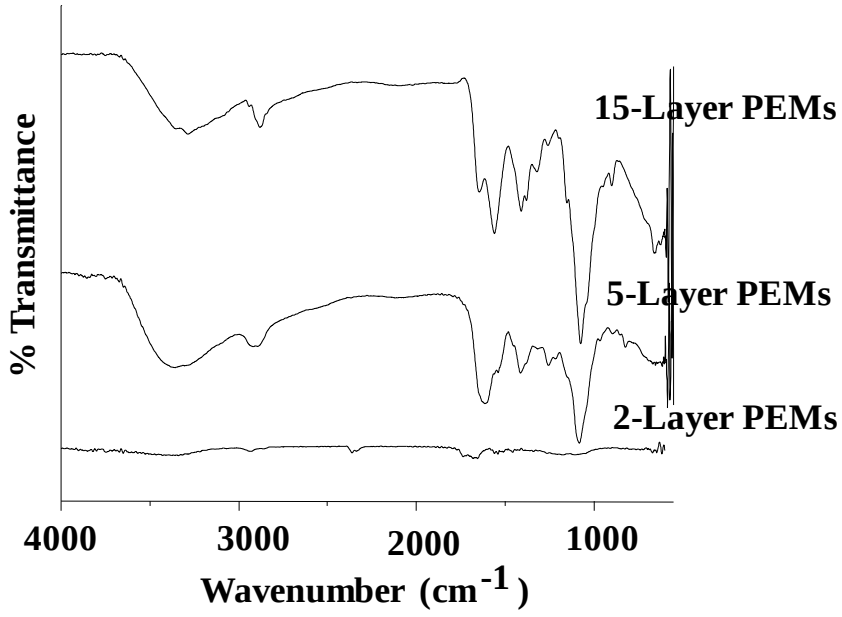

Figure 12. ATR-IR spectra of polyelectrolyte multilayer, with a total of 2, 5 and 15 layers of chitosan and alginate labeled as PEM (polyelectrolyte multilayers).

2. C_{60}^+ Sputter Yield by Quartz Crystal Microbalance Analysis (QCM)

C_{60}^+ sputtering was performed using a 8 kV C_{60}^+ defocused primary ion beam of ~ 4 mm^2 spot size, with an ion fluence of 3.4×10^{14} ions/cm^2. QCM measumerments of the polyelectrolyte multilayer with twenty alternating layers of chitosan and alginate was performed during C_{60}^+ sputtering to determine the C_{60}^+ sputter yield.[49] The average sputter yield observed for the polyelectrolyte multilayer using a defocused C_{60}^+ primary ion beam was 4.8×10^4 amu/C_{60}^+ ions (Table 1). This sputter rate observed for the polyelectrolyte multilayer was close to that observed for various other polymers.[49]

Sample #	Sputter Yield (amu/ions)	%RSD	Average Sputter yield (amu/ions)
1	6.2×10^4		
2	5.3×10^4	35.5	4.8×10^4
3	2.9×10^4		

Table I. C_{60}^+ sputter yield for the polyelectrolyte multilayer system.

3. C_{60}^+ Depth Profiling of Br_2Y

A polyelectrolyte multilayer sample without any added B_2Y was examined by XPS before and after C_{60}^+ sputtering to examine any chemical damage induced by C_{60}^+ sputtering. Figure 13 shows C *1s* core level spectra for the polyelectrolyte multilayer sample before and after C_{60}^+ sputtering. The peak region at 285.0 eV is attributed to (C-C) of adventitious carbon, hydrocarbon contaminants. For alginate and chitosan the ether and alcohol contributions C-O-C and C-O-H are found in between 286.6 and 286.9 eV, the acetal carbon (O-C-O) is found between 288.0 to 288.2 eV and the carboxyl carbon is observed between 287.4 to 289.3 eV.[76] There is no significant difference observed in the C *1s* spectra (Figure 13) before and after C_{60}^+ sputtering except for the regions attributed to the adventitious hydrocarbon at 285.0 eV, where a slight increase in the peak height was observed after sputtering. This can however, be attributed to the carbonization of the surface due to deposited C_{60} residues. Furthermore, the C-O region showed a slight decrease in the intensity due to oxidation of radical sites formed during sputtering.[77]

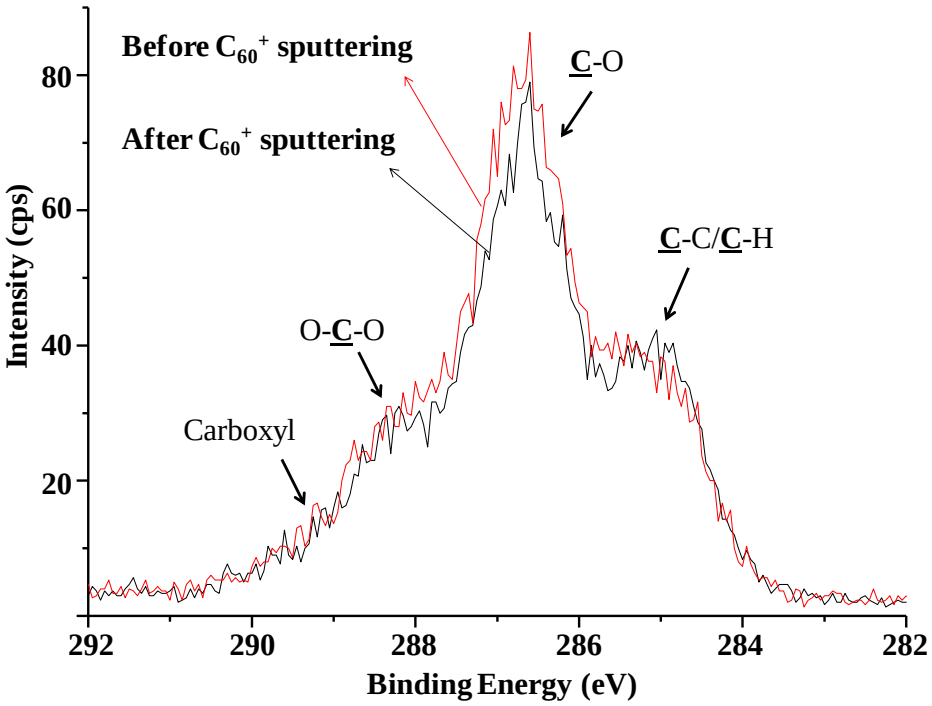

Figure 13. C *1s* core level spectra of polyelectrolyte multilayer before and after C_{60}^+ sputtering indicating no significant chemical damage.

Figure 14 shows O *1s* core level spectra for the polyelectrolyte multilayer sample before and after C_{60}^+ sputtering. For alginate and chitosan the peak region between 531.9 and 532.5 eV is attributed to (O-C=O), the ether and alcohol contributions C-O and C-O-H are found in between 532.4 and 533.1 eV, the acetal oxygen (O-C-O) are found between 532.9 to 533.5 eV and the carboxyl oxygen is observed between 533.2 to 533.9 eV.[76] There is no significant difference observed in the O 1s spectra (Figure 14) before and after C_{60}^+ sputtering. Except for the C-O bond region which showed a slight decrease in the intensity after C_{60}^+ sputtering, this can however be attributed to oxidation of radical sites formed during sputtering, which is also supported by a slight decrease in corresponding region in the C *1s* spectra after C_{60}^+ sputtering (Figure 13). Similar observations were reported during C_{60}^+ sputtering of cellulose.[77]

Thus, XPS analysis of the polyelectrolyte multilayer before and after C_{60}^{+} sputtering indicate that C_{60}^{+} sputtering removes the damaged layer and leaves material that does not display damage observable by XPS (i.e. C_{60}^{+} ion sputtering has larger sputter yield compared to damage yield) for the multilayer surface.

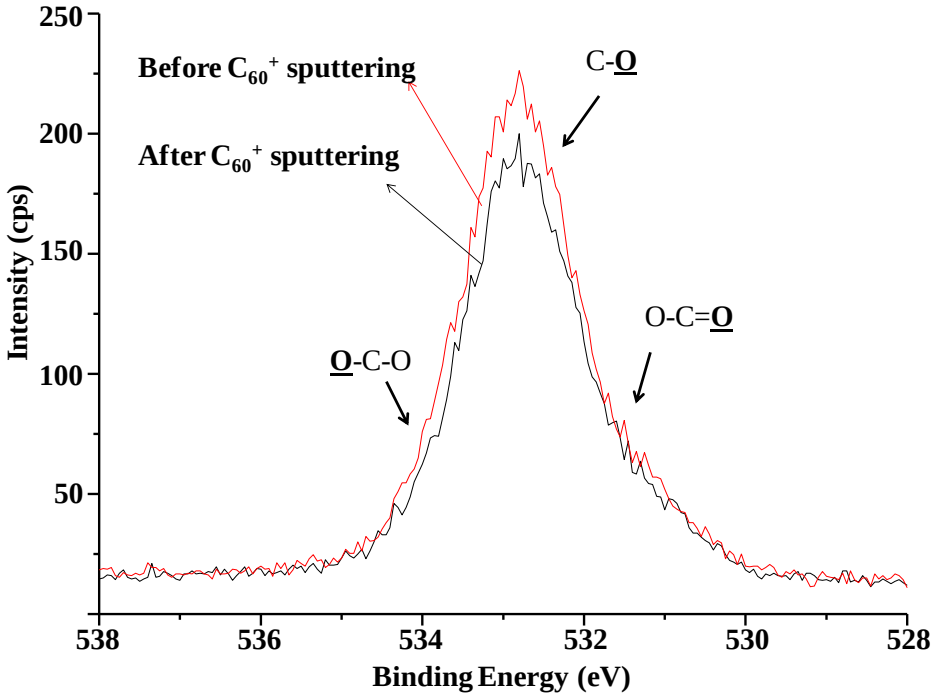

Figure 14. O *1s* core level spectra of polyelectrolyte multilayer before and after C_{60}^{+} sputtering indicating no significant chemical damage.

A polyelectrolyte multilayer consisting of 20 alternating layers of alginate and chitosan with Br_2Y incorporated at fifth, tenth and fifteenth layer from the air-multilayer interface was sputtered by C_{60}^{+} ion beam for a total of 90 minutes with XPS analysis performed after every 5 minutes of sputtering. This procedure was used because. C_{60}^{+} ion current produced from the home built sputter source was inconsistent with time, making it difficult to evaluate the exact time period of sputtering required to reach a particular depth within the multilayer. Figure 15 shows the Br ($3d^{5/2}$ and $3d^{1/2}$) spectra of the polyelectrolyte multilayer after C_{60}^{+} sputtering for 30

min, 45 min and 90 min detecting Br_2Y at different depths in the multilayer. A prominent Br signal from the fifth layer was observed after 30 min of sputtering, however only a weak signal corresponding to Br from the tenth and fifteenth layer were observed after sputtering for 30 min and 45 min. This lower sensitivity of detection after prolonged C_{60}^+ sputtering can be attributed to the mixing of alginate, Br_2Y-alginate and chitosan layers by the C_{60}^+ beam, similar mixing of the layers were reported during C_{60}^+ ion sputtering of polytetrafluoroethylene surface.[78] Also the inconsistency in C_{60}^+ ion current with respect to time can contribute a significant effect on the sputter rate, resulting in uneven removal of the multilayer over course of time.

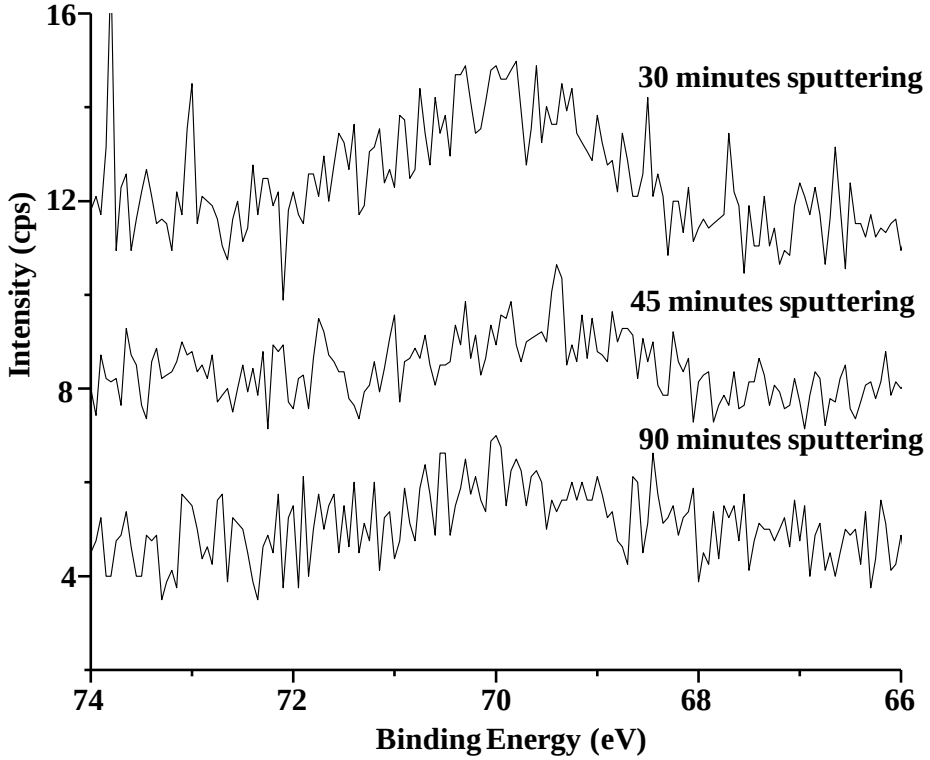

Figure 15. Br ($3d^{5/2}$ and $3d^{1/2}$) XPS core level spectra recorded at different time points for a 20 layer polyelectrolyte multilayer with Br_2Y incorporated at fifth, tenth and fifteenth layer from the air sample interface. Signal observed after 30 min sputtering is identifiable, but the signal after 45 min and 90 min sputtering are barely identifiable.

D. Conclusions

Polyelectrolyte multilayer with Br_2Y incorporated at different depth as a probe molecule was amenable for depth profiling using C_{60}^+ sputtering in conjunction with XPS to a depth of only fifth layer, with identifiable signal observed only from the fifth layer, however the data obtained after consecutive sputtering to probe Br_2Y at tenth and fifteenth layers were very hard to interpret. Furthermore due to the instability in C_{60}^+ ion current produced by the home built C_{60}^+ sputter source with time, no attempt was made to determine the depth of resolution for C_{60}^+ sputtering. The results however demonstrate that C_{60}^+ sputtering does not impart any significant chemical damage to the multilayer surface and hence can be used to probe small molecular analytes in particular Br_2Y at different depths in a multilayer system, since polyelectrolyte multilayer has a close resemblance to the bacterial biofilms[53, 79, 80] C_{60}^+ sputtering in conjunction with XPS has a greater potential to be extend for depth profiling studies in bacterial biofilms, however use of a stable C_{60}^+ sputter source and a sensitive topological tool like atomic force microscopy (AFM) in conjunction,[15] can be invaluable especially in determining the depth of erosion from C_{60}^+ sputtering.

IV. DETECTION OF BROMINATED TYROSINE IN POLYELECTROLYTE MULTILAYERS BY LDPI-MS AND SIMS

A. Introduction

In this study two methods for MS imaging analyses are explored for polyelectrolyte multilayer samples: LDPI-MS[35, 36] and SIMS.[23, 85] Recent LDPI-MS work has focused on SPI with 7.87 eV VUV radiation because it is available from a convenient laboratory source – the molecular fluorine laser. However, its 7.87 eV photon energy is below the ionization energy of many analytes, limiting the potential targets that it can ionize.

10.5 eV VUV radiation from the 118 nm ninth harmonic of the Nd:YAG laser has historically been the most popular VUV source for SPI because of its ability to ionize a much larger class of molecular analytes while avoiding detection of water, carbon dioxide and other abundant species usually of little interest to MS imaging.[22] However, the 10.5 eV source suffers from a relatively low energy, ~nJ energy per pulse which limits sensitivity and precludes its use in commercial instruments.

The question arises as to what VUV photon energies are most effective for postionization. Photon energies that are slightly above the ionization threshold of a molecular analyte have most often been considered ideal for LDPI-MS as they minimize the excess energy available for parent ion dissociation.[22, 23] Different photon energies for SPI can readily be accessed at a VUV synchrotron light source.[25, 36, 85, 86]

Another issue that arises in MS imaging is the difficulty of establishing analysis protocols on complex, heterogeneous biological samples. This difficulty has led to the use of organic multilayer models to evaluate the suitability of SIMS protocols for analysis of intact biological samples. SIMS studies of organic multilayer models have included Langmuir-Blodgett films of

barium arachidate,[62] dipalmitoyl-phosphatidylcholine-sucrose multilayers[63] and peptide doped trehalose thin films.[15]

A polyelectrolyte multilayer (PEM) model was applied here that is particularly well-suited to evaluate MS imaging protocols for bacterial biofilms. The composition and features of PEM were described in detail in Chapter 2 and Chapter 3. The PEM model also allowed introduction of small molecular analytes into the PEM, simulating the presence of metabolites, signaling molecules, and other species present within actual biofilms. Here, the small molecular analyte was Br_2Y, which was electrostatically adsorbed to every alternating alginate layer of the PEM. The presence of bromine and the unique isotopic pattern of Br_2Y facilitated identification by MS.

This study examined LDPI-MS of neat Br_2Y films, neat PEMs, and PEMs with adsorbed Br_2Y (Br_2Y-PEMs). 25 keV Bi_3^+ SIMS was also performed on these samples, given the several prior studies that used SIMS to study biofilms.[15, 82-84]

MS analysis was performed using a commercial SIMS instrument additionally configured for LDPI-MS by coupling to desorption laser and a tunable VUV synchrotron beamline.[47, 85, 87] Samples were also analyzed with a home built LDPI-MS that utilized a 7.87 eV molecular fluorine laser for postionization.[35] IE of Br_2Y were determined experimentally and compared to IE from electronic structure calculations. The results are discussed in terms of SPI mechanisms and desorption of Br_2Y, both from neat films and PEMs.

B. Experimental Details

1. Preparation and Verification of Br_2Y Films, PEMs, and Br_2Y-PEMs

Br_2Y films were prepared from solutions in (1:1 v:v) acetonitrile:water that were dried on gold-coated silicon substrates.

PEMs were prepared on gold-coated substrates as described previously in chapter 2. PEMs were verified by attenuated total reflection Fourier transform infrared spectroscopy. Elemental content of the PEMs was determined by monochromatic X-ray photoelectron spectroscopy using instrumentation and procedures previously described in Chapter 2.

20 mg/ml CHCA matrix solutions were prepared in (7:3 v:v) acetonitrile:trifluoroacetic acid (0.1% v:v). These matrix solution were then sprayed onto a subset of the PEMs to facilitate desorption during 7.87 eV LDPI-MS.

2. LDPI-MS and SIMS Instrument

LDPI-MS investigations described in this chapter were recorded using a custom built 7.87 eV LDPI-MS instrument at the University of Illinois at Chicago and 8.0 to 12.5 eV LDPI-MS at the Advanced Light Source (Lawrence Berkeley National Laboratory, Berkeley, CA). SIMS investigations were performed using a commercial SIMS instrument (TOF.SIMS 5, ION-TOF Inc., Munster, Germany) using 25 keV Bi^{3+} primary ions at the Advance Light Source (Lawrence Berkeley National Laboratory, Berkeley, CA) a detailed description of all the above instruments can be found in Chapter 2.

3. Electronic Structure Calculations

Calculations were performed using density functional theory with a commercial quantum chemistry software package (Gaussian 03, Pittsburgh, PA),[88] for different initial configurations of molecules and clusters. Calculations were carried out at DFT/ B3LYP level of theory with 6-311G basis set.[89-91] Vertical ionization energies (IEs) were calculated for molecules and clusters by initial geometry optimization, to determine the energy of the optimized neutral species. This was followed by energy determination of the anion species using the optimized neutral geometry.[89] Vertical ionization energy was then calculated using the equation below.

$$VIE = E^{+}(Geo=0) - E^{0}(Opt)$$

VIE: Vertical Ionization Energy

E^{+} (Geo = 0): Energy of the cation with optimized neutral geometry

E^{0} (Opt): Energy of the optimized neutral geometry

Vertical ionization energies (IEs) were calculated for Br_2Y, $[Br_2Y]_2$, $[Br_2Y][H_2O]$ and $[Br_2Y][H_2O]_3$. The $[Br_2Y][H_2O]_3$ cluster was chosen as an intermediate species representative between what is expected to be highly abundant $[Br_2Y][H_2O]$ and the much larger clusters thought to form in MALDI.[92, 93] The optimized geometries in the ground state shown in Figures 16 to 19 were used to calculate the vertical IEs by freezing the geometries and removing one electron from the highest occupied molecular orbital. All calculations were performed at the B3LYP/6-311+G** level and were corrected for zero point energy on the structures shown in the Figures 16 to 19 that represented local minima on their respective potential energy surfaces.

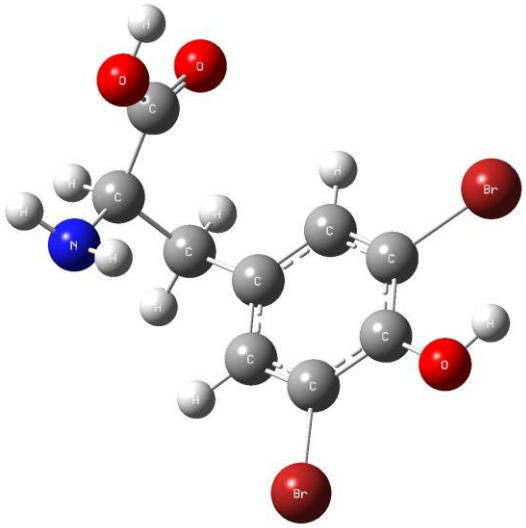

Figure 16. Optimized geometry of Br_2Y.

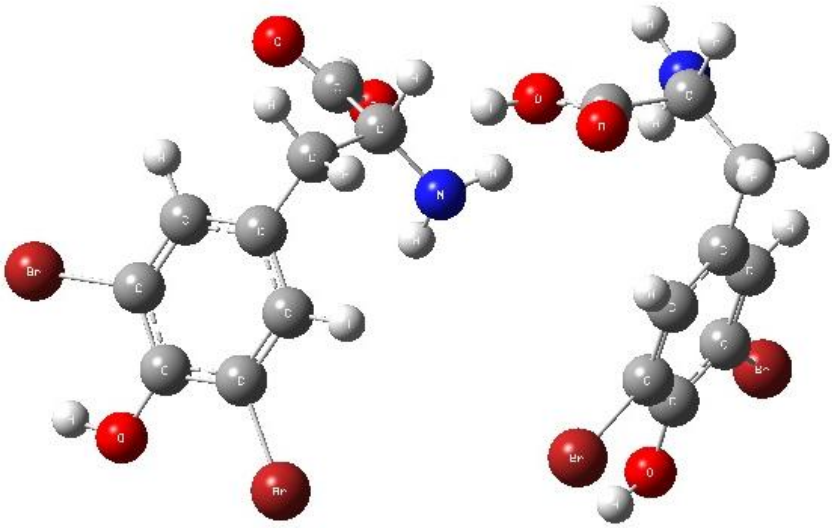

Figure 17. Optimized geometry of $[Br_2Y]_2$.

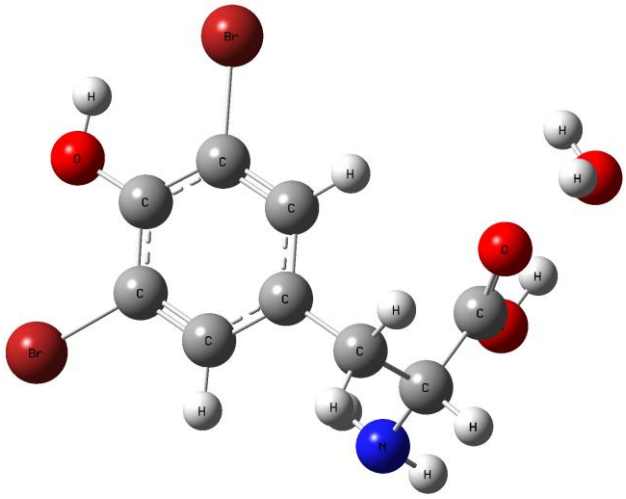

Figure 18. Optimized geometry of $[Br_2Y][H_2O]$.

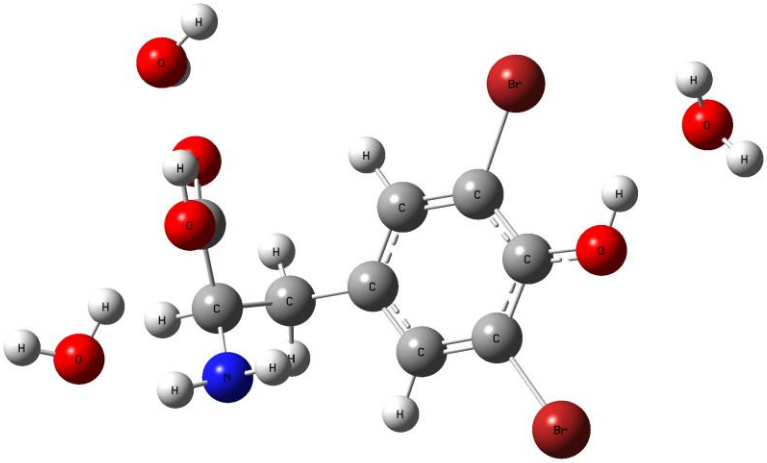

Figure 19. Optimized geometry of $[Br_2Y][H_2O]_3$.

C. Results and Discussion

1. Single Photon Ionization of Evaporated and Laser Desorbed Br_2Y Films

The first experiments were designed to evaluate VUV SPI of Br_2Y. Figure 20 shows the photoionization efficiency curve of evaporated Br_2Y which was recorded by monitoring the parent ion at *m/z* 337 while sweeping the VUV photon energy from the synchrotron. The experimental IE of Br_2Y of 8.3±0.1 eV was determined from the extrapolation of the photoionization efficiency curve using the drawn lines and agreed well with the 8.3 eV IE determined by electronic structure calculations.

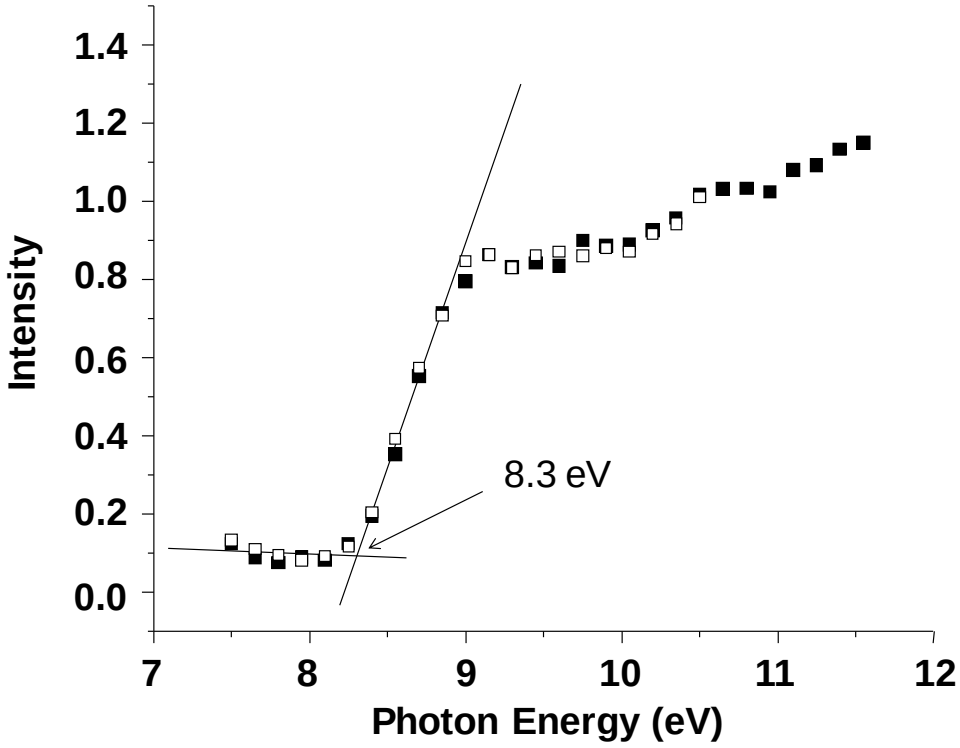

Figure 20. Photoionization efficiency curve for Br_2Y thermally desorbed from pure films recorded by sweeping the VUV photon energy while monitoring the *m/z* 337 parent ion. Intensities normalized to data collected at 10.5 eV photon energy. Lines are extrapolations indicating 8.3±0.1 eV experimental ionization energy. The different symbols correspond to different runs.

Full SPI-MS were also recorded at each photon energy point on the curve in Figure 20 and two of these spectra, recorded at 9.45 and 11.5 eV photon energies, are shown in Figure 21. 9.45 eV corresponds to ~1.1 eV internal energy deposited into the parent ion (the photon energy minus the ionization energy) while 11.5 eV corresponds to ~3.2 eV internal energy in the parent ion. The increase in internal energy significantly enhanced fragmentation in the parent ion at the higher photon energy, as expected.

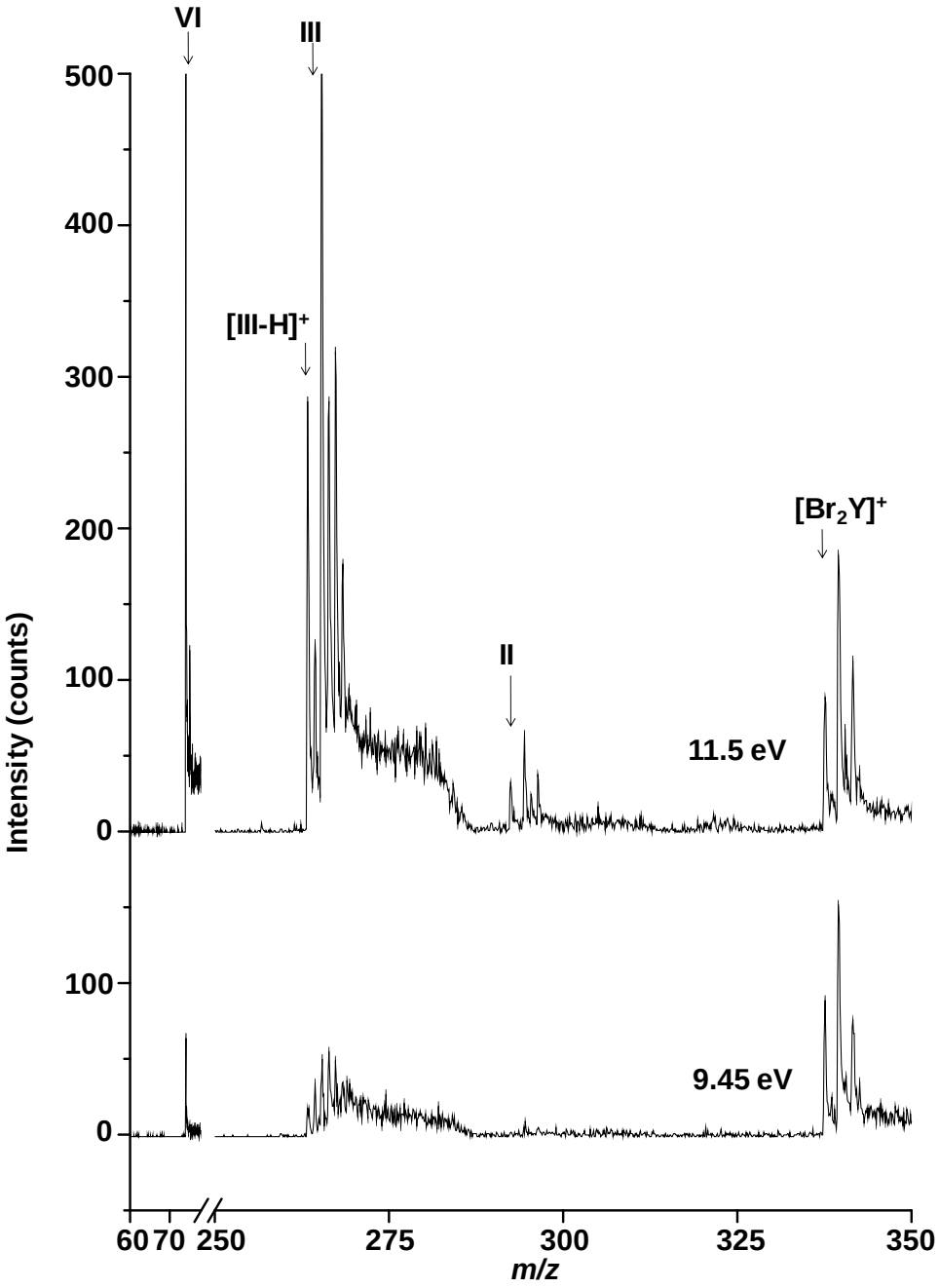

Figure 21. 9.45 and 11.5 eV photon energy SPI-MS of Br_2Y using synchrotron radiation.

Several of the fragments observed in SPI-MS of evaporated Br_2Y are similar to those from LDPI-MS of Br_2Y films described below (see Figure 23). Figure 22 identifies each of these fragments by a Roman numeral and illustrates the proposed fragment structures. All Br-containing peaks are referred to below by their lowest mass isotopes (i.e., those composed of ^{12}C, ^{79}Br, and ^{1}H) and were verified by the unique 1:0.97 isotopic pattern for ^{79}Br:^{81}Br (see below). Specifically, the II, III, and VI fragments identified in Figure 23 were observed along with the parent ion by SPI-MS and ≤8.0 eV LDPI-MS. However, little to none of the I, V, and IV fragments observed by LDPI-MS were detected by SPI-MS. Furthermore, SPI-MS additionally detected a deprotonated III fragment ion, denoted as $[III-H]^+$ in Figure 21, which was not observed at all in LDPI-MS. There were also significant differences in the fragment/parent ion ratios between LDPI-MS and SPI-MS: the (II/parent) and (III/parent) ratios were much higher in LDPI-MS than in SPI-MS, indicating a greater extent of fragmentation in the former and differences in fragmentation mechanisms between the two cases. Finally, there were no cluster ions observed by SPI-MS, unlike the case for LDPI-MS (Figure 24).

Br_2Y films on gold-coated substrates were laser desorbed and the resultant gaseous neutrals photoionized by VUV radiation and detected by time-of-flight MS. Figure 23 displays the LDPI-MS of Br_2Y films recorded using both 7.87 eV laser and 8.0 eV synchrotron photoionization. Both display characteristic fragments and clusters of Br_2Y.

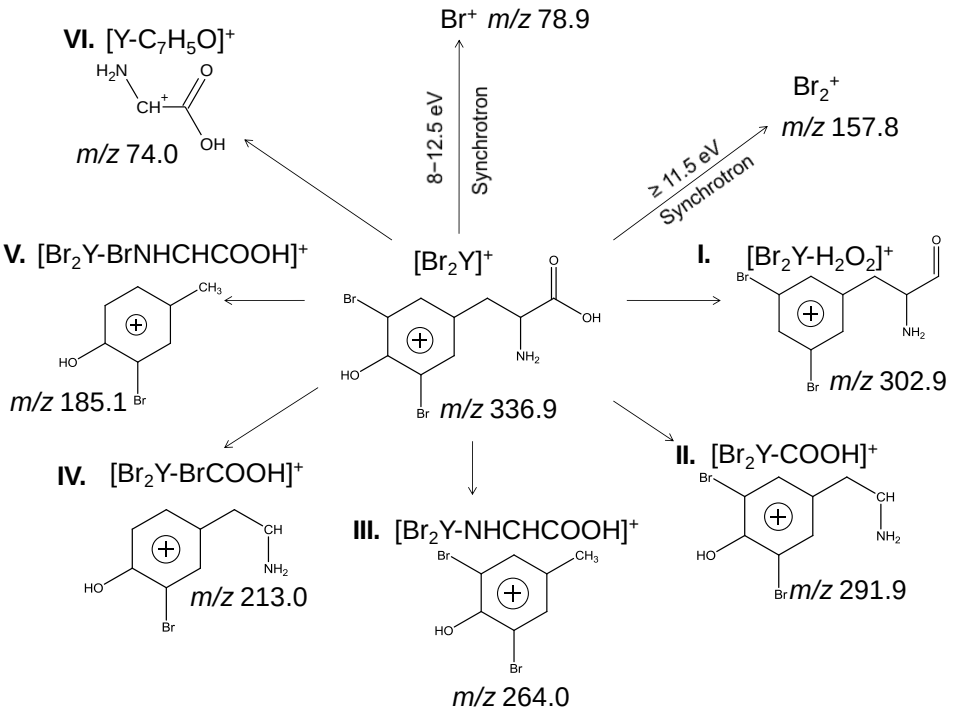

Figure 22. Schematic diagram of the fragmentation of Br_2Y by 7.87 eV laser and 8 - 12.5 eV synchrotron LDPI-MS, with Roman numerals identifying fragment ions. Br^+ and Br_2^+ were only observed by synchrotron photoionization at the noted photon energies.

Control experiments showed no significant ion signal from Br_2Y films except in the presence of both VUV radiation and the desorption laser (LD). This fact was demonstrated by the data in Figure 23 labeled “VUV only” and “LD only”, neither of which display any significant ion signal. Thus, few volatile species were detected by SPI at room temperature in the absence of laser desorption and little direct ionization occurred in the sole presence of the desorption laser.

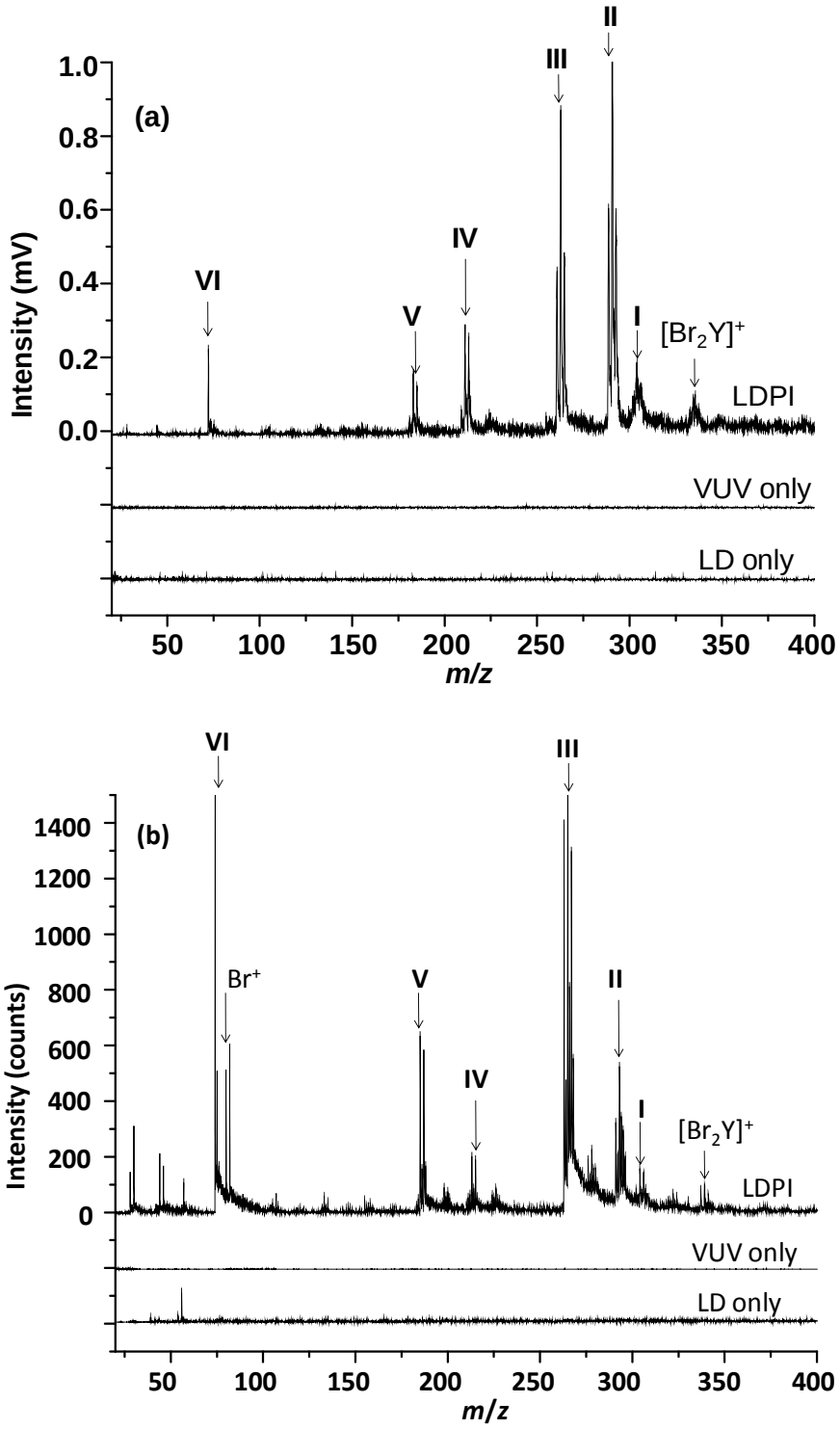

Figure 23. (a) 7.87 eV laser and (b) 8.0 eV synchrotron LDPI-MS of Br_2Y films: low mass range. The fragment ion structures associated with the Roman numeral labels are given in Figure 22.

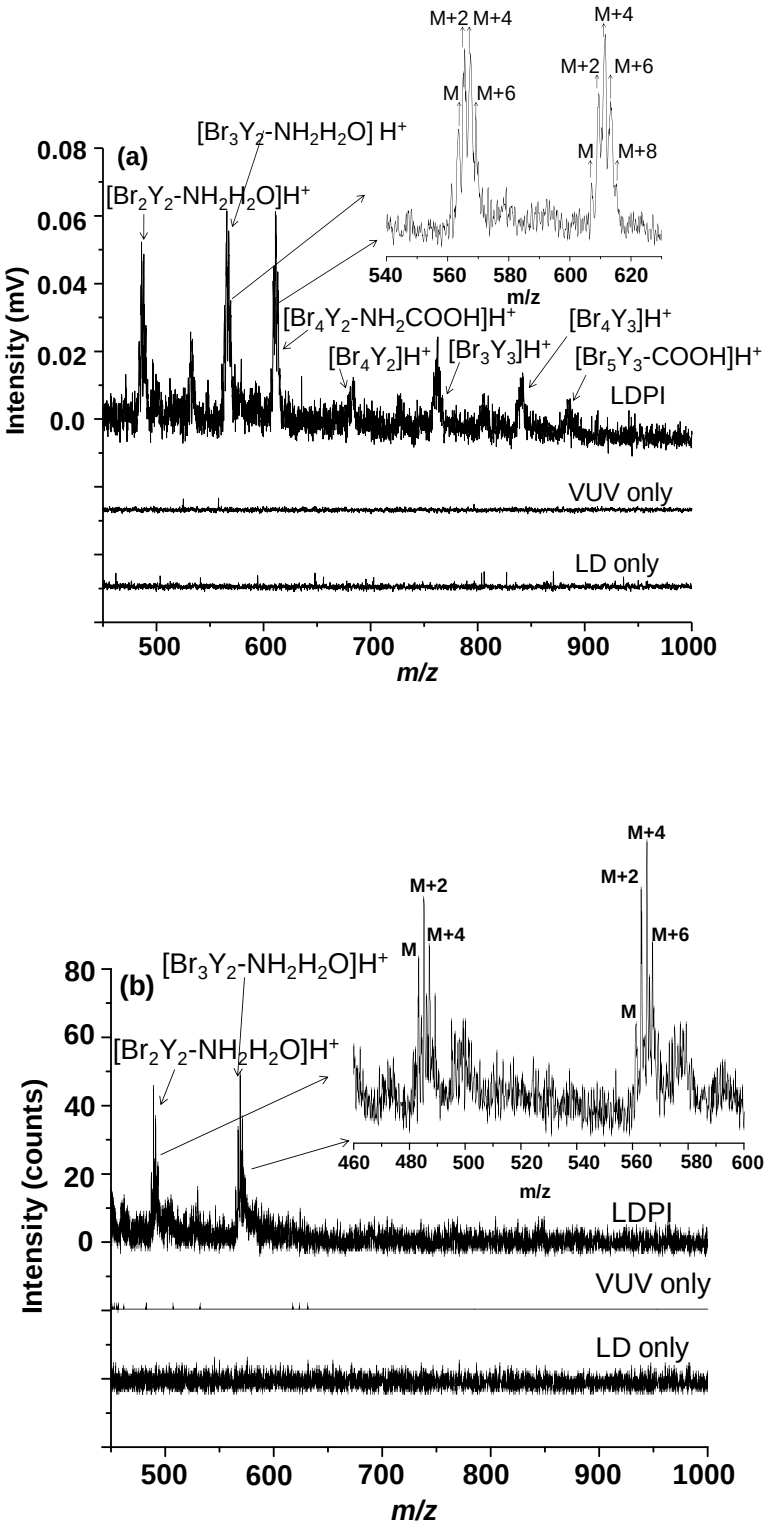

Figure 24. (a) 7.87 eV laser and (b) 8.0 eV synchrotron LDPI-MS of Br_2Y films: high mass range.

The $[Br_2Y]^+$ parent ion at *m/z* 336.9 along with various low mass fragments of Br_2Y appear in both the 7.87 eV laser and 8.0 eV synchrotron LDPI-MS in Figure 23. *M/z* 302.9 (I) was attributed to the parent ion after loss of H_2O_2. *M/z* 291.9 (II) was attributed to loss of COOH via cleavage of the α C-C bond. *M/z* 264.0 (III) was attributed to loss of NHCHCOOH via cleavage of the β C-C bond. These observations were consistent with prior VUV SPI studies that found amino acids predominantly undergo cleavage via the C-C bonds that are α and β to the terminal carboxyl group.[94-97] *M/z* 213.0 (IV) and *m/z* 185.1 (V) underwent similar cleavages with the additional loss of Br (losses of BrCOOH and BrNHCHCOOH, respectively). The charge resided on the aromatic group for most of these fragment ions due to charge stabilization via delocalization.[96] However, some fraction of β C-C bond cleavage led to the charge residing on the carboxyl group and produced the *m/z* 74.0 (VI) ion.

Some differences were observed between LDPI-MS using 7.87 eV laser and 8.0 eV synchrotron photoionization. The relative abundances of fragment ions differed with photoionization source and desorption conditions. *M/z* 291.9 (II) appeared as the most intense peak by 7.87 eV laser photoionization while *m/z* 264.0 (III) was the most intense peak by 8.0 eV synchrotron photoionization. However, the most significant difference was the sole appearance of Br^+ in the 8.0 eV synchrotron photoionization, as discussed further below.

Certain higher mass ions attributed to clusters of Br_2Y were also observed at both 7.87 eV laser and 8.0 eV synchrotron photoionization energies, as shown in Figure 24. The peak envelope in Figure 24(a) at *m/z* 561.8, 563.8, 565.8, and 567.8 with peak intensity ratios 1:3:3:1 matched with *m/z* and isotopic distribution for $[Br_3Y_2\text{-}NH_2H_2O]H^+$, the dimer of Br_2Y after loss of Br, NH_2, and H_2O. The other cluster at *m/z* 482.9 was assigned as $[Br_2Y_2\text{-}NH_2H_2O]H^+$. These clusters were detected by both 7.87 eV laser and 8.0 eV synchrotron photoionization.

The appearance of the aforementioned ions in Figure 24 confirmed cluster formation during laser desorption from pure films of Br_2Y. Pure analyte and analyte/solvent cluster formation also explained the appearance of ion signal for the parent ion and fragments thereof (Figures 23a and 22), despite the fact that the 7.87 photon energy was lower than the ~8.3 eV experimental IEs of Br_2Y. Electronic structure calculations found IEs of 7.8 eV for $[Br_2Y]_2$, 8.1 eV for $[Br_2Y][H_2O]$ and 7.9 eV for $[Br_2Y][H_2O]_3$. These calculated IEs indicate that clustering between Br_2Y monomers or with water lowered their IEs below that of the monomer. Thus, the lower IEs of pure Br_2Y clusters and/or $[Br_2Y]_m[H_2O]_{n>1}$ and their dissociation following photoionization enabled the detection of Br_2Y by 7.87 eV laser LDPI-MS, leading to essentially all of the ion signal observed in both Figures 23a and 24a.

Molecular dynamics simulations and experimental probes of the evolution of a desorption plume in the MALDI process showed that pulsed laser irradiation results in the ejection of a mixture of individual molecules, clusters, and microdroplets.[92, 93] Previous studies also showed that IEs of clusters of pure analyte or analyte-solvent are substantially lower than their corresponding monomers. For example, clusters of proline and 2,5-dihydroxybenzoic acid displayed lower IEs than the free matrix or proline[98] as did cytosine dimers compared to monomers[99] and water clusters compared to isolated water molecules.[100, 101] All of this prior work supports the cluster desorption/photoionization mechanism proposed here.

Another aspect of the clusters that Br_2Y forms with itself and/or water was that many, if not all, were protonated. Prior SPI of formic acid and water clusters found that protonated species dominated.[102, 103] The two cluster species detected by both laser and synchrotron VUV SPI, $[Br_2Y_2\text{-}NH_2H_2O]H^+$ and $[Br_3Y_2\text{-}NH_2H_2O]H^+$, were both protonated. Thus, all higher mass

clusters observed solely in laser VUV SPI were also assigned as protonated, although their signal to noise ratios were insufficient to assign *m/z* values with <1 *m/z* accuracy.

The 7.87 laser LDPI-MS showed a ~0.05 ratio of clusters to fragments, indicating a dominance of fragments in the spectra. The low excess energy available from threshold single photon ionization at 7.87 eV of clusters was insufficient to lead to such extensive cluster fragmentation. This is supported by the 9.45 eV SPI-MS of evaporated Br_2Y, which showed little fragmentation (Figure 21). However, cluster fragmentation would have been aided by the additional internal energy imparted by laser desorption. Furthermore, single photon ionization of clusters could have lead to structural rearrangement and proton transfer to form some of the fragment ions depicted in Figure 22. Nevertheless, the details of cluster fragmentation remain unresolved: further experiments and calculations are needed to validate ion structures and fragmentation mechanisms.

The low photon energy and narrow bandwidth of the 7.87 eV laser support the ionization mechanism via lowered cluster IEs. However, the case with the 8.0 eV synchrotron LDPI-MS of the Br_2Y films in Figures 23b and 24b is less clear. The slightly higher 8.0 eV photon energy and the 0.2 eV bandwidth of the synchrotron radiation[47] left open the possibility of some threshold single photon ionization of Br_2Y and $[Br_2Y][H_2O]$. Furthermore, some signal may have resulted from a minor amount of photoelectron ionization[104] or higher VUV harmonics leaking through the gas filter in the synchrotron beamline causing photoionization, as discussed previously.[105] However, the similarity of the fragments and clusters for both 7.87 eV laser and 8.0 eV synchrotron radiation and the similar cluster to fragment ratios (except as noted below) argued for a common ionization mechanism.

Nevertheless, there were several significant differences between 7.87 eV laser and 8.0 eV synchrotron radiation of Br_2Y films. The high mass Br_2Y spectra showed a higher mass distribution of clusters for 7.87 eV laser photoionization. These higher mass clusters included the intact protonated dimer, $[Br_4Y_2]H^+$, the trimer after a single Br loss, $[Br_5Y_3]H^+$, and fragments thereof. The source of this difference was not determined, but likely resulted from differences in either desorption/ionization conditions and/or TOF collection/transmission efficiencies between the two instruments.

Another significant difference between the Br_2Y spectra from the two photoionization sources was the observation of a peak at *m/z* 78.9 due to Br^+ only for 8.0 eV synchrotron photoionization (Figure 23). This result led to experiments in which the tunability of synchrotron radiation was exploited to record the LDPI-MS of Br_2Y films at photon energies above 8.0 eV (Figure 25). Increasing the photon energy from 8.0 to 12.5 eV showed only modest changes in the fragmentation pattern for Br_2Y, which remained different from those of 11.5 eV SPI-MS of evaporated Br_2Y. However, the signal intensity for all fragments did increase with photon energy, presumably due to a corresponding increase in the photoionization cross sections of the desorbed clusters.

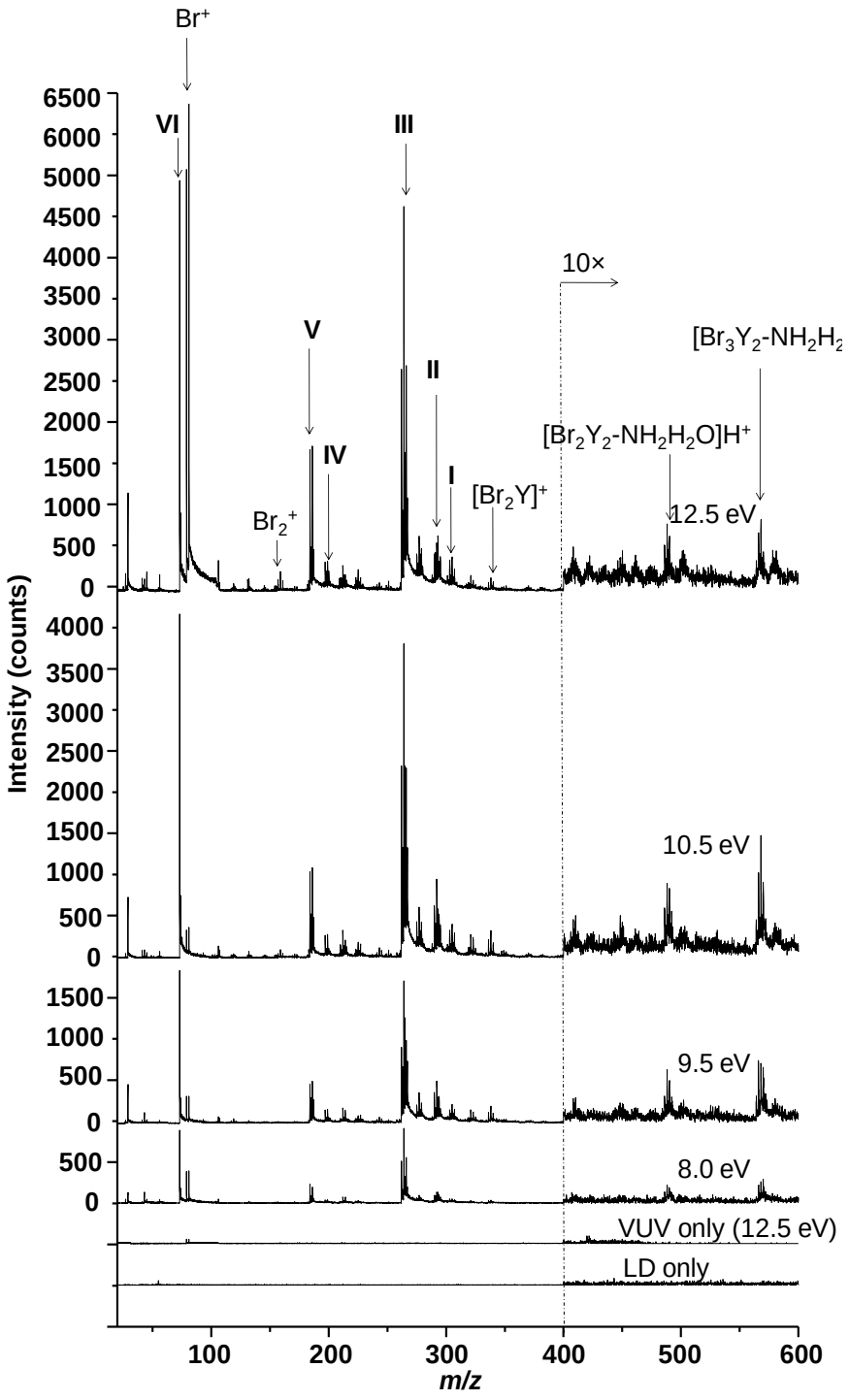

Figure 25. LDPI-MS of Br_2Y films recorded with 8.0 - 12.5 eV photon energies produced at the synchrotron. The "VUV only" spectrum was recorded with 12.5 eV photons, but without laser desorption while the "LD only" spectrum is recorded with the desorption laser but without any photoionization.

Intense signals for both Br^+ at *m/z* 78.9 and Br_2^+ at *m/z* 157.8 were observed at photon energies in excess of their ionization energies of 11.81 and 10.52 eV, respectively. The 349 nm wavelength of the desorption laser is sufficient to induce photodissociation of various organic bromides via the C−Br bond whose ~3 eV bond energy is readily cleaved to form bromine and carbon radicals.[106, 107] Br_2 could have formed from surface adsorbed Br that recombined during laser induced thermal desorption, analogous to the formation of O_2 by laser induced thermal desorption of atomic oxygen on metal surfaces. Examination of the time evolution of the Br and Br_2 signal (data of spectra versus laser shot recorded from a single sample spot not shown) indicated a relative increase in their signal over time compared to the Br_2Y fragment ions and clusters. This time evolution supported a Br_2Y degradation mechanism for the formation of Br and Br_2. This degradation might also explain some of the differences in fragment ratios between laser and synchrotron photoionization.

Neither Br nor Br_2 was detected by 7.87 laser photoionization (see Figure 23). Br_2^+ was only observed by synchrotron photoionization with photon energies at and above the 10.52 eV Br_2 IE. However, Br^+ was observed with 8.0 eV synchrotron radiation and at other photon energies below the 11.81 eV ionization energy of the Br atom: it may have formed by the same low photon energy mechanisms discussed above for the experiments using synchrotron radiation.

2. LDPI-MS of Polyelectrolyte Multilayers: Neat PEMs and Br_2Y-PEMs

The above results established the ability of VUV SPI to detect Br_2Y as neat films, so the next step was to examine the conditions required to detect Br_2Y adsorbed into PEMs. These Br_2Y-PEMs and also neat PEMs (without Br_2Y) were analyzed by LDPI-MS using both 7.87 eV laser and 11.5 eV synchrotron photoionization, with the higher photon energy chosen at the synchrotron for its large expected photoionization cross sections.

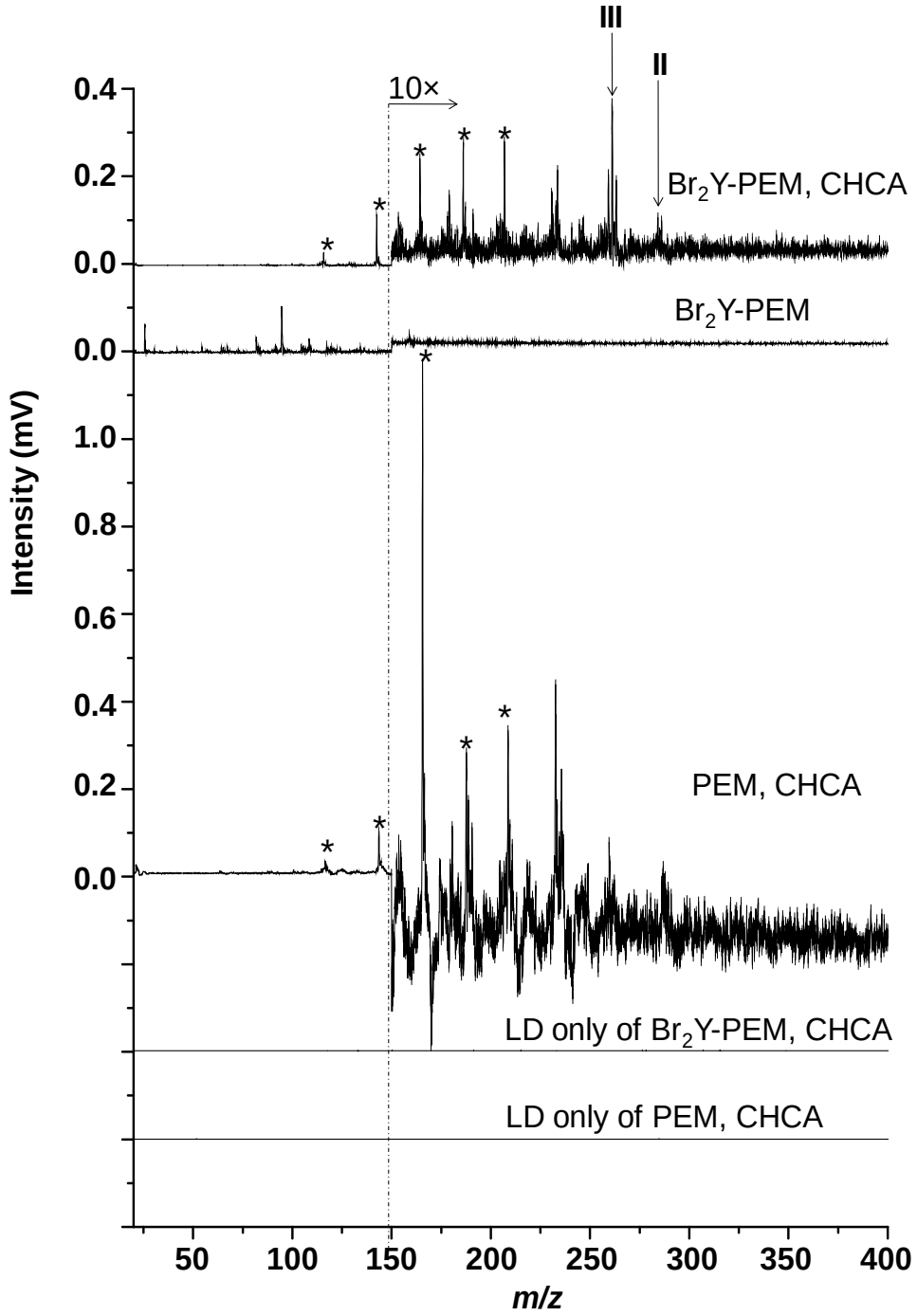

Figure 26. 7.87 eV laser LDPI-MS of Br_2Y-PEM (top trace) with CHCA matrix; (second trace from top) without CHCA, but with Br_2Y; and (third trace from top) with CHCA, but without Br_2Y. The corresponding LD only of samples containing matrix are also shown. CHCA-only associated peaks marked with asterisks.

Figure 26 shows 7.87 eV laser LDPI-MS of Br_2Y-PEMs, analyzed with and without CHCA matrix added to the fully prepared multilayer prior to MS analysis. The CHCA-treated sample allowed matrix-assisted laser desorption of neutral species, which produced *m/z* 264.0 (III) and *m/z* 291.9 (II) ions upon single photon ionization. These two ions were previously observed as the most intense ions formed from the neat Br_2Y films (see Figures 22 and 23). The ion observed at *m/z* 189.0 in Figure 26 was attributed to the CHCA parent ion and *m/z* 210 was attributed to the $[CHCA{\cdot}Na]^+$ complex while *m/z* 145.6 and several lower *m/z* peaks were assigned as CHCA fragments. All CHCA-only peaks are marked with asterisks in Figure 26.

The spectrum of the Br_2Y-PEM without matrix shows no Br_2Y-attributed peaks. Rather, it only displays peaks below *m/z* 150, none of which were assignable to any characteristic fragment of Br_2Y. The various controls supported these results. The spectrum of PEM with CHCA displays only matrix-associated peaks. LD only of both Br_2Y-PEM and neat PEM without the VUV laser showed no signal either with or without added CHCA matrix, indicating that direct ionization did not occur at these desorption laser peak power densities, which were similar to those used to analyze the pure Br_2Y films.

The inability to detect any Br containing species with 7.87 eV laser photoionization when no matrix was added raises the question of how much Br_2Y was actually adsorbed into the Br_2Y-PEMs. X-ray photoelectron spectra were recorded on equivalent Br_2Y-PEM samples and indicated a 0.7% bromine content, compared to a calculated value of 13% for a pure Br_2Y film. Thus, the Br_2Y-PEMs had ~5% of the total Br_2Y of pure films, yet no Br-containing species could be observed in the absence of matrix. This ~5% Br_2Y concentration was apparently insufficient to allow the cluster formation needed for 7.87 eV SPI under these desorption conditions. By contrast, the matrix facilitated desorption of pure Br_2Y clusters or mixed

Br_2Y/CHCA/water clusters, all of which were expected to display ionization energies below the 7.87 eV photon energy (see above). The applied matrix on the PEM probably also extracted some of the Br_2Y into a surface layer where it co-crystallized with the matrix and permitted matrix assisted laser desorption, as is thought to occur in standard MALDI-MS.[93]

Next, the ionizing photon energy was raised in an attempt to detect adsorbed Br_2Y in the Br_2Y-PEM without the addition of matrix. Br_2Y was detected by 11.5 eV synchrotron LDPI-MS, as manifested in the *m/z* 185.1 (V) and *m/z* 264.0 (III) peaks from the Br_2Y-PEM, as shown in Figure 27. Experiments were performed in which the desorption laser peak power density was increased, but it neither enhanced the useful III/V fragment signal nor brought out any other peaks that were clearly characteristic of Br_2Y (data not shown). Rather, higher desorption laser peak power densities only led to more PEM degradation as characterized by pyrolysis peaks appearing at almost every integer *m/z* value up to ~*m/z* 450.

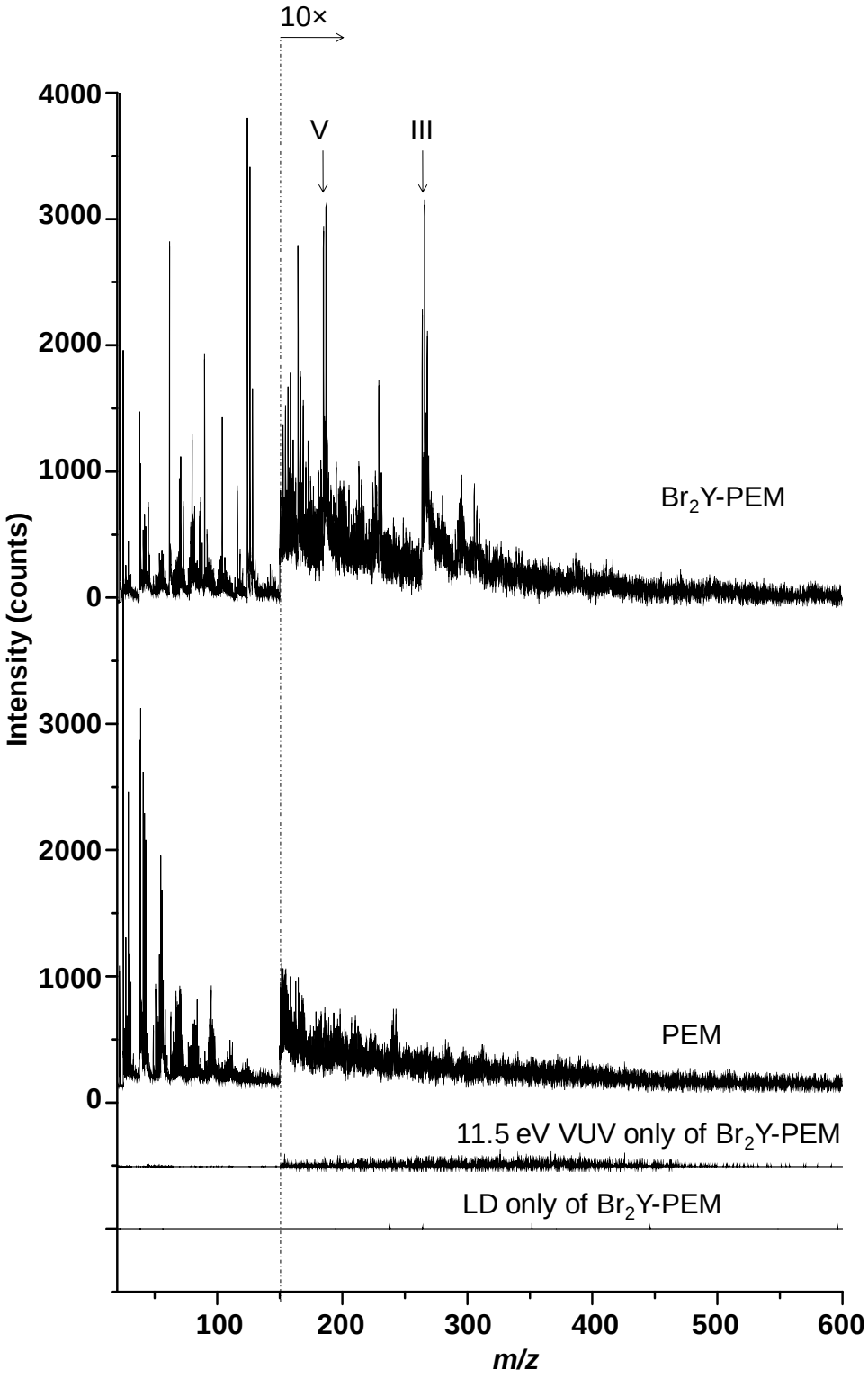

Figure 27. 11.5 eV synchrotron LDPI-MS of Br_2Y-PEMs and neat PEMs. The 11.5 eV SPI-MS and LD only mass spectra for Br_2Y-PEMs are also shown. No CHCA or other matrix was added.

3. SIMS of Br_2Y Films, Neat PEMs, and Br_2Y-PEMs

Films of Br_2Y, neat PEMs, and Br_2Y-PEMs were also analyzed by 25 keV Bi_3^+ SIMS. While the positive ion spectra was relatively uninteresting, as shown in Figure 28. Both spectra show several peaks that are characteristic to chitosan and alginate fragments: the peak at *m/z* 199.1 was attributed to the $[C_6H_8O_6Na]^+$ alginate monomer, *m/z* 125 to the $[C_3H_2O_4Na]^+$ alginate fragment, and *m/z* 97.2 to $[C_6H_9O]^+$ from both chitosan and alginate.[108, 109] Higher mass (as yet unidentified) fragments were also observed at *m/z* 250.2 and *m/z* 275, with additional lower mass peak groups below *m/z* 100 resulting from extensive chitosan/alginate degradation. However, SIMS of the Br_2Y-PEMs showed no evidence for the presence of Br^+ in the multilayer, where the vertical lines in the inset indicate where $^{79}Br^+$ and $^{81}Br^+$ would appear. Even the Br^+ region did not display any signal unique to the Br_2Y-PEM. While the Br_2Y-PEM did show unique peaks at *m/z* 111.6 and 137.8, these lacked the characteristic isotopic distribution for bromine and therefore could not have resulted solely from any Br-containing fragments of Br_2Y.

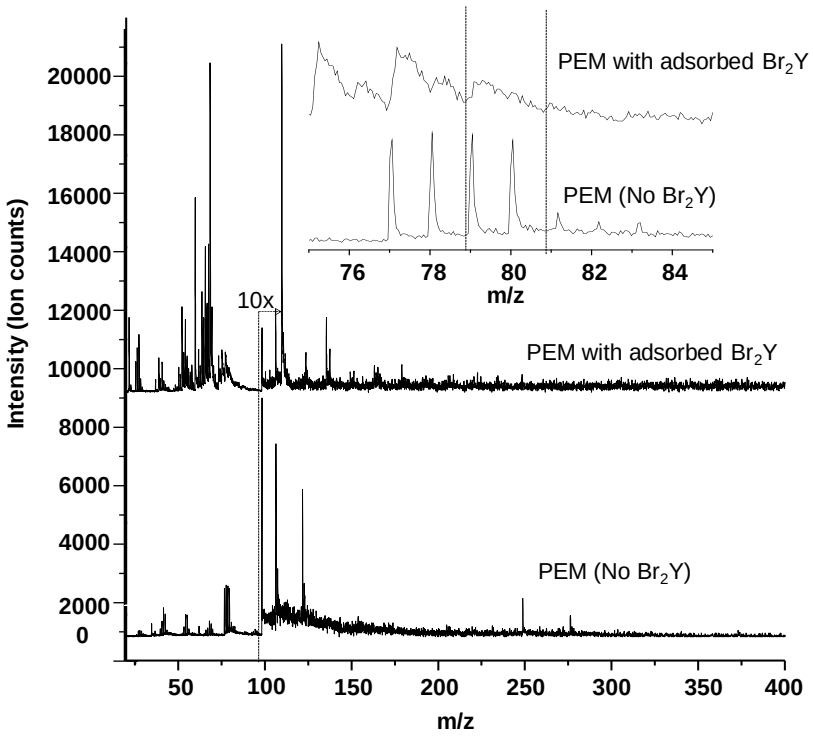

Figure 28. Positive ion 25 keV Bi_3^{2+} SIMS of PEM and Br_2Y-PEM. Vertical lines in inset indicate where $^{79}Br^+$ and $^{81}Br^+$ would appear.

The negative ion SIMS of the Br_2Y films and Br_2Y-PEMs in Figure 29 display significant useful signal. The negative ion SIMS of the Br_2Y films displayed the $[Br_2Y]^-$ parent ion at *m/z* 336.9, and strong Br^- and Br_2^- peaks. Several other Br_2Y-related peaks also appeared including one at *m/z* 262.9 that was similar to the structure III (see Figure 22) minus a proton, denoted as $[III\text{-}H]^-$ in Figure 29. Other Br_2Y characteristic ion appeared at *m/z* 249.9 that was attributed to the III structure without the CH_2 group and denoted as $[III\text{-}CH_2]^-$. The clusters of peaks near *m/z* 290 were attributed to an overlap of the II ion and the II ion minus a proton, $[II\text{-}H]^-$. The peak at *m/z* 275.9 was attributed to $[II\text{-}NH_2]^-$. Thus, SIMS observed several fragments not seen in LDPI-MS. No ions were observed in the negative ion SIMS with structures related to the I, IV, V, or VI ions observed in LDPI-MS. Finally, the peak at *m/z* 417.8 also appeared related to Br_2Y and

was tentatively assigned to $[Br_2Y][HBr]^-$, although at least one other assignment related to fragments of dimerized Br_2Y was also feasible.

The Br_2Y-PEMs also displayed the $[Br_2Y]^-$ parent ion and Br^-, but did not display the structurally intact (II/III related) fragments of Br_2Y that were observed for the negative ion SIMS of the neat Br_2Y films. However, other Br-containing ions were observed including *m/z* 157.8 corresponding to Br_2^-, *m/z* 180.8 corresponding to $[Br_2Na]^-$ and *m/z* 283.5 corresponding to $[Br_3Na_2]^-$. Br_2Y-PEM also showed a peak at *m/z* 359.4 assigned to $[Br_2Y][Na]^-$ and several other peaks up to *m/z* 550 with characteristic bromine isotopic patterns indicative of other $[Br_2Y][Na_xBr_y]^-$ or $[Na_xBr_y]^-$ structures. Some of the most prominent ions in the negative ion SIMS of the Br_2Y-PEMs showed high sensitivity to Br, but these atomic $[Na_xBr_y]^-$ clusters contained little information on the analyte's chemical structure. That these various negative ion adducts containing Na appeared only in the Br_2Y-PEM spectra was attributed to the presence of excess sodium from the sodium alginate used in their preparation and/or a unique desorption event facilitated by the PEM (or the complexation of Br_2Y therein). The neat PEMs showed none of the above mentioned peaks associated with Br_2Y (see Figure 29).

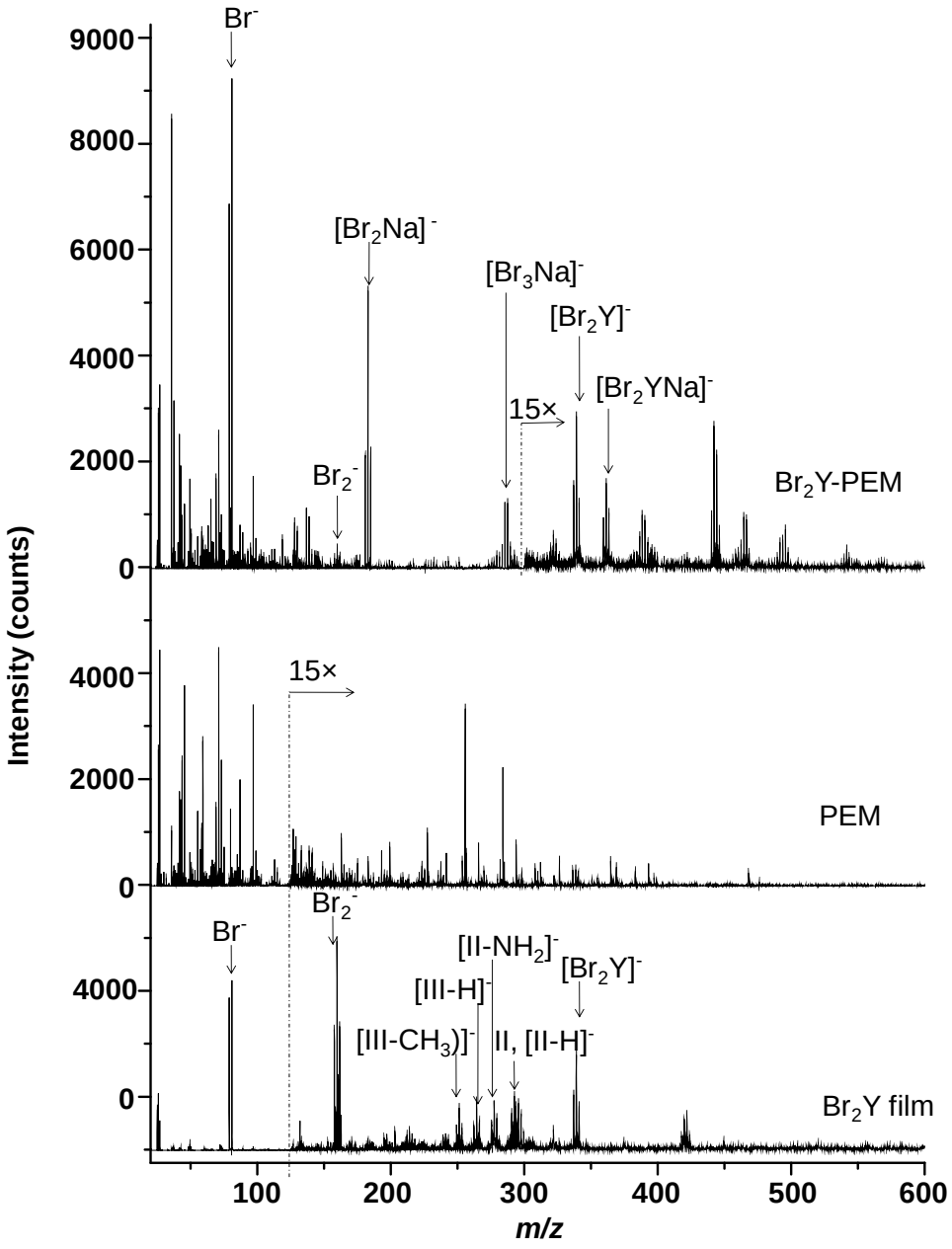

Figure 29. 25 keV Bi_3^+ SIMS negative ion spectra of a Br_2Y film, neat PEM, and Br_2Y-PEM.

D. Conclusions

These results demonstrated several points of significance to the application of VUV SPI to MS imaging. It has usually been considered necessary for the VUV photon energy to exceed a molecular analyte's ionization energy to allow SPI.[22] However, the lower ionization energy of pure analyte, analyte/solvent, or analyte/matrix clusters that form during laser desorption can permit SPI at lower photon energies.[98, 99, 110] The practical implication of this observation is that the fluorine excimer laser might be much more widely useful for VUV postionization in MS imaging, as it can detect some species with ionization energies above its 7.87 eV photon energy when they cluster.

Cluster formation does require a relatively high density of gaseous species that could be laser desorbed only from pure films or polyelectrolyte multilayers pretreated with matrix. Thus, even the relatively high (~5%) fraction of adsorbed Br_2Y in the polyelectrolyte multilayers was insufficient to produce clusters upon laser desorption unless CHCA matrix was added prior to analysis. The application of matrix was also thought to facilitate extraction of adsorbed Br_2Y from within the multilayer while also enhancing the explosive desorption known to occur in MALDI.[92, 93] Desorption was enhanced by matrix even though desorption laser peak power density was kept low enough to minimize direct ion formation via proton transfer. Nevertheless, Br_2Y was detectable from multilayers without added matrix when higher photon energies were employed for SPI.

The positive ion spectra from Bi_3^+ SIMS produced few useful results for these samples, showing mostly monomers of the polysaccharides (Figure 28).[108, 109] However, the negative ion spectra were analytically quite useful. Like many organohalides, Br_2Y has a high electron affinity, which is expected to enhance negative ion formation.[111] However, most non-

halogenated analytes have low electron affinities and may not produce as useful a negative signal. Furthermore, there was a strong dependence of the analyte's condensed phase environment upon the negative SIMS, with the neat films displaying major differences from the multilayer spectra.

Finally, a few observations can be made regarding the comparison of LDPI-MS with SIMS. SIMS permits much higher spatial resolution for MS imaging of ~100 nm, compared with a spatial resolution of ~20 μm for LDPI-MS, similar to that observed for MALDI-MS.[7] Both methods formed significant parent ions from the pure Br_2Y films, albeit via different ionization pathways. However, the SPI event in LDPI-MS formed additional fragment and cluster ion species not observed in SIMS. The difference in spectra from the two methods was even greater for the Br_2Y-PEMs, mostly due to differences in the extent and type of fragmentation and clustering. It can be concluded that LDPI-MS and SIMS will generally provide complementary chemical information due to their different ionization mechanisms. Furthermore, the ability to tune the ionization event by selection of photon energy in SPI adds an added dimension of selectivity to LDPI-MS that is not directly available in SIMS. This work has refrained from comparisons of sensitivity between LDPI-MS and SIMS, as the former was performed using novel experimental configurations that are the subject of ongoing improvements.

V. IDENTIFICTION AND IMAGING OF PEPTIDES AND PROTEINS ON *ENTEROCOCCUS FAECALIS* BIOFILMS BY MALDI-MS

A. Introduction

Peptides and proteins are often used as biomarkers in bacterial identification by mass spectrometry.[112, 113] Matrix assisted laser desorption ionization mass spectrometry (MALDI-MS) is well established for the identification of bacterial strains via protein profiling.[114-116] Sequencing peptides or proteins using tandem MS and comparing the data with protein databases can reliably identify bacterial species and overcome the limitations of earlier MS-based methods.

The study of protein expression from bacterial biofilms has typically required the separation of proteins from disaggregated biofilms,[113] a strategy which loses all information on their spatial distribution within intact biofilms. Imaging proteomics is a MS imaging technique which gives relative abundance and spatial localization of proteins throughout a biological sample.[1, 7, 117] When imaging proteomics employs trypsin digest of proteins to peptides, as is frequently the case, identical strategies can be subsequently employed to detect both peptide fragments of proteins and peptides native to a biological sample. Secondary metabolites, endogenous molecules, antibiotics, peptides, and other small molecules have been imaged within intact bacterial colonies by MALDI-MS,[118-120] laser desorption postionization MS,[22, 35, 121] and other MS imaging methods.[1, 37]

Relatively little work has been reported on in situ imaging proteomics of intact bacterial biofilms, perhaps due to several challenges that must be overcome. Bacterial cells are much smaller than eukaryotic cells.[122] Furthermore, the microbes in bacterial biofilms are typically enclosed in an extracellular polysaccharide matrix which hinders easy access for protein digestion and identification. Relatively few bacterial strains have the fully sequenced genomes

needed to facilitate protein identification, although new bacterial genomes are reported regularly. However, bacteria have the advantage of much smaller proteomes compared with eukaryotes.

Imaging proteomics can be performed using either a top down or a bottom up approach.[123-125] The top down approach identifies low molecular weight proteins by direct MS fragmentation without any preliminary digestion.[123, 126] The bottom up approach digests samples prior to MS analysis by depositing trypsin solutions as separate, <200 µm droplets which confines protein digestion and prevents diffusion of digested peptides beyond individual droplets. This strategy aids identification of proteins and permits simultaneous localization of their constituent peptides. Imaging proteomics by the bottom up approach previously demonstrated the feasibility of direct protein identification and imaging in tissues of eukaryotic organisms. On-tissue MALDI-MS analysis of rat brain tissue sections was performed directly from individual trypsin digested spots to identify and localize several proteins.[127] Formalin-fixed paraffin embedded rat brain tissues samples were analyzed by MALDI-MS imaging to correlate protein identification and molecular imaging.[128] Tissue digestion combined with MALDI-ion mobility MS has also been used for protein identification and imaging directly on rat brain and human cerebellum tissues.[129]

Traditional proteomics requires proteins be extracted, purified, and concentrated prior to their identification. Imaging proteomics is performed with fewer sample preparation steps and without any protein extraction or concentration steps. However, the imaging technique appears limited to relatively high abundance proteins, at least in mammalian tissues.[127-129]

Direct analysis and in situ trypsin digestion of intact *Enterococcus faecalis* biofilms was combined here with MALDI-MS imaging to identify one peptide and over a dozen proteins, establishing the feasibility of imaging proteomics to study biofilms of prokaryotic organisms. *E. faecalis* is an opportunistic pathogen which is a natural inhabitant of the mammalian

gastrointestinal tract and oral cavity. It is known to be a major cause of infections of the urinary tract, respiratory tract, wounds, and root canal.[130, 131] *E. faecalis* is known to withstand oxidative stress, desiccation and extreme temperature and pH. It also displays high endogenous resistance to salinity, bile acids, detergents and antimicrobials.[130] In particular, the V583 strain of *E. faecalis* is resistant to the antibiotic vancomycin and was the first vancomycin-resistant clinical isolate reported in the U.S.A.[132] The ability of *E. faecalis* V583 to acquire resistance against most effective antibiotics has attracted global attention.[133] Another reason to focus on this strain is that the V583 genome has been completely sequenced, with a total of 3337 predicted protein-encoding open reading frames reported.[134] The V583 strain has at least 306 proteins predicted to be covalently anchored to the cell membrane and another 67 proteins non-covalently attached to the membrane.[135] These membrane and secreted proteins are known to play a vital role in cell adhesion, apart from their virulence properties.[136] Thus, the spatial localization of these proteins within intact biofilms may improve understanding of bacterial virulence mechanisms as a function of culturing conditions. Studies were also performed on biofilms of *Escherichia coli* (ATCC 25922) and a vancomycin-sensitive, virulent medical isolate strain, *E. faecalis* ATCC 29212 (39). MALDI-MS imaging was demonstrated on co-cultured biofilms of *E. faecalis* V583 and *E. coli*. The alternate organism of *E. coli* was chosen because of the synergistic interaction reported between the two strains, specifically the higher virulence of *E. faecalis* observed in association with *E. coli.*[137]

B. Experimental Details

1. Strains and Media

E. faecalis V583 (ATCC 700802), *E. faecalis* (ATCC 29212), and *E. coli* (ATCC 25922) were obtained commercially (American Type Culture Collection, Manassus, VA). *E. faecalis*

V583 planktonic culture was grown for 24 h in tryptic soy broth growth medium (Difco, Detroit, MI, USA) containing 10% (w/v) glucose (TSBG) for use in inoculation of drip flow biofilms. Similar cultures were used to inoculate TSBG-amended tryptic soy agar (TSA) for membrane biofilms. Planktonic cultures of *E. faecalis* (ATCC 29212) and *E. coli* were grown under similar conditions.

2. Plate and Membrane Biofilm Growth

Single species *E. faecalis* biofilms were grown either using a drip flow reactor or on polycarbonate membranes (Millipore, 0.20 μm pore size, 25 mm diameter, Fisher Scientific) described in detail previously in Chapter 2.

Drip flow biofilms were grown on sterile stainless steel MALDI plates mounted in the flow cell lanes of a sterile drip flow reactor (DFR) and was inoculated with 10^8 colony forming units (CFU) of *E. faecalis* V583. To allow initial adhesion of the cells to the MALDI plates, the reactor set-up was incubated for 24 h at 37°C and kept flat without any inclination upon addition of 20 mL of TSBG growth media to each of the flow cell lanes. After 24 h of static growth, the drip flow reactor was assembled completely with its stand tilted at an angle of 10°. TSBG growth medium was delivered at a flow rate of 3.6 mL/h for three days using a peristaltic pump to each of the flow cells. At the end of three days, biofilms grown on MALDI plates were rinsed with 50 mM ammonium bicarbonate (BICAM) solution (pH 8), followed by submersion in 50 mM BICAM containing 0.5 M sucrose for 2 h, then drying at room temperature prior to further processing.

Membrane biofilms were grown on sterile polycarbonate membranes inoculated with either vancomycin-resistant *E. faecalis* V583 or with the vancomycin-sensitive ATCC 29212 strain of *E. faecalis* containing 10^6 CFU and grown in TSBG-TSA at 37°C for 7 days while replenishing

the agar plate daily. For co-cultured membrane biofilms, sterile polycarbonate membranes were inoculated with *E. faecalis* V583 and *E. coli* cultures containing 10^6 CFU. The two microbes were spotted at distinct points 3 mm apart on the same membrane, then grown in TSBG-TSA at 37 °C for 7 days while replenishing the agar plate daily. The two biofilms were observed to grow into one another after 7 days. Membrane biofilm growth was chosen over plate biofilms to avoid the practical difficulties associated with growing two species biofilms in a drip flow bioreactor.

3. Biofilm Preparation for MALDI Analysis

For top down proteomics, 5 mM dithiothreitol in water was twice sprayed on the dried plate biofilms using an airbrush (Testors Corp., Rockford, IL, USA) at 20 psi spray pressure followed by incubation at 37°C for 2 h to break the disulphide bonds in the proteins. Sinapinic acid matrix at 20 g/L concentration in 1:1 (v/v) acetonitrile:trifluoroacetic acid (TFA, 0.1% (v/v) in water) was then sprayed three times with approximately one min of drying time between each spray cycle using the airbrush (20 psi). The plate biofilms were then air dried at room temperature prior to MALDI-MS analysis.

For bottom up proteomics, after treating the plate biofilms with dithiothreitol, 1 g/L trypsin (Sigma-Aldrich) in BICAM was sprayed twice using the airbrush (20 psi) and incubated at 37°C for 24 h prior to spraying with α-cyano-4-hydroxycinnamic acid (CHCA, Sigma-Aldrich) matrix at 20 g/L concentration in 7:3 (v/v) acetonitrile:TFA (0.1% v/v in water) and air drying at room temperature prior to MALDI-MS analysis.

For peptide identification and imaging in single and two species membrane biofilms, membranes were removed from the agar plate and blotted on stainless steel MALDI plate, with care taken to maintain the spatial integrity of the biofilm cells during the transfer. CHCA matrix

at 20 g/L concentration in 7:3 (v/v) acetonitrile:TFA (0.1% v/v in water) was then sprayed on the sample and air dried at room temperature prior to MALDI-MS analysis.

4. MALDI-MS

MALDI-MS investigations described in this chapter were recorded using a commercial MALDI-MS instrument (4700 TOF/TOF, AB SCIEX, Foster City, CA, USA) under MS and MS/MS mode. A detailed description of the instrument conditions can be found in Chapter 2. Briefly helium was used as a collision gas for MS/MS experiments. Non MS imaging data were acquired by commercial software (4000 Series Explorer V3, AB SCIEX) while MS image acquisition was performed using open source software (4000 Imaging V3, http://maldi-msi.org) with a raster size of 150 μm and 255 laser shots per spot. The MS images acquired were processed further using open source software (BioMap V3803, http://maldi-msi.org).

5. Scanning Electron Microscopy

CHCA matrix sprayed biofilms were visualized by a scanning electron microscope (S-3000N, Hitachi) with a tungsten electron source operating at 15 keV under high vacuum. Rather than dehydrating by an alcohol/water gradient series, the wet biofilms were simply coated with platinum/palladium alloy.

6. Data Analysis for Peptide and Protein Identification

Proteins and peptides were only identified when they were detected in three replicate samples. MS imaging of co-cultured biofilms were repeated a minimum of three times with similar mass spectral images observed each time.

Protein database searching was performed using commercial software (MASCOT V 2.2.04 licensed to the University of Illinois at Chicago, National Center for Data Mining, P0127504). All monoisotopic MS/MS data were searched after conversion to MASCOT compatible using the

program (4000 Series Explorer V3, AB SCIEX). The entire NCBInr and SwissProt databases were searched using MASCOT without any enzyme, fixed or variable modification selected in the search criteria and the taxonomy selected as all entries (no species selection). The NCBInr database of *Enterococcus faecalis* V583 (downloaded from NCBI on January 25, 2011, with 6961 records in the database) was also searched. MASCOT searches were performed with a peptide tolerance of ±0.5 Da and a fragment mass tolerance of ±1.0 Da. Searches were performed with one variable modification which included acetylation of protein N-terminal and oxidation of methionines as well as with one missed cleavage and no fixed modifications (since no chemical modification was expected during digestion).

De novo peptide sequencing was performed using commercial software (GPS Explorer TM software-DeNovo Explorer version 3.0, build 291 licensed to The University of Illinois at Chicago). The sequencing was performed with a mass tolerance of ±0.1 Da and without any selection made for enzyme, fixed and variable modifications. Any peptides identified by *de novo* sequencing were also searched in the EMBL protein database without any species constraints (via MS BLAST similarity search in DeNovo Explorer).

C. Results

1. *In situ* Peptide Identification on Intact Biofilms

Biofilms of two different strains of *E. faecalis* V583 (ATCC 700802) and ATCC 29212 as well as that of *E. coli* (ATCC 25922), were used to test the specificity of species observed to *enterococci* species under various growth conditions. Figure 30 shows representative in situ MALDI-MS spectra for biofilms of *E. faecalis* V583 grown on a MALDI plate, *E. faecalis* ATCC 29212 grown on a polycarbonate membrane, and *E. coli* grown on a polycarbonate membrane. Both strains of *E. faecalis* biofilms displayed many of the same peaks, despite their

growth under different conditions. However, many of those *E. faecalis* peaks were absent in *E. coli.* Several *E. faecalis* species-specific peaks with ion counts greater than 500 were observed, including *m/z* 714.3, 747.4, 780.2 and 851.5. *M/z* 851.5 and several other peaks were also observed in planktonic cultures of both *E. faecalis* strains. A peak at *m/z* 673.3 was observed in both membrane biofilms of *E. faecalis* and *E. coli* species. The peak at *m/z* 655.7 was observed only in *E. coli*, but not in any *E. faecalis* biofilms.

MALDI-MS/MS (tandem MS) experiments for *E. faecalis*-specific peaks were performed for *de novo* sequencing. Figure 31 shows the MALDI-MS/MS spectra of *m/z* 851.5 with the peptide fragments assigned using the standard notation.[138] The peak at *m/z* 851.5 was identified by *de novo* sequencing to be the heptapeptide of primary sequence ARHPHPH with a 83.7 score. ARHPHPH is part of the primary sequence of κ-casein from Bison bonansus (European bison), specifically the f96 – 102 residues.[139]

De novo sequencing also showed that the *m/z* 780.5 peak corresponded to hexapeptide of sequence RHPHPH (83.6 score, data not shown). The only difference between this two peptide and ARHPHPH was the absence of the terminal amino acid residue alanine in the former. It follows that RHPHPH peptide at *m/z* 780.5 is also derived from κ-casein. However, it is unclear whether RHPHPH exists as a distinct species in cell culture or as only a fragment that subsequently only formed in the gas phase during MS analysis.

Both peptide sequences were further confirmed by trypsin digestion of the *E. faecalis* biofilms since trypsin cleaves peptides on the c-terminal side of lysine or arginine amino acid residues. Trypsin digestion decreased the intensity of the two peptide peaks (data not shown) which indicated the presence of an arginine residue in the sequences of *m/z* 780.5 and 851.5.

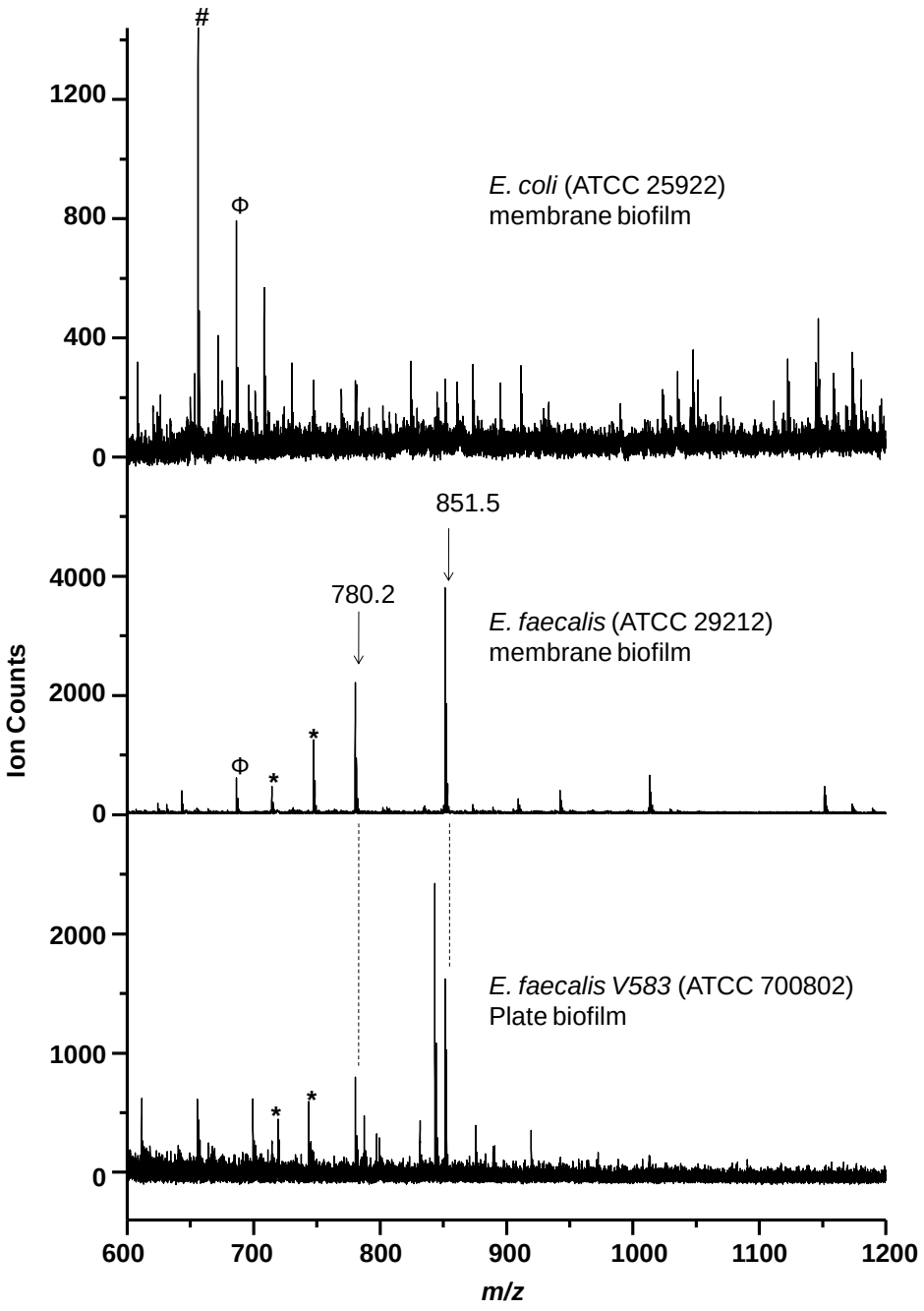

Figure 30. Representative in situ MALDI-MS spectra of *E. faecalis* plate biofilm (V583, bottom trace), *E. faecalis* membrane biofilm (ATCC 29212, middle trace) and *E. coli* membrane biofilm (ATCC 25922, top trace). *E. faecalis* species specific peaks are labeled and marked with asterisks, Peaks observed in both E. coli and *E. faecalis* membrane biofilms are marked with Φ (i.e., *m/z* 673.3). An *E. coli* specific peak is marked with # (i.e., *m/z* 655.7).

No peptide sequences or other chemical structures were assigned to any of the other peaks beyond for *m/z* 780.2 and 851.5. De novo sequencing of the unidentified *E. faecalis* peaks described above did not yield any unique peptide sequences with a reliable score, indicating that they may not be independent peptides. A regular neutral loss fragment pattern observed in their MS/MS data indicated these peaks might derive from muropeptides of peptidoglycans of *E. faecalis*. However no conclusive structures were derived for these or any other peaks from their MS/MS data alone.

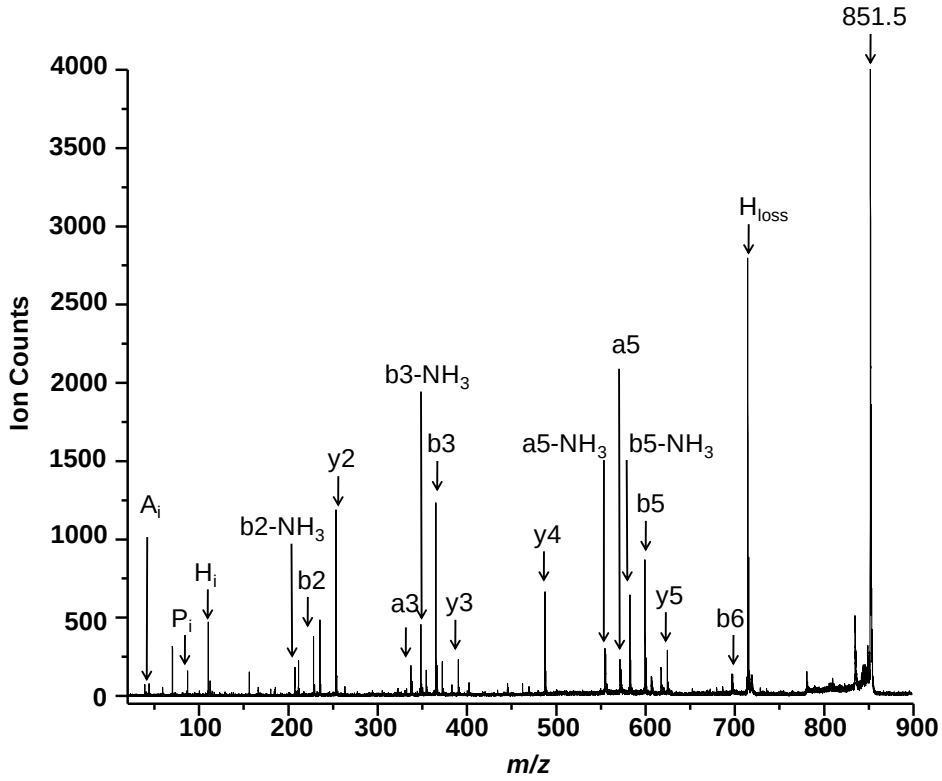

Figure 31. MALDI-MS/MS of *m/z* 851.5 observed in *E. faecalis* V583 membrane biofilm with peak assignments indicating the heptapeptide of sequence ARHPHPH.

2. *In situ* Protein Identification on Intact Biofilms

Figure 32 shows representative in situ MALDI-MS data from *m/z* 3000 to 8500 for proteins identified using the top down proteomics approach. The peaks at *m/z* 3412.6, 3605.7, 3662.2, 7182.0, 7207.8, 7308.2 and 7325.9 were observed with S/N >3: all were labeled based on the most intense peak observed in their isotopic distribution. No peaks were observed at higher masses. It was clear that the peak at *m/z* 3605.7 was a doubly charged peak of *m/z* 7207.8, based on the isotopic distribution. Two positive hits were observed when the MS/MS data were searched in the protein database using peptide mass fingerprinting (where a protein score greater than 51 was considered significant). This search identified two hypothetical proteins: EF1885 and EF1734 corresponding to *m/z* 3662.2 and 7325.9, respectively. These *m/z* values were lower by 975 and 839 Da than the reported masses of these proteins. The MS/MS data from other peaks did not yield a sufficient S/N ratio to generate any successful matches in the protein databases.

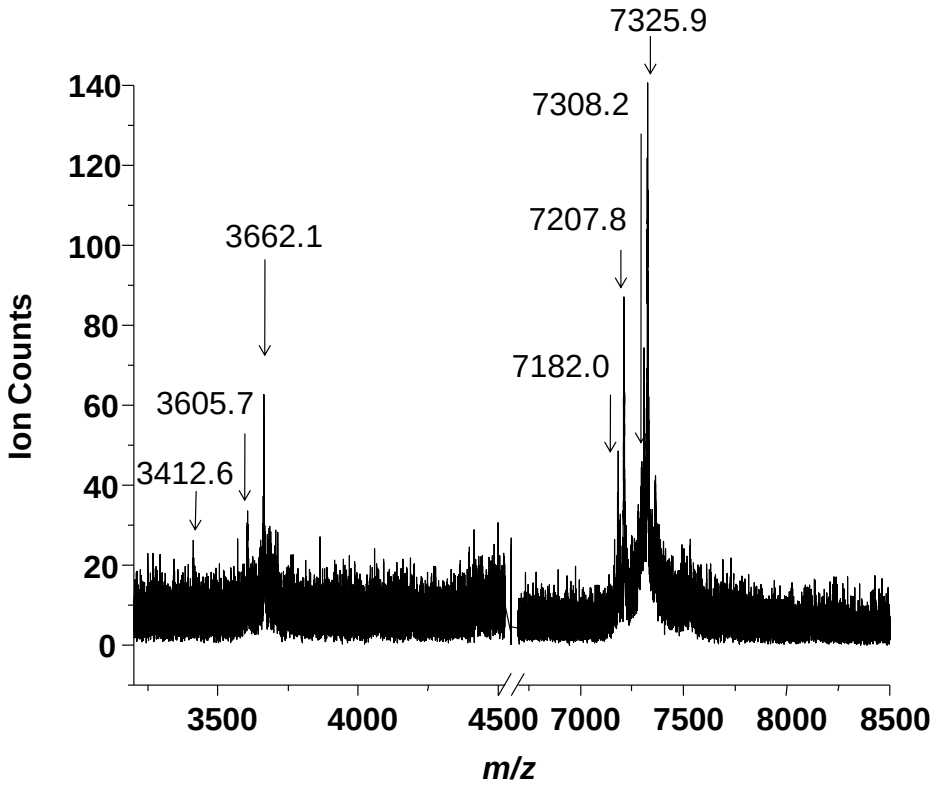

Figure 32. Typical *in situ* MALDI-MS of intact *E. faecalis* V583 biofilm.

Figure 33 shows a typical in situ MALDI-MS in the mass range *m/z* 500 to 2500 of an *E. faecalis* V583 biofilm for the bottom up proteomic approach with and without trypsin digestion. No peaks were observed at higher masses and matrix interference peaks dominated below *m/z* 500. The mass spectra of the trypsin digested biofilm (top trace of Figure 33) display several peptide peaks with varying intensities which were not observed in the undigested control biofilm (bottom trace of Figure 33).

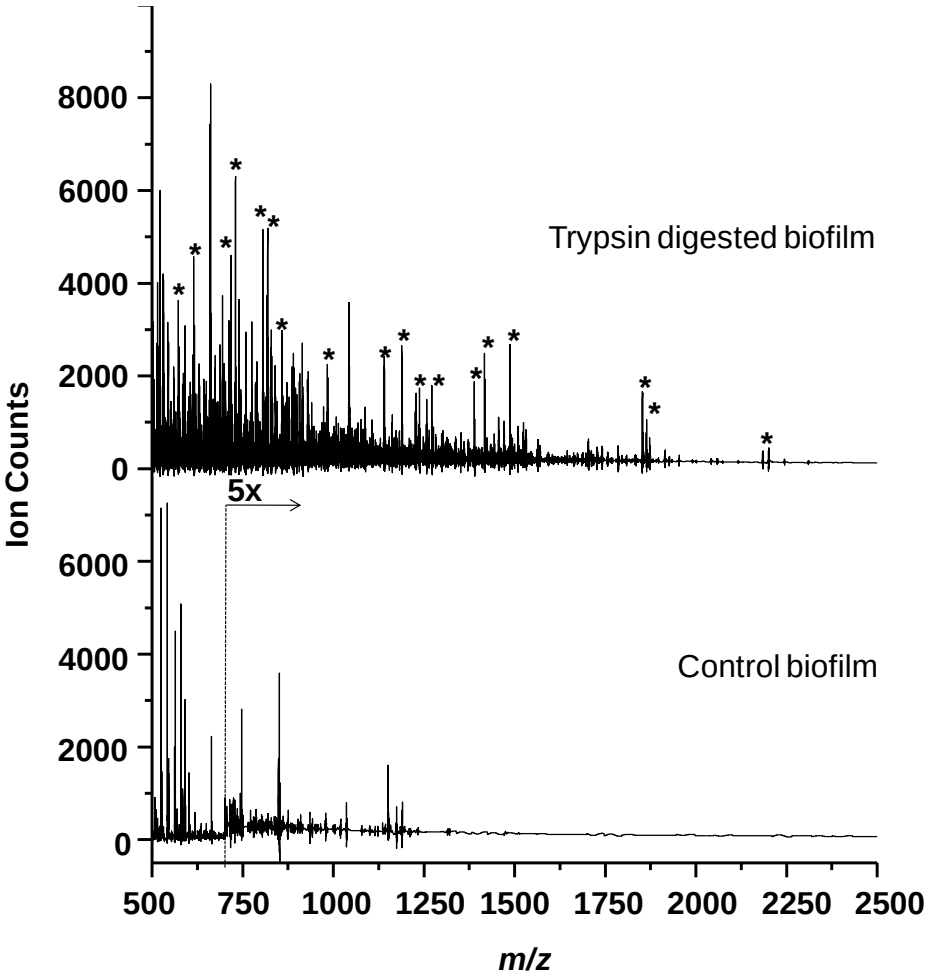

Figure 33. *In situ* MALDI-MS of *E. faecalis* V583 biofilm. top trace shows spectrum of biofilm digested with trypsin. Bottom trace shows spectrum of neat untreated control biofilm. Peaks arising after trypsin digest are marked with asterisks.

.

Eight peaks between *m/z* 500 and 1800 were also observed that might be associated with trypsin digested peptides. However, none of these peaks could be reliably assigned as they displayed low MASCOT scores due to low signal to noise, the primary sequences assigned via their MS/MS data were questionable, and/or they lacked of correlation with any protein in the database.

Top Down

Database	Sequence Reference	Protein ID	MASCOT score [(a)]	Sequence coverage (%)	Theoritical m/w
V583	gi/29376414	EF1885	65	100	4637
V583	gi/29376284	EF1734	104	100	8165

(a) Protein score greater than 51 are significant ($p<0.05$)

Bottom Up

Database	Sequence Reference	Protein	MASCOT score [(b)]	Peptide m/z used for protein identification	Theoritical mol. wt of the identified protein	Protein subcellular localization
V583	gi|29343947	enolase	68	717.4, 1188.6, 1851.9	46482	Cytoplasm
V583	gi|29343950	glyceraldehyde 3-phosphate dehydrogenases	47	749.4, 819.3	35749	Cytoplasm
V583	gi|29342693	tyrosyl-tRNA synthetase	37	1389.4, 1487.4	47231	Cytoplasm
V583	gi|29344777	hypothetical protein EF_2843	36	828.5	8359	Cytoplasm
V583	gi|29344997	BioY family protein	34	730.1	19446	Membrane
V583	gi|29342815	excinuclease ABC, subunit B	34	1701.8	76054	Cytoplasm
V583	gi|29344009	hypothetical protein EF_2033	34	788.4	4498	Cytoplasm
V583	gi|29342305	translation elongation factor Tu	32	1139.6, 1702.9, 1862.9, 2184.0	43361	Cytoplasm
V583	gi|29344612	helicase, putative, RecD/TraA family	32	1863	97416	Cytoplasm
V583	gi|29344600	spermidine/putrescine ABC transporter, permease protein	29	629.4	31484	Membrane
V583	gi|29344133	GTP-binding protein	28	712.1	46992	Cytoplasm

(a) Protein score greater than 26 indicate identity or extensive homology ($p<0.05$)

Table II. List of proteins identified on intact *E. faecalis* V583 biofilms by top down and bottom up proteomic approaches.

3. *In situ* MALDI-MS Imaging of Peptide

Figure 34 shows the MALDI-MS images of several different ion peaks in co-cultures of *E. coli* and *E. faecalis* V583 strains grown together until the two biofilms met at the interface: the *E. faecalis* ARHPHPH peak at *m/z* 851.5, an endogenous peak at *m/z* 673.3 observed in both species, and a peak at *m/z* 655.7 observed predominantly in the *E. coli* biofilm region. The MS images show the ARHPHPH peptide was observed only in the *E. faecalis* biofilm region and not

in the *E.coli* region. Both strains grew at approximately equal rates, but the MS images were cropped to emphasize the *E. faecalis* region.

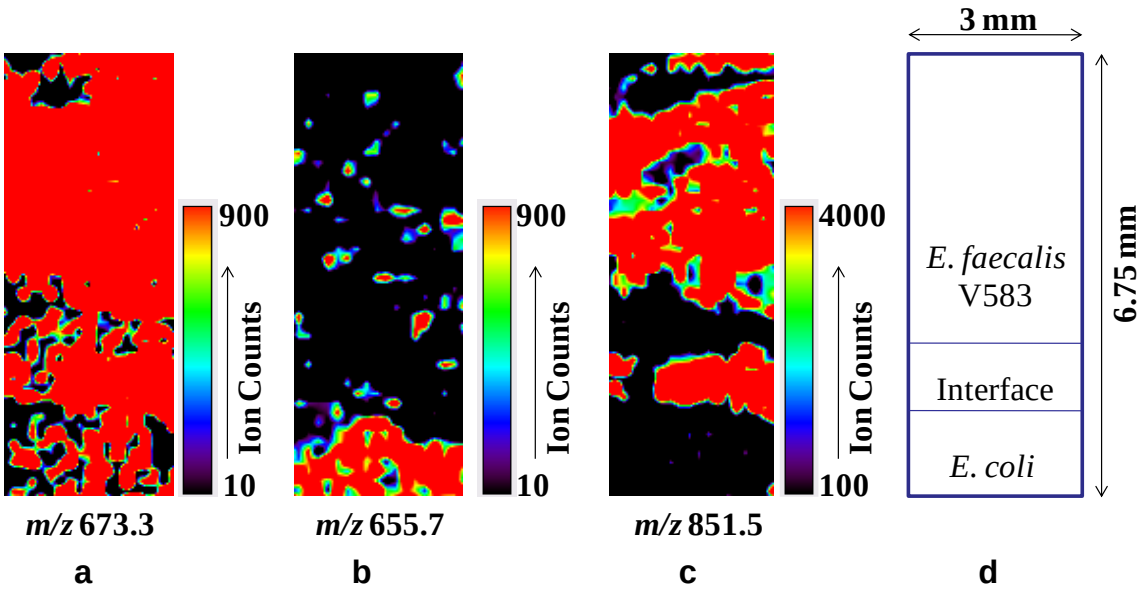

Figure 34. MALDI-MS images of co-cultured biofilms of *E. faecalis* V583 and *E. coli* showing spatial distributions of three ions: (a) *m/z* 673.3, an endogenous peak observed in both species, (b) *m/z* 655.7, an *E. coli* specific peak, and (c) *m/z* 851.5 corresponding to the ARHPHPH peptide from *E. faecalis*. (d) is a cartoon showing the relative positions of each strain in the co-culture and the absolute size of the images.

MALDI-MS images of trypsin digested peptides on intact *E. faecalis* V583 single species plate biofilms were also obtained (data not shown) to observe the spatial localization of the associated proteins. These results demonstrated the feasibility of imaging proteins on intact biofilms without involving any complicated sample preparation steps employed by traditional proteomics such protein extraction, purification, and/or concentration. Among the several proteins identified and imaged by MALDI-MS were BioY family protein (a biotin transporter), GTP binding protein (multifunctional protein family), tyrosyl-tRNA synthase (a protein synthesis associated protein), glyceraldehyde-3-phosphate dehydrogenase (a glycolysis enzyme

and possible cell surface virulence factor). Also the MS images of these proteins indicated that different proteins were expressed differentially within the biofilm as a result of heterogeneous environments.

MALDI-MS requires that a matrix compound be sprayed onto the biofilm surface and the presence of this matrix can affect the spatial resolution of MS imaging. The scanning electron micrograph of *E. faecalis* V583 biofilm sprayed with CHCA matrix showed the ~0.7 μm bacterial cells were apparent within the <10 μm matrix crystals (data not shown). However, the spatial resolution of ~150 μm for MS images acquired in this study was not dependent on the matrix crystal size, but rather on the laser spot size (~150 μm diameter) and the step size of MS image acquisition (also 150 μm).

D. Discussion

1. Summary of Results

The ARHPHPH heptapeptide was identified in both vancomycin-resistant and sensitive *E. faecalis* strains under a range of conditions including mono- and co-cultured biofilms as well as planktonic cultures. ARHPHPH was also imaged at the boundary of co-cultured, adjacent *E. faecalis* and *E. coli* biofilms, appearing only on the *E. faecalis* side. ARHPHPH was proteolyzed from κ-casein, a component in the growth media, by *E. faecalis* microbes. RHPHPH peptide was also observed, but it could not be determined if this peptide actually existed in culture or only formed during MS analysis. Several peaks specific to *E. faecalis* other than these two peptides were also observed, but their identities could not be confirmed by de novo sequencing. In addition, eleven different proteins were identified by the bottom up proteomics approach and two proteins were identified by the top down approach. Finally, the feasibility of imaging proteomics on intact *E. faecalis* V583 bacterial biofilms by MALDI-MS was also demonstrated.

2. Peptide and Protein Expression

ARHPHPH was found to be associated with *E. faecalis* biofilms and planktonic culture, but it does not represent any sequence in this organism's proteome. Rather, ARHPHPH corresponds to the f96 – 102 residues of κ-casein.[139] Casein is one of the components of the trytic soy growth media used here and prior work showed that many *E. faecalis* strains can proteolyze casein.[140] Thus, *E. faecalis* appears to be proteolyzing casein from the growth media to produce ARHPHPH, an observation that has not been previously reported. Other *enterococci* strains, *E. faecium* and *E. durans*¸ were also found to proteolyze casein, but the *E. faecalis* strains were report to be more active.[140]

The imaging of ARHPHPH on intact biofilms demonstrates the potential for MALDI-MS to study the spatial localization of peptides and proteins in their native form. As the *E. coli* strain examined here did not proteolyze casein, the ARHPHPH peak could be used to study the spatial interactions of *E. faecalis* with other microbial species. This is analogous to prior work where surfactin from *B. subtilis* co-cultured *S. aureus* used to map the chemistry associated with the phenotypes by MALDI-MS imaging, with higher concentration of the surfactin observed at the interface suggesting an inhibitory role against *S. aureus*.[119]

The eleven proteins identified in vancomycin-resistant *E. faecalis* V583 by the bottom up strategy include both cytosolic and membrane proteins (Table II).[135] Several of the cytosolic proteins have 'moonlighting' or multiple functional associations with the cell surface as reported for enolase and glyceraldehyde 3-phosphate dehydrogenase (GAPDH).[141, 142] These cell surface-associated, multiple function bacterial proteins can be virulence determinants playing important roles in interactions with the host, including adaptive responses to environmental changes, adherence, internalization, toxin synthesis, and escaping the host immune system.[135] For instance

in *Streptococcus agalactiae*, the cell surface localized GAPDH protein is reported to function as a virulence factor with B lymphocyte-modulatory activity, while in *Streptococcus oralis* it is reported to be important in colonization. In *Streptococcus suis* serotype 2, GAPDH is known to play a role in adhesion for cell binding and albumin binding protein. Over all, GAPDH is known to exhibit moonlightling behavior, contributing to bacterial virulence in most gram positive bacteria. Like GAPDH, enolase is also reported to play a vital role in the virulence behavior of several gram positive bacteria. It is known to be present on the surface of most streptococci and has a strong plasminogen-binding property. Apart from plasminogen-binding, enolase is also found to be binding to the salivary mucin, Muc7 in *Streptococcus gordonii* contributing to the bacterial virulence. MALDI-MS imaging of these multifunctional proteins in their native form on intact biofilms should permit detailed studies of their virulence roles in biofilms.[136]

The top down approach identified only two proteins (Table II), EF1885 and EF1734, both predicted to be membrane proteins. This is not surprising since no protein digestion steps were involved in the top down approach. This is consistent with prior results in which only highly abundant membrane proteins were directly detected by MALDI-MS when no cell lysis or protein concentration steps were involved.[123, 126, 135] While EF1885 and EF1734 were detected intact without any trypsin digestion, the observed masses for their peptides were nonetheless lower than the predicted masses by 839 and 975 Da, respectively. For the protein EF 1734 a predicted cleavage site with the peptide sequence AGGFFLAR of *m/z* 837.4 was reported.[143] The observance of a lower *m/z* for the protein EF1734 is likely due to the cleavage of this peptide from the protein, although no such cleavage site has yet been reported for the protein EF1885. Fragmentation of intact proteins in the MALDI plume after desorption/ionization may have occurred here, as in-source decay is a common phenomenon in MALDI-MS.[123]

A further detailed study on imaging these identified proteins in response to various stress factors could give a greater insight and add to the future applications of imaging proteomics to the study of bacterial biofilms. For example, the method can be employed to study the effect of antimicrobial or other culturing perturbation. MALDI-MS and/or laser desorption postionization MS can be used to examine the spatial distribution of antibiotics and/or metabolites in the biofilms[35] and can colocalize them with cellular proteins, providing a more complete picture of an antimicrobial challenge and biofilm response.

3. Limits of Peptide and Protein Imaging Methodology

Only highly abundant membrane proteins or proteins that have a functional association with the cell surface could be identified and imaged, limiting the number of proteins detected by this technique.[127-129] Furthermore, in the bottom-up approach different trypsin digested peptide peaks originating from the same protein could show varying intensity within the biofilm, which could be attributed to differences in digestion efficiency, and/or desorption/ionization efficiency of different trypsin- digested peptides.[127] The lower sensitivity of the instrument to detect protein peaks of much higher masses due to poor detection efficiencies was also a major reason why more proteins were not detected by the top down approach.[127]

Optimization and/or incorporation of additional steps in cell lysis and protein denaturation that do not compromise the spatial integrity of the biofilm could aid in detection of additional proteins. The use of different enzymes or a combination of digestion enzymes might also allow identification of a larger number of proteins and their spatial localization on intact bacterial biofilms.

A major challenge with the technique is spot-to-spot variability observed within a single analysis that arises from differences in desorption/ionization efficiency rather than analyte

concentration in heterogeneous biofilms. This adverse effect can arise from ion suppression, heterogeneous matrix application, detector noise, and/or sample charging and their net effect is to hinder quantification of analytes. These factors have slowed the progress of MALDI-MS imaging for absolute quantification of analytes in many biological samples.[1, 7, 133] Various strategies have been proposed to solve the problem of quantification in MALDI-MS generally.[144] For example, stable isotope labeled internal standards have been used for protein quantification in non-imaging proteomic MS.[145, 146] Comparison with liquid chromatography MS data[147] or use of internal standards[148, 149] have also been used to quantify MALDI-MS images of lipids, drugs, and other small molecules. Further, several advanced data processing tools are in the developmental stage to address the noise and surface topography variability in MS imaging.[2]

Spatial and depth resolution are also an issue in these experiments. The ~150 μm spatial resolution is actually typical for most MALD-MS imaging of biological samples, although resolution below 25 μm is sometimes possible.[1, 7, 117] The exact depth in the biofilms from which proteins and peptides were detected was not measured, but is also likely to be in the range of tens of microns. For example, MALDI-MS imaging of animal tissue slices found that the matrix solution coated on the sample surface can extract analytes from as deep as 40 μm from the sample surface.[150]

VI. QUANTIFICATION OF ANTIBIOTIC IN BIOFILM-INHIBITING MULTILAYERS BY 7.87 EV LDPI-MS IMAGING

A. Introduction

Traditional quantification techniques based on gas or liquid chromatography mass spectrometry generally require several time consuming sample cleanup procedures prior to analysis. Over the past decade, MALDI-MS has been applied to the rapid quantification of analytes with high sample throughput and simple sample preparation.[145, 151-154] However, quantification by MALDI-MS involves several challenges with respect to reproducibility, matrix application and small molecule quantification.

This work demonstrates the potential of LDPI-MS imaging for small molecule quantification. LDPI-MS addresses some of the limitations of MALDI-MS quantification while retaining the latter's benefits of rapid sample throughput and simple sample preparation. LDPI-MS employs VUV radiation for single photon ionization of laser desorbed neutrals.[22, 35, 87] Use of VUV radiation from the fluorine laser allows single photon ionization of only those analytes with ionization energies below 7.87 eV and in the case of analyte-cluster formation,[155] up to ~8.3 eV. This selective ionization simplifies mass spectra, minimizes background signal, and improves signal to noise. Furthermore, derivatization with a low ionization energy tag or chromophore allows 7.87 eV single photon ionization of high ionization energy species.[22, 35] For example, ampicillin cannot be directly identified by 7.87 eV LDPI-MS,[156] but prior results indicate it should be detectable upon derivatization with piperazine.[157] MS imaging detects analyte over an entire sample surface, further improving quantification of spatially inhomogeneous analyte distributions. Thus, LDPI-MS imaging should be a robust tool for small molecule

quantification with potential applications in the direct analysis of bacterial biofilms on medical devices.[35, 37]

Implanted medical devices are often plagued by colonization with bacterial and/or fungal biofilms, so control of biofilm growth is essential to improve device efficacy and longevity.[158] *E. faecalis* is an opportunistic pathogen and a natural inhabitant of mammalian gastrointestinal tracts that is also a major cause of infections of the urinary tract, respiratory tract, general skin wounds, root canal and various medical implants.[130, 131] For example, *E. faecalis* biofilms are known to colonize peri-prosthesis tissues and to spread out as causative agents of orthopedic implant infections.[46] Early stage *E. faecalis* biofilm formation on medical devices generally occurs within days of implantation[159] and often results from inoculation by endogenous bacteria.

Various strategies exist to prevent early stage biofilm formation on implanted medical devices, biomaterials, and other surfaces where biofilm formation is deleterious to designed function.[160-164] This work examines the prevention of early stage biofilm formation on medical devices by use of a polyelectrolyte multilayer surface coatings composed of chitosan and alginate, both high molecular weight biopolymers.[155] The antimicrobial properties of chitosan have been well studied.[165, 166] Multilayers composed of chitosan were also found to be antimicrobial[167] and chitosan-alginate multilayers have been used for slow release of the common antibiotic ampicillin.[168] Ampicillin is derivatized here with piperazine to form the N-methylpiperazine acetamide of ampicillin. The resultant compound, called MPA-ampicillin, is detected quantitatively by 7.87 eV LDPI-MS when adsorbed in chitosan-alginate multilayers. MPA-ampicillin spiked multilayers are then shown to inhibit the growth of *E. faecalis* biofilms. Finally, LDPI-MS imaging is used to determine how much of an initial minimum inhibitory concentration of MPA-ampicillin remained in the multilayer after exposure to the biofilm.

B. Experimental Details

1. 7.87 eV LDPI-MS Imaging and MALDI-MS

7.87 eV LDPI-MS imaging was performed using a custom built instrument and the MALDI-MS was performed using a commercial instrument (4700 TOF/TOF, AB SCIEX, Foster City, CA, USA) described in detail previously in Chapter 2.

Linearity as well as limits of quantification and detection (LOQ and LOD, respectively) were determined for LDPI-MS on multilayer samples (see below). 0.3, 0.6, 1.2, 3.1, 10.2, 20.4 and 40.9 nmole aloquots of MPA-ampicillin dissolved in water:acetonitrile (7:3 v:v) were added to separate multilayers. These were allowed to dry in air for 20 min prior to the addition of 18.3 nmoles of sulfadiazine as an internal standard, then air dried again. These multilayers were then analyzed by LDPI-MS imaging for determination of MPA-ampicillin signal linearity with concentration, LOQ, and LOD. MPA-ampicillin spiked multilayers were used for efficacy studies, but the internal standard was added only immediately prior to LDPI-MS imaging. A minimum of three trials were performed for linearity, LOQ, and LOD determination.

2. Preparation of MPA-Ampicillin and Multilayers

The N-methylpiperazine acetamide of ampicillin was prepared in house using previously described methods.[157] Ten layer chitosan-alginate polyelectrolyte multilayers were prepared on 0.5 mm thick silicon substrates coated with 100 nm of gold (Sigma-Aldrich) and verified by X-ray photoelectron spectroscopy and attenuated total reflection Fourier transform infrared spectroscopy, as described previously in Chapter 2 and Chapter 3.

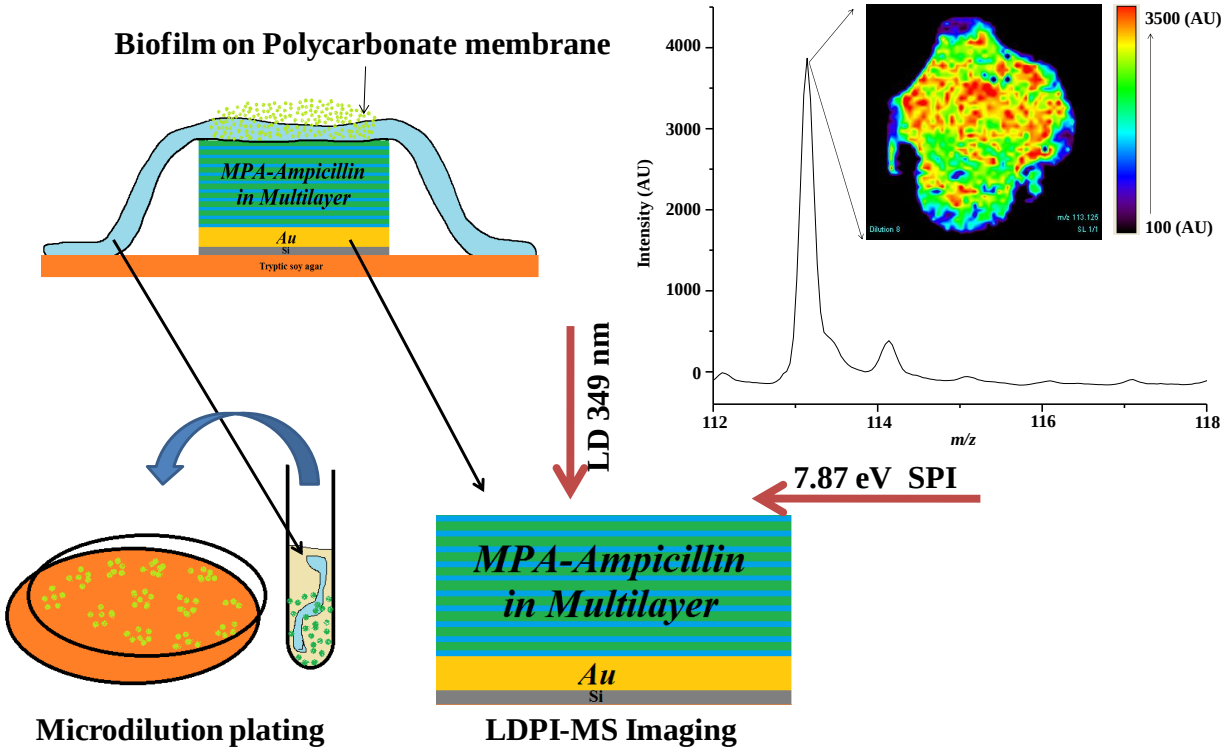

Figure 35. Schematics showing the experimental protocol for biofilm inhibition by MPA-Ampicillin.

3. *E. faecalis* Colony Biofilm Growth and MPA-Ampicillin Activity

A detailed description of colony biofilm growth is described in Chapter 2. Briefly, Polycarbonate membranes (Millipore, 0.20 µm pore size, 25 mm diameter, Fisher Scientific) were inoculated with 40 µL of 10^6 colony forming units (CFU) of *E. faecalis* V583 cultures (ATCC 700802, American Type Culture Collection, Manassus, VA), then grown on tryptic soy agar (TSA) at 37°C for three days while replenishing the agar plate daily.[87, 162] A growth curve for *E. faecalis* colony biofilms (Figure 36) indicated growth for three days was sufficient to form a mature biofilm. The MPA-ampicillin spiked multilayers were sterilized by 20 min exposure to radiation from a germicidal ultraviolet lamp (254 nm, 4.8 watts, held ~30 cm from the sample, G15T8, Osram Sylvania, Danvers, MA). Figure 35 displays a schematic of the biofilm inhibition

procedure: sterilized MPA-ampicillin spiked multilayers were placed on agar plates and mature biofilms on membranes were placed over the multilayers, completely covering them. These efficacy studies were performed in TSA media for 18 h, after which viable cells in the biofilms were counted by microdilution plating. A minimum of three trials were performed for each concentration of MPA-ampicillin.

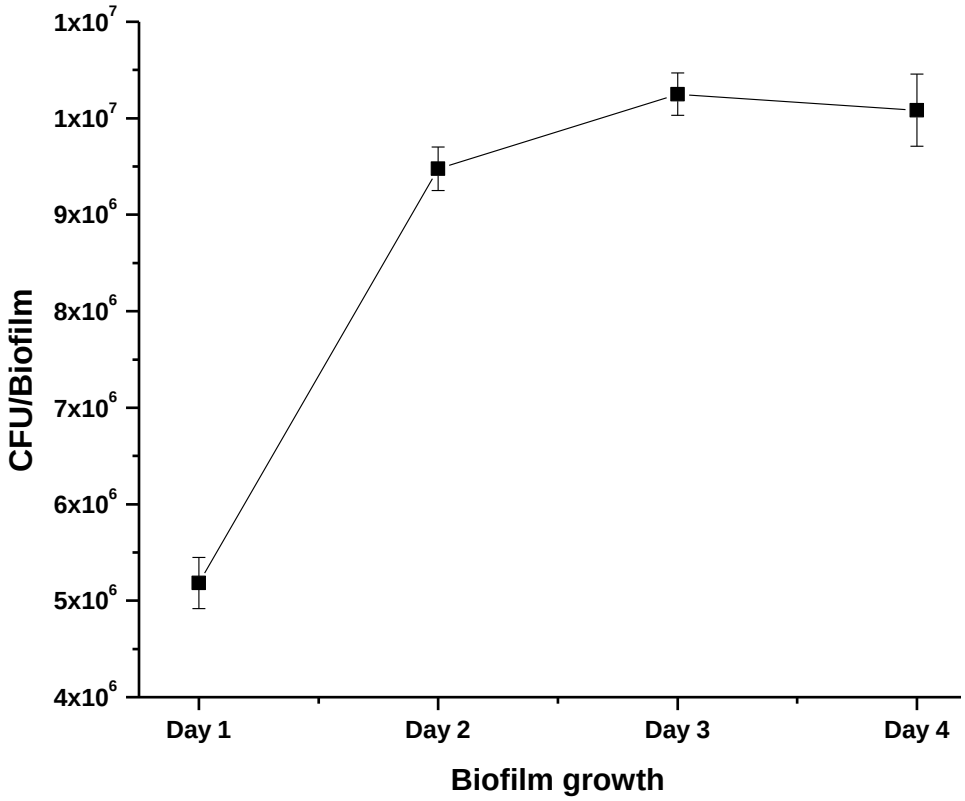

Figure 36. *E. faecalis* colony biofim growth curve.

C. Results

1. LDPI-MS of MPA-Ampicillin Neat and in Multilayers

Figure 37 displays 7.87 eV LDPI-MS of neat MPA-ampicillin, with the parent ion at *m/z* 489.2 and several predicted characteristic fragment ions (structures shown). The characteristic fragment at *m/z* 412.2 was attributed to the parent ion after loss of benzene from the ampicillin moiety. *M/z* 274.2 was attributed to the cleavage of the amide bond in the ampicillin moiety, similar to the b-type fragment ions commonly observed in peptides. *M/z* 256.2 was attributed to loss of water after amide bond cleavage, also consistent with peptide fragmentation where water or ammonia losses from y and b type ions are commonly observed. *M/z* 170.1 was attributed to the cleavage of the piperazine derivative from the ampicillin moiety and *m/z* 113.1 was attributed to piperazine. It appeared that charge resided on the piperazine moiety for all the fragments, as it does following collision induced dissociation of protonated peptides functionalized with piperazine.[146] Electronic structure calculations indicated that 7.87 eV single photon ionization is localized on the piperazine chromophore,[157] further evidence that this moiety serves as the site of position charge localization on the cation.[157]

Figure 38 shows the 7.87 eV LDPI imaging mass spectra of 3.1 nmoles of MPA-ampicillin adsorbed onto chitosan-alginate polyelectrolyte multilayers before and after UV sterilization: these spectra indicate that the antibiotic spiked into these multilayers is stable to this level of UV exposure. The antibiotic spiked multilayer displays characteristic fragments of MPA-ampicillin at *m/z* 274.2, 170.1 and 113.1. Several unlabeled peaks at *m/z* 270.1 and below *m/z* 150 appeared from desorption laser-induced pyrolysis of the multilayer.[155] The bottom and top traces show mass spectra before and after UV sterilization, respectively, again indicating no significant differences in the fragmentation pattern of MPA-ampicillin. It is concluded that photolysis or

other modification of the antibiotic or multilayer did not result from UV sterilization. MALDI-MS-MS was also performed on the UV sterilized multilayer surfaces with adsorbed antibiotic (Figure 39): no significant difference was observed in the MALDI-MS-MS of MPA-ampicillin before and after sterilization

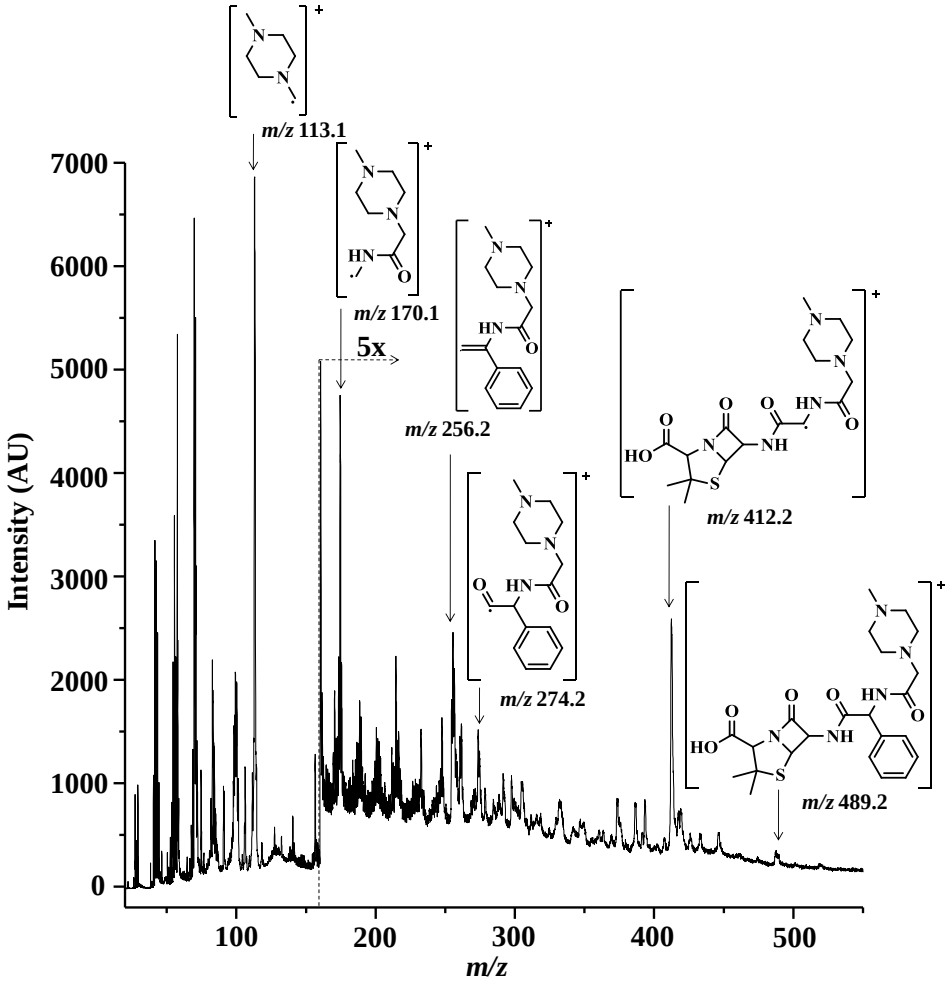

Figure 37. 7.87 eV LDPI-MS of the neat N-methylpiperazine acetamide of ampicillin (called MPA-ampicillin) shown with the structures of the parent ion and characteristic fragments.

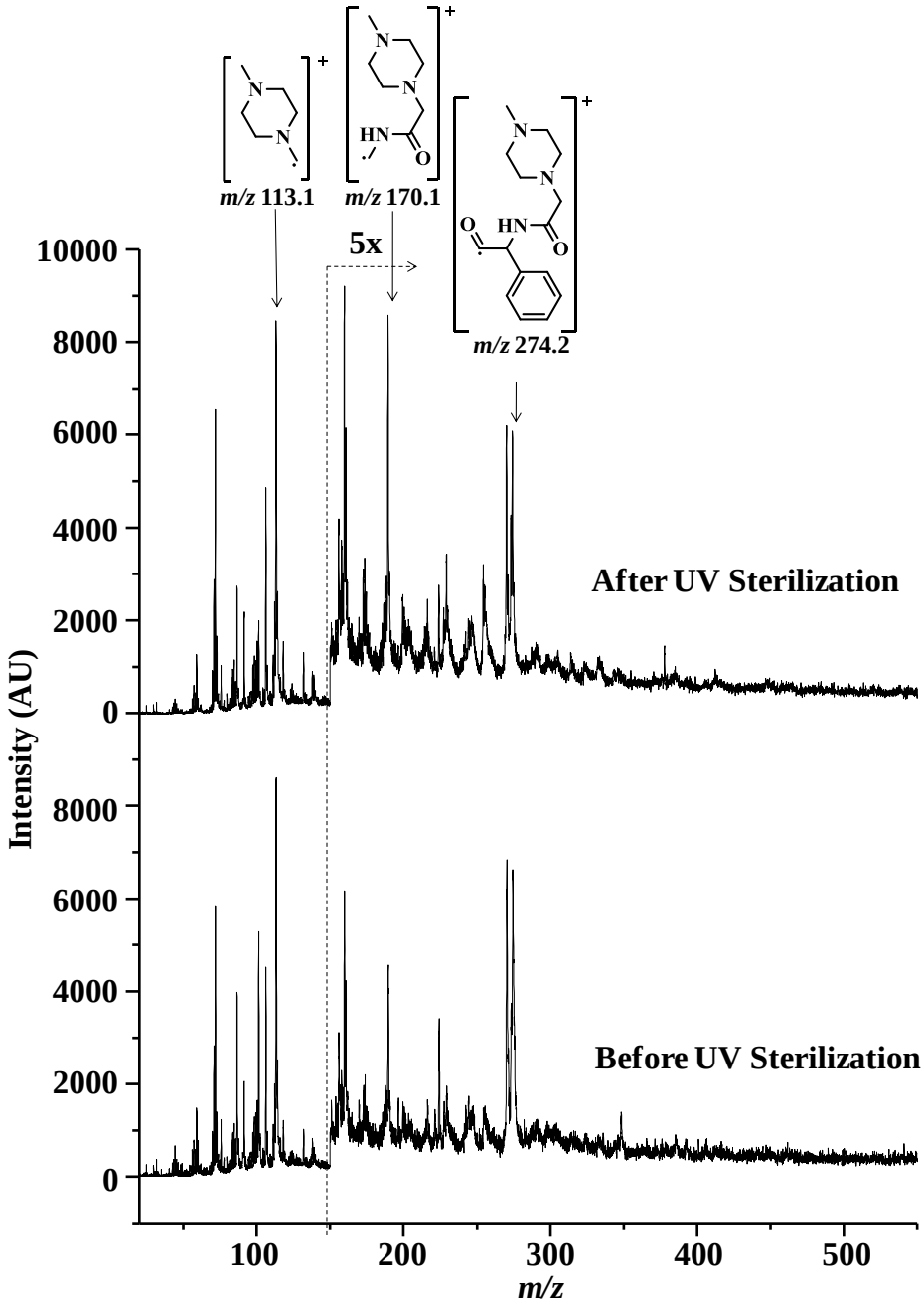

Figure 38. 7.87 eV LDPI-MS spectra of MPA-ampicillin adsorbed on multilayer surface before and after UV sterilization with peaks characteristic to MPA-ampicillin labeled.

Several fragments observed in LDPI-MS were also observed in the MALDI-MS of MPA-ampicillin in the multilayer (Figure 39). The MALDI-MS fragments at *m/z* 257.1, 158.2 and 114.1 displayed similar structures to those observed in LDPI-MS, except that the former were protonated. Furthermore, the protonated parent signal observed by MALDI-MS was more intense with respect to MPA-ampicillin fragments compared to the radical cation parent observed by LDPI-MS. However, several matrix and multilayer interference peaks were also observed at masses below *m/z* 300 in MALDI-MS that were absent in LDPI-MS. LDPI-MS analysis of MPA-ampicillin in multilayers resulted in the complete removal of not only the multilayer, but based upon visual analysis, also the ~100 nm thick gold coating from the underlying silicon substrate. This indicated that LDPI-MS sampled through the entire depth of the multilayer surface while MALDI-MS relied upon the matrix to extract the analyte from the multilayer. However, the high laser fluence employed here for Au film desorption likely imparted more internal energy into the desorbed neutrals, enhancing fragmentation upon single photon ionization and reducing the parent ion signal.[22, 35]

Parent ion signal by LDPI-MS for neat MPA-ampicillin was much lower in intensity compared to the fragment ions and for multilayer samples, no parent ion was observed. The piperazine fragment ion at *m/z* 113.1 was observed as the most intense ion from both neat and multilayer samples. Similarly, *m/z* 186.4 was observed as the most intense peak for the internal standard. Hence, the fragment peaks at *m/z* 113.1 for MPA-ampicillin and *m/z* 186.4 for the sulfadiazine internal standard were chosen for quantification of MPA-ampicillin.

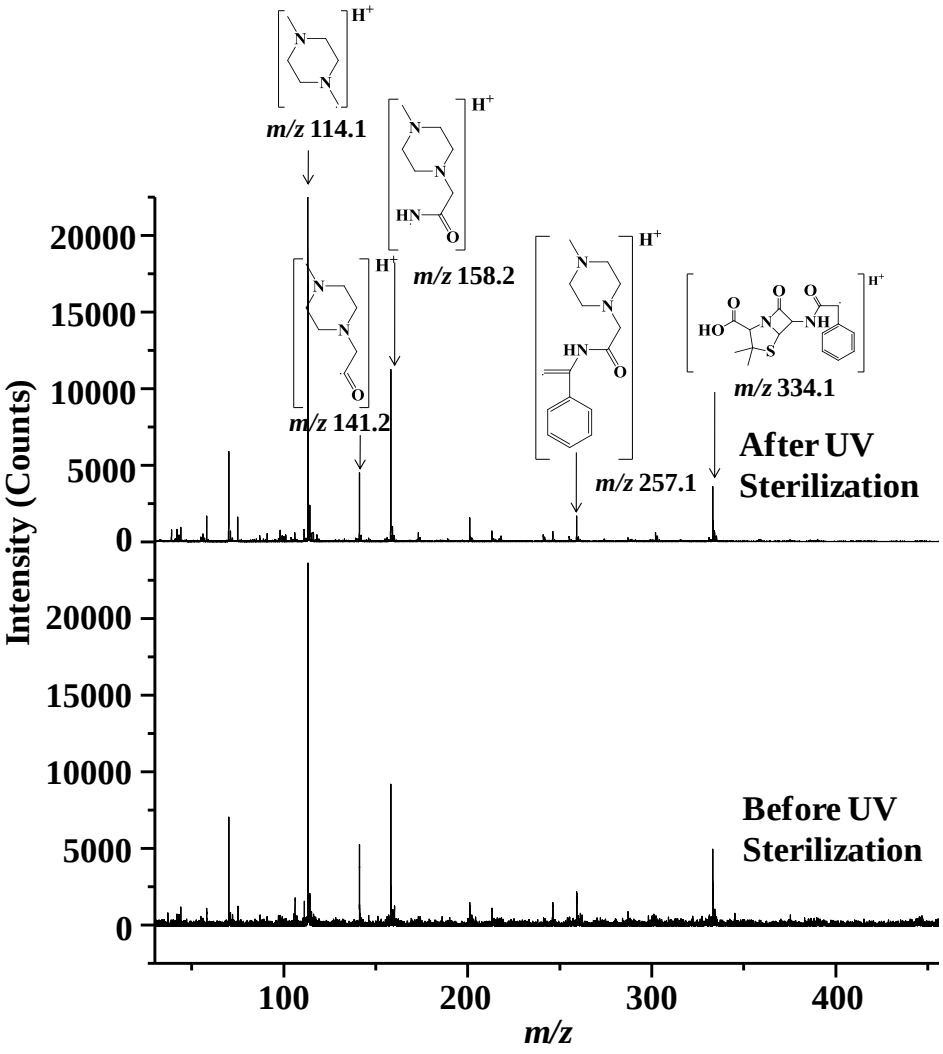

Figure 39. MALDI-MS of MPA-ampicillin adsorbed on chitosan-alginate polyelectrolye multilayers before and after UV sterilization.

2. Inhibition of Intact *E. faecalis* Colony Biofilms by MPA-Ampicillin

The antibiotic was found to inhibit *E. faecalis* biofilms growth after 18 h of incubation by the procedure shown in Figure 35. Figure 40 shows the results of this procedure, the inhibition plot against *E. faecalis* colony biofilms for multilayers spiked with 0.02 to 2.0 μmole aliquots of MPA-ampicillin. Controls consisted of no substrate applied to the biofilm (marked "Blank" in Figure 40), gold-only substrate ("Au)" and multilayer without antibiotic ("Multilayer"): all these samples were incubated with the intact biofilms grown on a 25 mm diameter polycarbonate membrane for 18 h. After incubation, the number of colony forming units (CFU) in each entire biofilm was determined by the microdilution plating method. There was no significant inhibition observed in controls when MPA-ampicillin was absent, while for the Au control there was ~2% inhibition. The PEM control displayed an ~8% inhibition, consistent with the antimicrobial properties of the chitosan component of the multilayer.[165-167]

The 90% minimum biofilm inhibitory concentration, $(MBIC)_{90}$, for MPA-ampicillin adsorbed on multilayer surfaces against these *E. faecalis* biofilms was achieved by the addition of 0.61 μmoles. 99.9 % inhibition ($2.32\pm0.07 \times 10^4$ CFU) was observed by the addition of 1.23 μmoles of MPA-ampicillin and no CFU were observed for larger amounts of antibiotic.

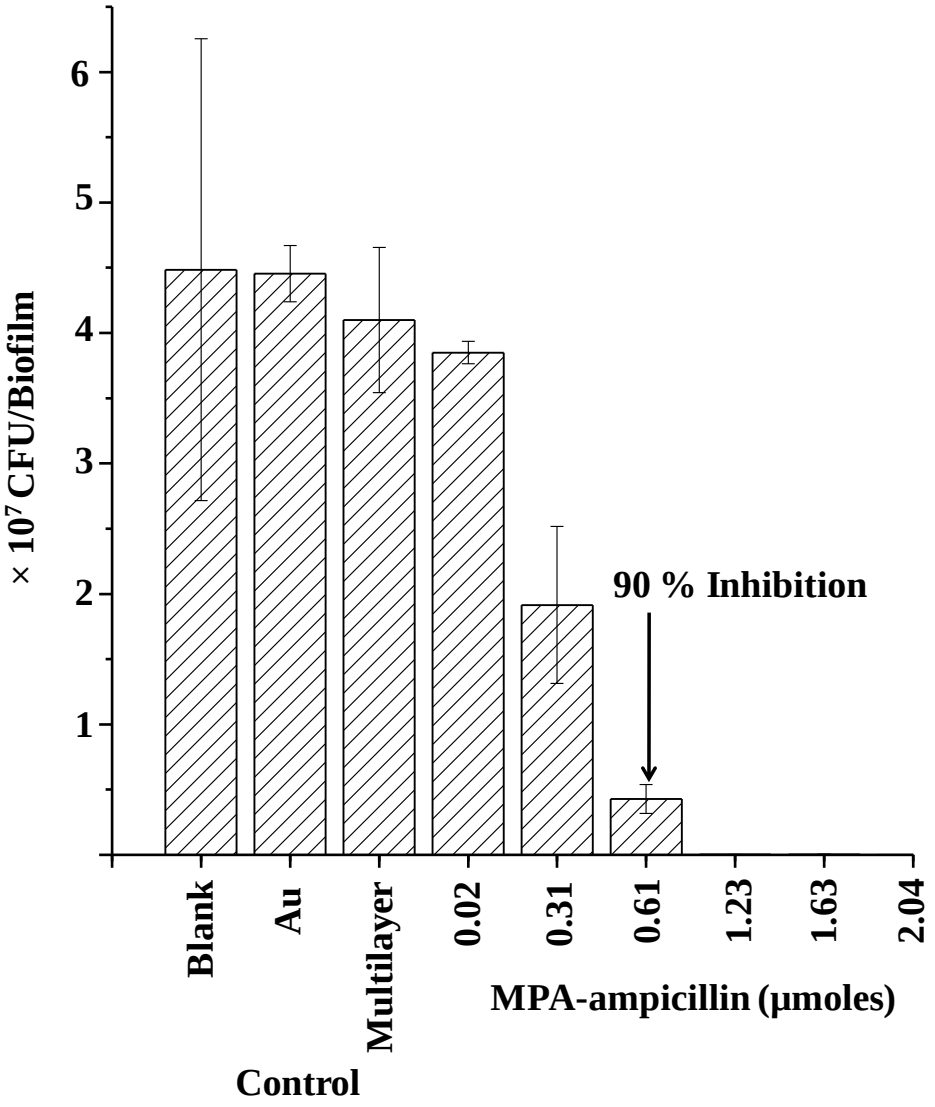

Figure 40. Inhibition plot for MPA-ampicillin adsorbed on multilayer surface against *E. faecalis* colony biofilms. or 2.32±0.07 × 10^4 CFU was observed at 1.23 µmoles MPA-ampicillin and no CFU were observed at ≥1.63 µmoles.

3. Linearity Range and Analytical Sensitivity of 7.87 eV LDPI-MS Imaging

MPA-ampicillin was spotted in amounts ranging from 0.3 to 40.9 nmoles onto multilayer surfaces along with known amounts of sulfadiazine as an internal standard (IS), then analyzed by LDPI-MS imaging. The top right corner of Figure 41 shows a representative MS image for *m/z* 113.1 (MPA-ampicillin fragment) extracted from LDPI-MS data recorded from a 1×1 cm square antibiotic spiked multilayer. The colored region in the image shows distribution of MPA-ampicillin and the black region shows its absence in the multilayer. The mass spectrum of the *m/z* 113.1 piperazine fragment was extracted by averaging over the region of interest (ROI) where the analyte was distributed in a 0.6 to 0.8 cm diameter spot on the multilayer surface (colored region in the image), both shown in Figure 41. The area of MPA-ampicillin to IS peak ratio (ration of *m/z* 113.1 to 186.4) was calculated at each concentration using the averaged mass spectra from the LDPI-MS image, then used to determine linearity. The linearity range for MPA-ampicillin spiked multilayers was established to be 0.6 to 20 nmoles with R^2 of 0.986 using data acquired from two consecutive days (Figure 42). The LOQ was 0.6 nmoles with S/N 9 and the LOD was 0.3 nmoles with S/N 6.

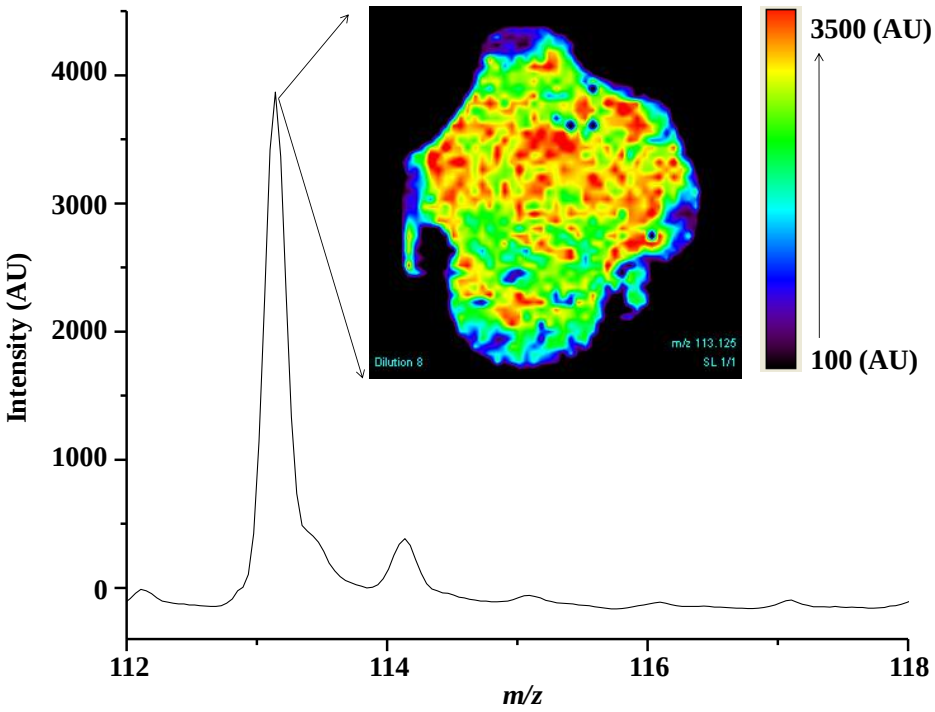

Figure 41. 7.87 eV LDPI-MS image (1 × 1 cm) showing the distribution of MPA-ampicillin (*m/z* 113.1) on the multilayer surface (inset) and the averaged mass spectrum from the region of interest (ROI).

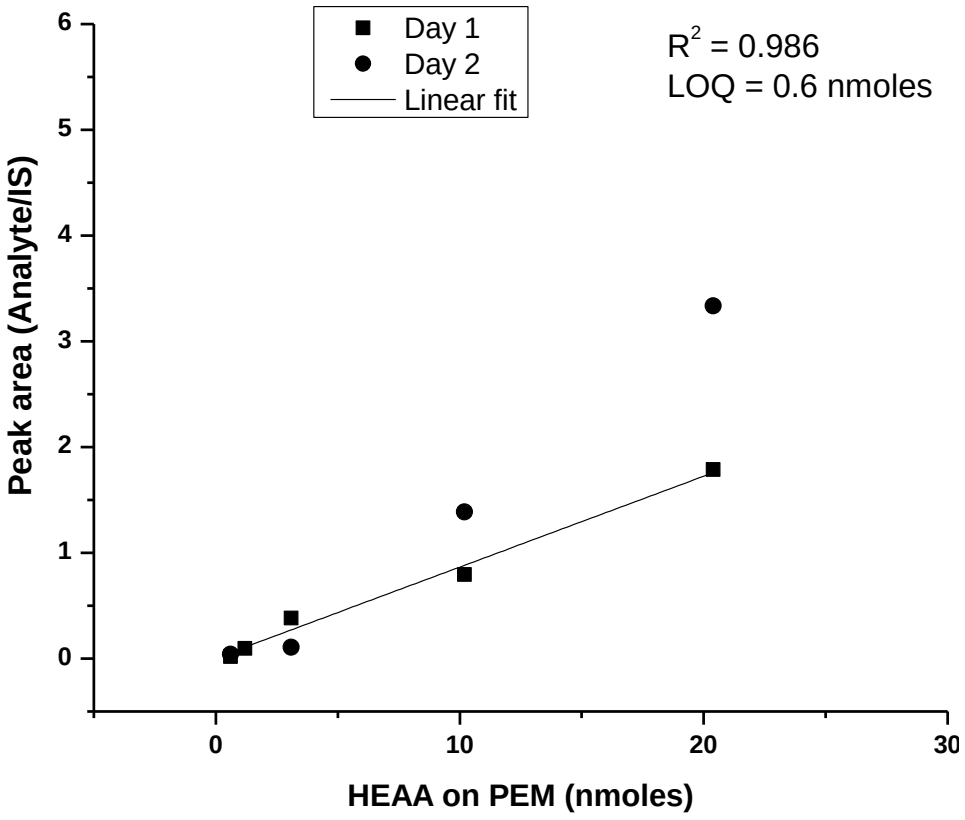

Figure 42. Linear regression plot for MPA-ampicillin adsorbed on chitosan-alginate polyelectrolye multilayers with sulfadiazine as internal standard (IS).

4. Quantification of MPA-Ampicillin in Multilayers After Biofilm Growth

A 90% biofilm-inhibiting amount of MPA-ampicillin adsorbed on multilayers was incubated with *E. faecalis* biofilms for 18h, then the multilayers were treated with IS. Analysis by LDPI-MS imaging found that only 0.7% or 3.6 nmoles (RSD of 16.0%) of the initial 0.61 µmoles of MPA-ampicillin remained on the multilayer surface after incubation with the biofilm. The area of MPA-ampicillin to internal standard peak ratio was calculated from the MS image spectra, then the linear regression established above was employed to determine the amount of MPA-ampicillin remaining on the multilayer after incubation.

D. Discussion

1. Implications for Preventing Infections on Medical Devices

Previous work found that chitosan-alginate polyelectrolyte multilayer surfaces can be used for slow release of ampicillin.[168] It is demonstrated here that 0.61 and 1.23 μmoles MPA-ampicillin inhibited 90% and 99.9% of a 25 mm diam *E. faecalis* biofilm over an 18 h exposure, respectively. If all the MPA-ampicillin instantaneously transferred to the biofilms, assumed to be 0.5 mm thick, then 90% inhibition of the biofilm occurred at ~1 mg/ml antibiotic concentration. While only 0.7% of the antibiotic remained on the multilayer after a 90% inhibiting exposure, prior results indicate that significant release of antibiotic likely continues over several hours, making the instantaneous concentration of MPA-ampicillin in the biofilm << 1 mg/ml.[168] This timescale of release should be effective given that *E. faecalis* shows high initial adhesion on several common polymeric biomaterials within 3 h of exposure.[159] The results of Figure 40, the antibiotic release timescale,[168] and the short term adhesion of microbes[159] collectively indicate that MPA-ampicillin spiked multilayers should be effective for preventing *E. faecalis* biofilm formation on medical devices and implants for the first day following implantation.

2. Quantification by LDPI-MS Imaging vs. MALDI-MS

7.87 eV LDPI-MS imaging was demonstrated to rapidly quantify a small molecule analyte on intact polyelectrolyte multilayers. Quantification by MALDI-MS of various analytes and samples without prior preparation, including protein hepcidin in human plasma,[145] melamine and its derivative in milk powder,[153] phenothiazines in human plasma,[152] and benzodiazepines.[151] Several issues must be considered when comparing quantification by LDPI-MS and MALDI-MS.

One limiting factor in quantification by MALDI-MS is the need for the addition of matrix which is known to affect sensitivity and reproducibility. Inhomogeneous co-crystallization of matrix and analyte is another additional factor to consider when using MALDI-MS for quantification, particularly when ion signal intensity is derived from single or multiple laser shots. Matrix thickness and matrix-to-analyte ratio are also known to strongly affect ion signal in MALDI-MS.[169] LDPI-MS entirely avoids the various quantification-inhibiting effects of matrix application that accompany MALDI-MS analysis of small molecules. Even homogenous application of MALDI matrix can result in matrix crystals that differ in size, quality, analyte extraction efficiency, and density per unit surface. All these factors can vary with the local physical properties of the sample surface, affecting information regarding analyte distributions.[170] By contrast, LDPI-MS uses no matrix and hence avoids these limitations.

Competing endogenous species such as proteins or lipids can cause significant ion suppression of the analyte signal as well as compound-dependent ionization efficiencies which will hinder quantification by MALDI-MS, especially in complex samples.[170] For example, certain endogenous compounds can have higher proton affinity which allows them to successfully compete for charge with the analyte. Such effects can be reduced by maintaining a constant sample composition for MALDI quantification.[144] Use of an internal standard can mitigate this effect, although homogenous introduction of an internal standard on the sample surface is required.[170] By contrast, desorption is independent of ionization in LDPI-MS, which additionally selectively ionizes only those analytes whose ionization energy is lower than 7.87 eV. In the absence of secondary proton transfer events observed at elevated pressures, most endogenous compounds will not be ionized and neither competitive ionization nor ion suppression effects should occur in LDPI-MS. Unlike atmospheric pressure photoionization,

proton transfer events are not expected here due to the low pressures in the source of the LDPI-MS.

There are several positive attributes of MALDI-MS that render it preferable for quantification, including the observation that it can approach attomole sensitivity.[145, 153, 170] By contrast, LDPI-MS is only observed here to display 0.3 nanomole sensitivity (LOD). However, this comparison is premature given that commercial MALDI-MS instruments benefited from two decades of development while the LDPI-MS instrument utilized here is a home-built, non-commercial prototype. Another positive aspect of MALDI-MS is the versatility of this ionization method: thermally labile, low mass analytes as well as involatile, high mass biopolymers including for proteins, peptides, lipids, and some pharmaceuticals can all be ionized by MALDI.[144] However, the ability for selective ionization of low ionization energy analytes by 7.87 eV LDPI-MS for some small molecule analytes provides the advantage of simplifying mass spectra, minimizing background, and improving sensitivity. Overall, 7.87 eV LDPI-MS imaging at this stage should be seen as a complimentary tool still under development for rapid quantification of small molecule analytes without the need for expensive sample clean up procedures. Furthermore, these results indicate that 7.87 eV LDPI-MS imaging should be applicable to quantification of a range of small molecular species on a variety of complex organic and biological surfaces.

VII. CONCLUSIONS

It seems that every emerging and established analytical technique has been applied to imaging. MS imaging is an emerging and fast growing imaging technique for the analysis of complex systems spatially in all three dimensions, particularly for the analysis of biological samples.

A positive contribution was made in this thesis to this emerging MS imaging field using SIMS, MALDI-MS and LDPI-MS. The protocols described can thus be used to at least partially address some unsolved scientific questions, in particular those associated with the architecture and properties of the bacterial biofilms.

Since biofilms are complex heterogeneous communities which vary widely in their composition both chemically and structurally, evaluating any new technique directly on such a complex system can result in several unresolved questions. To overcome this issue, this thesis describes the use of a multilayer model system with some resemblance to bacterial biofilms. This multilayer model system served as an excellent, well characterized system mimicking the bacterial biofilms, which was particularly essential to evaluate MS imaging protocols. C_{60}^{+} ion sputtering was used to demonstrate the possibility of depth profiling in this multilayer system, with a greater potential foreseen to perform depth profiling in real bacterial biofilms. The depth profiling described in this thesis was performed in conjunction with XPS (Chapter 3) though any other atomic or molecular imaging techniques like SIMS, MALDI or LDPI-MS can also be used in conjunction with C_{60}^{+} ion sputtering to get further valuable molecular information within the depth of the sample. Further the multilayer system does not simulate the roughness of the surface as commonly observed with real biofilms, which would be a major limiting factor in application of the technique to real biofilms. A future prospect for this depth profiling strategy

would be to evaluate the technique directly on a real biofilm system and examine its efficiency in understanding the properties of bacterial biofilms.

The multilayer surface also served as a good model system to compare the two MS techniques SIMS and LDPI-MS, to highlight the benefits of each technique particularly, to study bacterial biofilms.

In addition to performing depth profiling and evaluating the SIMS and LDPI-MS techniques using the multilayers, the multilayer system was also used as an antimicrobial surface to host a small molecule antibiotic, for slow release into a biofilm. The multilayer model also served as a good sample surface to evaluate a protocol using LDPI-MS imaging for small molecule antibiotic quantification. The results from this multilayer surface established the future prospects of utilizing this robust LDPI-MS imaging protocol to quantify small molecules directly from several other complex surfaces like tissues, biofilms and other surfaces. Furthermore, LDPI-MS imaging could serve as an alternate to the traditional quantification techniques which require analyte extraction and concentration from the sample prior to analysis.

MALDI-MS imaging was used in this thesis to demonstrate the possible use of the technique to detect, identify and spatially locate both proteins and peptides from intact bacterial biofilm surface. This can be particularly helpful in understanding the role of specific proteins in biofilms.

However, there are several limitations associated with MS imaging techniques, particularly as applied to study biological materials. Though this thesis does not address all these issues, it leaves behind several thoughtful questions to improve the technique further. For instance, a major limitation of MS imaging by MALDI-MS and LDPI-MS is their low spatial resolution, which is primarily dictated by the desorption laser. This low spatial resolution has a very

significant impact particularly in studying bacterial biofilms, although this was not an issue for the applications described in this thesis. The low spatial resolution can have a significant impact particularly in single cell studies, since the resolution of these techniques is a few hundred cells, limiting the applications of the technique when compared to other single cell non-MS based imaging techniques. Thus a major challenge to the MS imaging community is to achieve spatial resolution in the single cell level.

Another major challenge associated with MS imaging techniques is to obtain quantitative information spatially. MS imaging techniques can detect and identify molecular species from surfaces, but when it come to quantification of the detected and identified molecular species spatially there has been issues, in particular differences arise in the ionization efficiencies observed from spot to spot which are primarily due to the sample composition and the topology of the sample surface. Various strategies have been proposed to solve this problem of quantification.[144] For example, stable isotope labeled internal standards have been used for protein quantification in non-imaging proteomic MS.[145, 146] Comparison with liquid chromatography MS data[147] or use of internal standards[148, 149] have also been used to quantify MALDI-MS images of lipids, drugs, and other small molecules. Furthermore, several advanced data processing tools are in the developmental stage to address the noise and surface topography variability in MS imaging.[2] This thesis demonstrated that LDPI-MS appears particularly promising for quantification, at least for small molecule analytes. However it should be mentioned that LDPI-MS as performed here shows greater degree of fragmentation of the parent ions, this could be primarily due to laser desorption-induced energy transfer event and not due to SPI event. The LD event can be controlled to some extent, but needs further work with the method to minimize fragmentation.

It can be concluded that MS imaging is still in its infancy. Continued improvements with greater and newer applications such as those presented in this thesis are motivation to the MS imaging research to address the limitations and work towards making MS imaging a prime imaging technique. MS imaging has the potential to solve several outstanding problems that have not been addressed by other molecular imaging techniques.

CITED LITERATURE

1. Watrous, J. D.; Dorrestein, P. C., Imaging mass spectrometry in microbiology. Nature Reviews Microbiology 2011, 9, 683-94.

2. Watrous, J. D.; Alexandrov, T.; Dorrestein, P. C., The evolving field of imaging mass spectrometry and its impact on future biological research. Journal of Mass Spectrometry 2011, 46, 209-222.

3. Vickerman, J. C., Molecular imaging and depth profiling by mass spectrometry-SIMS, MALDI or DESI? Analyst 2011, 136, 2199-2217.

4. Tucker, K. R.; Lanni, E. J.; Serebryannyy, L. A.; Rubakhin, S. S.; Sweedler, J. V., Stretched Tissue Mounting for MALDI Mass Spectrometry Imaging. Analytical Chemistry 2011, 83, 9181-9185.

5. McDonnel, L. A.; Heeren, R. M. A., Imaging mass spectrometry. Mass spectrometry reviews 2007, 26, 606-643.

6. Rubakhin, S. S.; Jurchen, J. C.; Monroe, E. B.; Sweedler, J. V., Imaging mass spectrometry: fundamentals and applications to drug discovery. Drug Discovery Today 2005, 10, 823-837.

7. Chughtai, K.; Heeren, R. M. A., Mass Spectrometric Imaging for Biomedical Tissue Analysis. Chemical Reviews 2010, 110, 3237-3277.

8. Winograd, N.; Postawa, Z.; Cheng, J.; Szakal, C.; Kozole, J.; Garrison, B. J., Improvements in SIMS continue is the end in sight? Applied surface science 2006, 252, 6836-6843.

9. Walker, A. V., Why Is SIMS Underused in Chemical and Biological Analysis? Challenges and Opportunities. Analytical Chemistry 2008, 80, 8865-8870.

10. Townes, J. A.; White, A. K.; Wiggins, E. N.; Krantzman, K. D.; Garrison, B. J.; Winograd, N., Mechanism for increased yield with SF5+ projectiles in organic SIMS: The substrate effect. Journal of Physical Chemistry A 1999, 24, 4587-4589.

11. Szakal, C.; Hues, S. M.; Bennett, J.; Gillen, G., Effect of Cluster Ion Analysis Fluence on Interface Quality in SIMS Molecular Depth Profilingâ€ The Journal of Physical Chemistry C 2010, 114, 5338.

12. Smith, D. F.; Robinson, E. W.; Tolmachev, A. V.; Heeren, R. M. A.; Paša-Tolić, L., C60 Secondary Ion Fourier Transform Ion Cyclotron Resonance Mass Spectrometry. Analytical Chemistry 2011, 83, 9552-9556.

13. Seah, M. P.; Green, F. M.; Gilmore, I. S., Cluster Primary Ion Sputtering: Secondary Ion Intensities in Static SIMS of Organic Materialsâ€ The Journal of Physical Chemistry C 2009, 114, 5351.

14. Fletcher, J. S.; Lockyer, N. P.; Vickerman, J. C., Molecular SIMS imaging; spatial resolution and molecular sensitivity: have we reached the end of the road? Is there light at the end of the tunnel? Surface and interface analysis 2011, 43, 253-256.

15. Wucher, A.; Cheng, J.; Winograd, N., Protocols for three-dimensional molecular imaging using mass spectrometry. Analytical chemistry 2007, 79, 5529-5539.

16. Yamamoto, Y.; Higashi, S.; Yamamoto, K., XPS-depth analysis using C60 ion sputtering of buried interface in plasma-treated ethylene-tetrafluoroethylene-copolymer (ETFE) film. Surface and interface analysis 2008, 40, 1631-1634.

17. Yang, J.; Caprioli, R. M., Matrix Sublimation/Recrystallization for Imaging Proteins by Mass Spectrometry at High Spatial Resolution. Analytical Chemistry 2011, 83, 5728-5734.

18. Xu, B. J.; Caprioli, R. M.; Sanders, M. E.; Jensen, R. A., Direct analysis of laser capture microdissected cells by MALDI mass spectrometry. Journal of the American Society of Mass Spectrometry 2002, 13, 1292-1297.

19. Vestal, M. L., Modern MALDI time-of-flight mass spectrometry. Journal of Mass Spectrometry 2009, 44, 303-317.

20. Baluya, D. L.; Garrett, T. J.; Yost, R. A., Automated MALDI matrix deposition method with inkjet printing for imaging mass spectrometry. Analytical chemistry 2007, 79, 6862-6867.

21. Schwamborn, K.; Caprioli, R., Molecular imaging by mass spectrometry-looking beyond classical histology. Nature reviews 2010, 10, 639-646.

22. Hanley, L.; Zimmermann, R., Light and Molecular Ions: The Emergence of Vacuum UV Single-Photon Ionization in MS. Analytical Chemistry 2009, 81, 4174-4182.

23. Zhou, J.; Takahashi, L. K.; Wilson, K. R.; Leone, S. R.; Ahmed, M.; , Internal energies of ion-sputtered neutral tryptophan and thymine molecules determined by vacuum ultraviolet photoionization. Analytical chemistry 2010, 82, 3905-3913.

24. Takahashi, L. K.; Zhou, J.; Wilson, K. R.; Leone, S. R.; Ahmed, M., Imaging with mass spectrometry: A secondary ion and VUV-photoionization study of ion-sputtered atoms and clusters from GaAs and Au. Journal of physical chemistry A 2009, 113, 4035-4044.

25. L.Gasper, G.; K.Takahashi, L.; JiaZhou; Ahmed, M.; Moore, J. F.; Hanley, L., Comparing vacuum and extreme ultraviolet radiation for postionization of laser desorbed neutrals from bacterial biofilms and organic fullerenes. Nuclear instruments and methods in physics research A 2011, 649, 222-224.

26. Milasinovic, S.; Liu, Y.; Bhardwaj, C.; Blaze M.T., M.; Gordon, R. J.; Hanley, L., Feasibility of depth profiling of animal tissue by ultrashort pulse laser ablation. Analytical Chemistry 2012, 84, 3945-3951.

27. Tucker, K. R.; Serebryannyy, L. A.; Zimmerman, T. A.; Rubakhin, S. S.; Sweedler, J. V., The modified-bead stretched sample method: Development and application to MALDI-MS imaging of protein localization in the spinal cord. Chemical Science 2011, 2, 785-795.

28. Mas, S.; Perez, R.; Martinez-Pinna, R.; Egido, J.; Vivanco, F., Cluster TOF-SIMS imaging: A new light for in situ metabolomics? Proteomics 2008, 8, 3735–3745.

29. Stoeckli, M.; Staab, D.; Schweitzer, A., Compound and metabolite distribution measured by MALDI mass spectrometric imaging in whole-body tissue sections. Inertnational jouranl of mass spectrometry 2007, 260, 195-202.

30. Stauber, J.; MacAleese, L.; Franck, J.; Claude, E.; Snel, M.; Kaletas, B. K.; Wiel, I. M. V. D.; Wisztorski, M.; Fournier, I.; Heeren, R. M. A., On-tissue protein identification and imaging by MALDI-Ion mobility mass spectrometry. Journal of the American Society for Mass Spectrometry 2010, 21, 338-347.

31. Schwamborn, K.; Caprioli, R., Molecular imaging by mass spectrometry-looking beyond classical histology. Nature reviews 2010, 10, 639-646.

32. Rubakhin, S. S.; Jurchen, J. C.; Monroe, E. B.; Sweedler, J. V., Imaging mass spectrometry: fundamentals and applications to drug discovery. Drug discovery today 2005, 10, 823-837.

33. Reyzer, M. L.; Caprioli, R. M., MALDI-MS-based imaging of small molecules and proteins in tissues. Current opinion in chemical biology 2007, 11, 29-35.

34. Chughtai, K.; Heeren, R. M. A., Mass spectrometric imaging for biomedical tissue analysis. Chemical reviews 2010, 110, 3237-3277.

35. Akhmetov, A.; Moore, J. F.; Gasper, G. L.; Koin, P. J.; Hanley, L., Laser desorption postionization for imaging MS of biological material. Journal of mass spectrometry 2010, 45, 137-145.

36. Gasper, G. L.; Takahashi, L. K.; Zhou, J.; Ahmed, M.; Moore, J. F.; Hanley, L., Laser desorption postionization mass spectrometry of antibiotic-treated bacterial biofilms using tunable vacuum ultraviolet radiation. Analytical chemistry 2010, 82, 7472-7478.

37. Vertes, A.; Hitchins, V.; Phillips, K. S., Analytical Challenges of Microbial Biofilms on Medical Devices. Analytical Chemistry 2012, 84, 3858-3866.

38. Chacon, A.; Zagol-Ikapitte, I.; Amarnath, V.; Reyzer, M. L.; Oates, J. A.; Caprioli, R. M.; Boutaud, O., On-tissue chemical derivatization of 3-methoxysalicylamine for MALDI-imaging mass spectrometry. Journal of Mass Spectrometry 2011, 46, 840-846.

39. Spengler, B.; Karas, M.; Bahr, U.; Hillenkamp, F., Excimer laser desorption mass spectrometry of biomolecules at 248 and 193nm. J. Phys. Chem. 1987, 91, 6502-6506.

40. Edirisinghe, P. D.; Moore, J. F.; Calaway, W. F.; Veryovkin, I. V.; Pellin, M. J.; Hanley, L., Vacuum ultraviolet postionization of aromatic groups covalently bound to peptides. Analytical chemistry 2006, 78, 5876-5883.

41. Vertes, A.; Hitchins, V.; Phillips, K. S., Analytical challenges of microbial biofilms on medical devices. Analytical chemistry 2012, 84, 3858-3866.

42. watnick, P.; Kolter, R., Biofilm, city of microbes. Journal of bacteriology 2000, 182, 2675-2679.

43. Stoodley, P.; Sauer, K.; Davies, D. G.; Costerton, J. W., Biofilms as complex differentiated communities. Annual Review of Microbiology 2002, 56, 187-209.

44. Yip, H. K.; Guo, J.; Wong, W. H. S., Protection offered by root-surface restorative materials against biofilm challenge. Journal of Dental Research 2007, 86, 431-435.

45. Stoodley, P.; Cargo, R.; Rupp, C. J.; Wilson, S.; Klapper, I., Biofilm material properties as related to shear-induced deformation and detachment phenomena. Journal of Industrial Microbiology & Biotechnology 2002, 29, 361-367.

46. Arciola, C. R.; Baldassarri, L.; Campoccia, D.; Creti, R.; Pirini, V.; Huebner, J.; Montanaro, L., Strong biofilm production, antibiotic multi-resistance and high gelE expression in epidemic clones of Enterococcus faecalis from orthopaedic implant infections. Biomaterials 2008, 29, 580-586.

47. Heimann, P. A.; Koike, M.; Hsu, C. W.; Blank, D.; Yang, X. M.; Suits, A. G.; Lee, Y. T.; Evans, M.; Ng, C. Y.; Flaim, C.; Padmore, H. A., Performance of the vacuum ultraviolet high-resolution and high-flux beamline for chemical dynamics studies at the Advanced Light Source. Review of Scientific Instruments 1997, 68, 1945-1951.

48. Bolotin, I. L.; Tetzler, S. H.; Hanley, L., XPS and QCM studies of hydrocarbon and fluorocarbon polymer films bombarded by 1 - 20 keV C60 ions. Journal of Physical Chemistry C 2007, 111, 9953 -9960.

49. Bolotin, I. L.; Tetzler, S. H.; Hanley, L., Sputtering yield of PMMA films bombarded by keV C60+ ions Applied surface science 2006, 252, 6533-6536.

50. Wijesundara, M. B. J.; Ji, Y.; Ni, B.; Sinnott, S. B.; Hanley, L., Effect of polyatomic ion structure on thin-film growth: Experiments and molecular dynamics simulations. Journal of applied physics 2000, 88, 5004-5016.

51. Fuoco, E. R.; Gillen, G.; Wijesundara, M. B. J.; Wallace, W. E.; Hanley, L., Surface analysis studies of yield enhancements in secondary ion mass spectrometry by polyatomic projectiles. Journal of physical chemistry B 2001, 105, 3950-3956.

52. Deng, T.; Wang, H.; Li, J.-S.; Hu, S.-Q.; Shen, G.-L.; Yu, R.-Q., A novel immunosensor based on self-assemblemd chitosan/alginate multilayers for the detection of factor B. Sensors and actuators B 2004, 99, 123-129.

53. Maurstad, G.; Morch, Y. A.; Bausch, A. R.; Stokke, B. T., Polyelectrolyte layer interpretation and swelling of alginate-chitosan multilayers studied by dual wavelength reflection interference contrast microscopy. Carbohydrate polymers 2008, 71, 672-681.

54. Sahni, N.; Yi, S.; Daniels, K. J.; Srikantha, T.; Pujol, C.; Soll, D. R., Gene selectively up-regulated by pheromone in white cells are involved in biofilm formation in candida albicans. PLoS pathogens 2009, 5, 1-18.

55. Jiao, Y.; Haeseleer, P. D.; Dill, B. D.; Shah, M.; VerBerkmoes, N. C.; Hettich, R. L.; Banfield, J. F.; Thelen, M. P., Identification of biofilm matrix-associated proteins from an acid mine drainage microbial community. Applied and environmental microbiology 2011, 77, 5230-5237.

56. Arciola, C. R.; Baldassarric, L.; Campocciaa, D.; Cretic, R.; Pirinia, V.; Huebnerd, J.; Montanaroa, L., Strong biofilm production, antibiotic multi-resistance and high gelE expression in epidemic clones of Enterococcus faecalis from orthopaedic implant infections. Biomaterials 2008, 29, 580-586.

57. Swenson, J. M.; Clark, N. C.; Sahm, D. F.; Ferraro, M. J.; Doern, G.; Hindler, J.; Jorgensen, J. H.; Pfaller, M. A.; Reller, L. B.; Weinstein, M. P.; Zabransky, R. J.; Tenover, F. C., Molecular characterization and multilaboratory evaluation of Enterococcus faecalis ATCC 51299 for quality control of screening tests for vancomycin and high-level aminoglycoside resistance in Enterococci. Journal of clinical microbiology 1995, 33, 3019-3021.

58. Sahm, D. F.; Kissinger, J.; Gilmore, M. S.; Murray, P. R.; Mulder, R.; Solliday, J.; Clarke, B., In vitro susceptibility studies of vancomycin-resistant enterococcus faecalis. Antimicrobial Agents and Chemotherapy 1989, 33, 1588-1591.

59. Lavigne, J. P.; Helene, M.; Chanoine, N.; Bourg, G.; Moreau, J.; Sotto, A., Virulent synergistic effect between enterococcus faecalis and escherichia coli assayed by using the caenorhabditis elegans model. PLoS One 2008, 3, e3370.

60. Kayaoglu, G.; Orstavik, D., Virulance factors of enterococcus faecalis: relationship to endodontic disease Critical Reviews in Oral Biology & Medicine 2004, 15, 308-320.

61. Jones, E. A.; Lockyer, N. P.; Vickerman, J. C., Depth Profiling Brain Tissue Sections with a 40 keV C60+ Primary Ion Beam. Anal. Chem. 2008, 80, 2125-2132.

62. Sostarecz, A. G.; Sun, S.; Szakal, C.; Wucher, A.; Winograd, N., Applied Surface Science 2004, 231/232, 179.

63. Kozole, J.; Szakal, C.; Kurczy, M.; Winograd, N., Model multilayer structure for three-dimentional cell imaging. Applied Surface Science 2006, 252, 6789-6792.

64. Briggs, D., Surface Analysis of Polymers by XPS and Static SIMS. Cambridge University Press: New York, 1998; p 198.

65. Morgan, S. M.; Al-Shamkhani, A.; Callant, D.; Schacht, E.; Woodley, J. F.; Duncan, R., Alginates as drug carriers: covalent attachment of alginates to therapeutic agents containing primary amine groups. Internaltional journal of pharmaceutics 1995, 122, 121-128.

66. Rowley, J. A.; Madlambayan, G.; Mooney, D. J., Alginate hydrogels as synthetic extracellular matrix materials. Biomaterials 1999, 20, 45-53.

67. Gomez, C. G.; Chambat, G.; Heyraud, A.; Villar, M.; Auzely-Velty, R., Synthesis and characterization of a B-CD-alginate conjugate. Polymer 2006, 47, 8509-8516

68. Yalpani, M.; Hall, L. D., Some chemical and analytical aspects of polysaccharide modifications. I. Nitoxide spin-labelling studies of algenic acid, cellulose, and xanthan gum. Canadian journal of chemistry 1981, 59, 3105-3115.

69. Grasdalen, H.; Larsen, B.; Smidsrod, O., 13C NMR studies of monomeric composition and sequence in alginate. carbohydrate research 1981, 89, 179-191.

70. Ikeda, A.; Takemura, A.; Ono, H., Preparation of low molecular weight alginic acid by acid hydrolysis. Carbohydrate polymers 2000, 42, 421-425.

71. Boyd, J.; Turvey, J. R., Identification by 13C-NMR spectroscopy of oligosaccharides derived from alginic acid. carbohydrate research 1978, 61, 223-226.

72. Lawrie, G.; Keen, I.; Drew, B.; Chandler-Temple, A.; Rintoul, L.; Fredericks, P.; Grondahl, L., Interaction between alginate and chitosan biopolymers characterized by FTIR and XPS. Biomacromolecules 2007, 8, 2533-2541.

73. Sakkayawong, N.; Thiravetyan, P.; Nakbanpote, W., Adsorption mechanism of sythetic reactive dye wastewater by chitosan. JOurnal of colloid adn interface science 2005, 286, 36-42.

74. Kim, M.-S.; Choi, Y.-J.; Park, H. S.; Noh, I., Analysis of chitosan irradiated with high-energy cyclotron ion beams. Journal of physics and chemistry of solids 2008, 69, 1569-1572.

75. Osugi, N.; DOng, T.; Hexig, B.; Inoue, Y., Generation and characterization of compositional gradient structure in the biodegradable chitosan/poly(ethylene oxide) Blend. Journal of applied polymer science 2007, 104, 2939-2946.

76. Stevens, J. S.; Schroeder, S. L. M., Quantitative analysis of saccharides by X-ray photoelectron spectroscopy. Surface and Interface Analysis 2009, 41, 453-462.

77. Nobuta, T.; Ogawa, T., Depth profile XPS analysis of polymeric materials by C60+ ion sputtering. Journal of material science 2009, 77, 1800-1812.

78. Sanada, N.; Yamamoto, A.; Oiwa, R.; Ohashi, Y., Extremely low sputtering degradation of polytetrafluoroethylene by C60 ion beam applied in XPS analysis. Surface and Interfacial Analysis 2004, 36, 280-282.

79. Maurstad, G.; Morch, Y. A.; Bausch, A. R.; Stokke, B. T., Polyelectrolyte layer interpenetration and swelling of alginate-chitosan multilayer studied by dual wavelength reflection interference contrast microscopy. Carbohydrate Polymers 2008, 71, 672-681.

80. Alves, N. M.; Picart, C.; Mano, J. F., Self Assembling and Crosslinking of Polyelectrolyte Multilayer Films of Chitosan and Alginate Studied by QCM and IR Spectroscopy. Macromolecular Bioscience 2009, 9, 776-785.

81. Otto, M., Staphylococcus epidermidis – the 'accidental' pathogen. Nature Reviews Microbiology 2009, 7, 555-567.

82. Tyler, B. J.; Rangaranjan, S.; Möller, J.; Beumer, A.; Arlinghaus, H. F., TOF-SIMS imaging of chlorhexidine-digluconate transport in frozen hydrated biofilms of the fungus Candida albicans. Applied Surface Science 2006, 252, 6712-6715.

83. Vaidyanathan, S.; Fletcher, J. S.; Jarvis, R. M.; Henderson, A.; Lockyer, N. P.; Goodacre, R.; Vickerman, J. C., Explanatory multivariate analysis of ToF-SIMS spectra for the discrimination of bacterial isolates. Analyst 2009, 134, 2352.

84. Esquenazi, E.; Yang, Y. L.; Watrous, J.; Gerwick, W. H.; Dorrestein, P. C., Imaging mass spectrometry of natural products. Nat Prod Rep 2009, 26, 1521-34.

85. Takahashi, L. K.; Zhou, J.; Wilson, K. R.; Leone, S. R.; Ahmed, M., Imaging with Mass Spectrometry: A Secondary Ion and VUV-Photoionization Study of Ion-Sputtered Atoms and Clusters from GaAs and Au. The Journal of Physical Chemistry A 2009, 113, 4035-4044.

86. Li, Y.; Qi, F., Recent Applications of Synchrotron VUV Photoionization Mass Spectrometry: Insight into Combustion Chemistry. Accounts of Chemical Research 2009, 43, 68.

87. Gasper, G. L.; Takahashi, L. K.; Zhou, J.; Ahmed, M.; Moore, J. F.; Hanley, L., Laser Desorption Postionization Mass Spectrometry of Antibiotic-Treated Bacterial Biofilms using Tunable Vacuum Ultraviolet Radiation Analytical Chemistry 2010, 82, 7472-7478.

88. Frisch, M. J.; Trucks, G. W.; Schlegel, H. B.; Scuseria, G. E.; Robb, M. A.; Cheeseman, J. R.; Montgomery, J. A. J.; Vreven, T.; Kudin, K. N.; Burant, J. C.; Millam, J. M.; Iyengar, S. S.; Tomasi, J.; Barone, V.; Mennucci, B.; Cossi, M.; Scalmani, G.; Rega, N.; Petersson, G. A.; Nakatsuji, H.; Hada, M.; Ehara, M.; Toyota, K.; Fukuda, R.; Hasegawa, J.; Ishida, M.; Nakajima, T.; Honda, Y.; Kitao, O.; Nakai, H.; Klene, M.; Li, X.; Knox, J. E.; Hratchian, H. P.; Cross, J. B.; Adamo, C.; Jaramillo, J.; Gomperts, R.; Stratmann, R. E.; Yazyev, O.; Austin, A. J.; Cammi, R.; Pomelli, C.; Ochterski, J. W.; Ayala, P. Y.; Morokuma, K.; Voth, G. A.; Salvador, P.; Dannenberg, J. J.; Zakrzewski, V. G.; Dapprich, S.; Daniels, A. D.; Strain, M. C.; Farkas, O.; Malick, D. K.; Rabuck, A. D.; Raghavachari, K.; Foresman, J. B.; Ortiz, J. V.; Cui, Q.; Baboul, A. G.; Clifford, S.; Cioslowski, J.; Stefanov, B. B.; Liu, G.; Liashenko, A.; Piskorz, P.; Komaromi, I.; Martin, R. L.; Fox, D. J.; T.; Keith; Al-Laham, M. A.; Peng, C. Y.; Nanayakkara, A.; Challacombe, M.; Gill, P. M. W.; Johnson, B.; Chen, W.; Wong, M. W.; Gonzalez, C.; Pople, J. A. Gaussian 03, Revision A.1; Gaussian, Inc.: Pittsburgh, 2003.

89. Lu, J.; Zhu, S.; Zhou, Z.; Wu, Q.; Zhao, G., DFT calculations of the ionization potentials and electron affinities of serinamide. International journal of quantum chemistry 2006, 106, 2073-2081

90. Hu, Y.; Lu, R.; Cai, Y.; Wang, X., Multiphoton ionization and ab initio calculation of teh hydrogen-bonded clusters (C5H5N)n(NH3)m. Journal of mass spectrometry 2001, 36, 329-335.

91. Okai, N.; Takahata, A.; Fuke, K., Electronic structure, stability, and formation dynamics of hypervalent molecular cluster: CH3NH3(CH3NH2)n. Chemical physics letters 2004, 386, 442-447.

92. Rohlfing, A.; Leisner, A.; Hillenkamp, F.; Dreisewerd, K., Investigation of the Desorption Process in UV Matrix-Assisted Laser Desorption/Ionization with a Liquid 3-Nitrobenzyl Alcohol Matrix by Photoacoustic Analysis, Fast-Flash Imaging, and UV-Laser Postionizationâ€ The Journal of Physical Chemistry C 2009, 114, 5367.

93. Knochenmuss, R.; Zhigilei, L. V., Molecular dynamics simulations of MALDI: laser fluence and pulse width dependence of plume characteristics and consequences for matrix and analyte ionization. Journal of Mass Spectrometry 2010, 45, 333-346.

94. Jochims, H.-W.; Schwell, M.; Chotin, J.-L.; Clemino, M.; Dulieu, F.; Baumgärtel, H.; Leach, S., Photoion mass spectrometry of five amino acids in the 6–22 eV photon energy range. Chemical Physics 2004, 298, 279-297.

95. Schwell, M.; Jochims, H.-W.; Baumgärtel, H.; Dulieu, F.; Leach, S., VUV photochemistry of small biomolecules. Planetary and Space Science 2006, 54, 1073.

96. Edirisinghe, P. D.; Moore, J. F.; Calaway, W. F.; Veryovkin, I. V.; Pellin, M. J.; Hanley, L., Vacuum ultraviolet postionization of aromatic groups covalently bound to peptides. Analytical Chemistry 2006, 78, 5876-5883.

97. Zhang, L.; Pan, Y.; Guo, H.; Zhang, T.; Sheng, L.; Qi, F.; Lo, P.-K.; Lau, K.-C., Conformation-Specific Pathways of Î²-Alanine: A Vacuum Ultraviolet Photoionization and Theoretical Study. The Journal of Physical Chemistry A 2009, 113, 5838.

98. Kinsel, G. R.; Knochenmuss, R.; Setz, P.; Land, C. M.; Goh, S.-K.; Archibong, E. F.; Hardesty, J. H.; Marynick, D. S., Ionization energy reductions in small 2,5-dihydroxybenzoic acid-proline clusters. Journal of Mass Spectrometry 2002, 37, 1131-1140.

99. Kostko, O.; Bravaya, K.; Krylov, A.; Ahmed, M., Ionization of cytosine monomer and dimer studied by VUV photoionization and electronic structure calculations. Physical Chemistry and Chemical Physics 2010, 12, 2860.

100. Belau, L.; Wilson, K. R.; Leone, S. R.; Ahmed, M., Vacuum ultraviolet (VUV) photoionization of small water clusters. Journal of Physical Chemistry A 2007, 111, 10075-10083.

101. Barth, S.; OncÌŒaÌ□k, M.; Ulrich, V.; Mucke, M.; Lischke, T.; SlaviÌ□cÌŒek, P.; Hergenhahn, U., Valence Ionization of Water Clusters: From Isolated Molecules to Bulk. The Journal of Physical Chemistry A 2009, 113, 13519.

102. Belau, L.; Wilson, K. R.; Leone, S. R.; Ahmed, M., Vacuum-Ultraviolet Photoionization Studies of the Microhydration of DNA Bases (Guanine, Cytosine, Adenine, and Thymine). J. Phys. Chem. A 2007, 111, 7562-7568.

103. Heinbuch, S.; Dong, F.; Rocca, J. J.; Bernstein, E. R., Single photon ionization of hydrogen bonded clusters with a soft x-ray laser: (HCOOH)[sub x] and (HCOOH)[sub y](H[sub 2]O)[sub z]. The Journal of Chemical Physics 2007, 126, 244301.

104. Gamez, G.; Zhu, L.; Schmitz, T. A.; Zenobi, R., Photoelectron Emission as an Alternative Electron Impact Ionization Source for Ion Trap Mass Spectrometry. Anal. Chem. 2008, 80, 6791-6795.

105. Suits, A. G.; Heimann, P.; Yang, X.; Evans, M.; Hsu, C.-W.; Lu, K.-t.; Lee, Y. T.; Kung, A. H., Review of Scientific Instruments 1995, 66, 4841.

106. Scaiano, J. C.; Barra, M.; Sinta, R., Chain amplified photoacid generation from vicinal dibromides. A general strategy for the efficient generation of hydrogen bromide across the ultraviolet and visible spectrum. Chemistry of Materials 1996, 8, 161-166.

107. Huang, J.; Xu, D.; Francisco, J. S.; Jackson, W. M., Photodissociation of bromoform cation at 308, 355, and 610 nm by means of time-of-flight mass spectroscopy and ion velocity imaging. Journal of Chemical Physics 2003, 118, 3083.

108. Tam, S. K.; Dusseault, J.; Polizu, S.; Menard, M.; Halle, J.-P.; Yahia, L. H., Physicochemical model of alginate−poly-L-lysine microcapsules defined at the micrometric/nanometric scale using ATR-FTIR, XPS and TOF-SIMS. Biomaterials 2005, 26, 6950-6961.

109. Sjovall, P.; Lausmaa, J.; Johansson, B.-L.; Andersson, M., Surface Chemical Analysis of Charbohydrate Materials Used for Chromatography Media by Time-of-Flight Secondary Ion Mass Spectrometry. Analytical Chemistry 2004, 76, 1857-1864.

110. Marchi, I.; Rudaz, S.; Veuthey, J., Atmospheric pressure photoionization for coupling liquid-chromatography to mass spectrometry: A review. Talanta 2009, 78, 1–18.

111. Harrison, A. G., Chemical ionization mass spectrometry. CRC Press: Boca Raton, 1992.

112. Drake, R. R.; Boggs, S. R.; Drake, S. K., Pathogen identification using mass spectrometry in the clinical microbiology laboratory. Journal of Mass Spectrometry 2011, 46, 1223-1232.

113. Jiao, Y.; D'haeseleer, P.; Dill, B. D.; Shah, M.; VerBerkmoes, N. C.; Hettich, R. L.; Banfield, J. F.; Thelen, M. P., Identification of biofilm matrix-associated proteins from an acid mine drainage microbial community. Applied and Environmental Microbiology 2011, 77, 5230-5237.

114. Demirev, P. A.; Ho, Y.-P.; Ryzhov, V.; Fenselau, C., Microorganism identification by mass spectrometry and protein database search. Analytical Chemistry 1999, 71, 2732-2738.

115. Wilkins, C. L.; Lay, J. O., Identification of Microorganisms by Mass Spectrometry. Wiley: New York, 2006; Vol. 169.

116. Williamson, Y. M.; Moura, H.; Woolfitt, A. R.; Pirkle, J. L.; Barr, J. R.; Da Gloria Carvalho, M.; Ades, E. P.; Carlone, G. M.; Sampson, J. S., Differentiation of Steptococcus preumoniae conjunctivitis outbreak isolates by matrix-assisted laser desorption ionization-time of flight mass spectrometry. Applied and Environmental Microbiology 2008, 74, 5891-5897.

117. Seeley, E. H.; Caprioli, R. M., Molecular imaging of proteins in tissues by mass spectrometry. Proceedings of the National Academy of Sciences, U.S.A. 2008, 105, 18126-18131.

118. Esquenazi, E.; Coates, C.; Simmons, L.; Gonzalez, D.; Gerwick, W. H.; Dorrestein, P. C., Visualizing the spatial distribution of secondary metabolites produced by marine cyanobacteria and sponges via MALDI-TOF imaging. Mol Biosyst 2008, 4, 562-70.

119. Gonzalez, D. J.; Haste, N. M.; Hollands, A.; Fleming, T. C.; Hamby, M.; Pogliano, K.; Nizet, V.; Dorrestein, P. C., Microbial competition between Bacillus subtilis and Staphylococcus aureus monitored by imaging mass spectrometry. Microbiology 2011, 157, 2485-92.

120. Liu, W. T.; Yang, Y. L.; Xu, Y.; Lamsa, A.; Haste, N. M.; Yang, J. Y.; Ng, J.; Gonzalez, D.; Ellermeier, C. D.; Straight, P. D.; Pevzner, P. A.; Pogliano, J.; Nizet, V.; Pogliano, K.; Dorrestein, P. C., Imaging mass spectrometry of intraspecies metabolic exchange revealed the cannibalistic factors of Bacillus subtilis. Proc Natl Acad Sci U S A 2010, 107, 16286-90.

121. Gasper, G. L.; Carlson, R.; Akhmetov, A.; Moore, J. F.; Hanley, L., Laser desorption 7.87 eV postionization mass spectrometry of antibiotics in Staphylococcus epidermidis bacterial biofilms. Proteomics 2008, 8, 3816-3821.

122. Anantharaman, V.; Iyer, L. M.; Aravind, L., Comparative Genomics of Protists: New Insights into the Evolution of Eukaryotic Signal Transduction and Gene Regulation. Annual Review of Microbiology 2007, 61, 453-475.

123. Calligaris, D.; Villard, C.; Lafitte, D., Advances in top-down proteomics for disease biomarker discovery. Journal of Proteomics 2011, 74, 920-934.

124. P.Mallick; Kuster, B., Proteomics: a pragmatic perspective. Nature Biotechnology 2010, 28, 695-709.

125. Speers, A. E.; Wu, C. C., Proteomics of Integral Membrane Proteins - Theory and Application. Chemical Reviews 2007, 107, 3687-3714.

126. Dani, F. R.; Francese, S.; Mastrobuoni, G.; Felicioli, A.; Caputo, B.; Simard, F.; Pieraccini, G.; Moneti, G.; Coluzzi, M.; della Torre, A.; Turillazzi, S., Exploring Proteins in Anopheles gambiae Male and Female Antennae through MALDI Mass Spectrometry Profiling. PLoS ONE 2008, 3, e2822.

127. Groseclose, M. R.; Andersson, M.; Hardesty, W. M.; Caprioli, R. M., Identification of proteins directly from tissue: in situ tryptic digests couple with imaging mass spectrometry. Journal of Mass Spectrometry 2007, 42, 254-262.

128. Lemaire, R.; Desmons, A.; Tabet, J. C.; Day, R.; Salzet, M.; Fournier, I., Direct analysis and MALDI imaging of formalin-fixed paraffin-embedded tissue sections. Journal of Proteome Research 2007, 6, 1295-1305.

129. Stauber, J.; MacAleese, L.; Franck, J.; Claude, E.; Snel, M.; Kaletas, B. K.; Wiel, I. M. V. D.; Wisztorski, M.; Fournier, I.; Heeren, R. M. A., On-Tissue Protein Identification and Imaging by MALDI-Ion Mobility Mass Spectrometry. Journal of the American Society for Mass Spectrometry 2010, 21, 338-347.

130. Klare, I.; Werner, G.; W., W., Enterococci. Habitats, infections, virulence factors, resistances to antibiotics, transfer of resistance determinants. Contributions in Microbiology 2001, 8, 108-122.

131. Tailor, S. A.; Bailey, E. M.; Rybak, M. J., Enterococcus an emerging pathogen. Annals of Pharmacotherapy 1993, 27, 1231-1242.

132. Sahm, D. F.; Kissinger, J.; Gilmore, M. S.; Murray, P. R.; Mulder, R.; Solliday, J.; Clarke, B., In vitro susceptibility studies of vancomycin-resistant enterococcus faecalis. Antimicrobial Agents and Chemotherapy 1989, 33, 1588-1591.

133. Wang, X.; He, X.; Jiang, Z.; Wang, J.; Chen, X.; Liu, D.; Wang, F.; Guo, Y.; Zhao, J.; Liu, F.; Huang, L.; Yuan, J., Proteomic analysis of the enterococcus faecalis V583 strain and clinical isolate V309 under vancomycin treatment. Journal of Proteome Research 2010, 9, 1772-1785.

134. Paulsen, I. T.; Banerjei, L.; Myers, G. S. A.; Nelson, K. E.; Seshadri, R.; Read, T. D.; Fouts, D. E.; Eisen, J. A.; Gill, S. R.; Heidelberg, J. F.; Tettelin, H.; Dodson, R. J.; Umayam, L.; Brinkac, L.; Beanan, M.; Daugherty, S.; DeBoy, R. T.; Durkin, S.; Kolonay, J.; Madupu, R.; Nelson, W.; Vamathevan, J.; Tran, B.; Upton, J.; Hansen, T.; Shetty, J.; Khouri, H.; Utterback, T.; Radune, D.; Ketchum, K. A.; Dougherty, B. A.; Fraser, C. M., Role of mobile DNA in the evolution of vancomycin-resistant enterococcus faecalis. Science 2003, 299, 2071-2074.

135. Benachour, A.; Morin, T.; Bert, L. H.; Verneuil, A. L. B.; Jeune, A. L.; Auffray, Y.; Pichereau, V., Identification of secreted and surface proteins from enterococcus faecalis. Canadian Journal of Microbiology 2009, 55, 967-974.

136. Coburn, P. S.; Pillar, C. M.; Jett, B. D.; Haas, W.; Gilmore, M. S., Enterococcus faecalis senses target cells and in response expresses cytolysin. Science 2004, 306, 2270-2272.

137. Lavigne, J.-P.; Nicolas-Chanoine, M.-H.; Bourg, G.; Moreau, J.; Sotto, A., Virulent Synergistic Effect between Enterococcus faecalis and Escherichia coli Assayed by Using the Caenorhabditis elegans model PLoS ONE 2008, 3, e3370.

138. Roepstorff, P.; Fohlman, J., Proposal for a common nomenclature for sequence ions in mass spectra of peptides. Biomedical Mass Spectrometry 1984, 11, 601.

139. Ong, L.; Shah, N. P., Release and identification of angiotensin-converting enzyme-inhibitory peptides as influenced by ripening temperatures and probiotic adjuncts in Cheddar cheeses. Food Science and Technology 2008, 41, 1555-1566.

140. Sarantinopoulos, P.; Andrighetto, C.; Georgalaki, M. D.; Rea, M. C.; Lombardi, A.; Cogan, T. M.; Kalantzopoulos, G.; Tsakalidou, E., Biochemical properties of enterococci relevant to their technological performance. International Dairy Journal 2001, 11, 621-647.

141. Pancholi, V.; Fischetti, V. A., a-Enolase, a Novel Strong Plasmin(ogen) Binding Protein on the Surface of Pathogenic Streptococci. Journal of Biological Chemistry 1998, 273, 14503-14515.

142. Pancholi, V.; Fischetti, V. A., A Major Surface Protein on Group A Streptococci is a Glyceraldehyde-3-Phosphate-Dehydrogenase with Multiple Binding Activity. Journal of Experimental Medicine 1992, 176, 415-426.

143. Wecker, P.; Klockow, C.; Ellrott, A.; Quast, C.; Langhammer, P.; Harder, J.; Glöckner, F. O., Transcriptional response of the model planctomycete Rhodopirellula baltica SH1T to changing environmental conditions. BMC Genomics 2009, 10, 1-16.

144. Duncan, M. W.; Roder, H.; Hunsucker, S. W., Quantitative matrix-assisted laser desorption/ionization mass spectrometry. Briefings in Functional Genomics and Proteomics 2008, 7, 355-370.

145. Anderson, D. S.; Kirchner, M.; Kellogg, M.; Kalish, L. A.; Jeong, J.-Y.; Vanasse, G.; Berliner, N.; Fleming, M. D.; Steen, H., Design and Validation of a High-Throughput Matrix-Assisted Laser Desorption Ionization Time-of-Flight Mass Spectrometry Method for Quantification of Hepcidin in Human Plasma. Analytical Chemistry 2011, 83, 8357-8362.

146. Monica, H. E.; Derek, S. S.; Carol, E. P.; Christoph, B., Current trends in quantitative proteomics. Journal of Mass Spectrometry 2009, 44, 1637-1660.

147. Koeniger, S. L.; Talaty, N.; Luo, Y.; Ready, D.; Voorbach, M.; Seifert, T.; Cepa, S.; Fagerland, J. A.; Bouska, J.; Buck, W.; Johnston, R. W.; Spanton, S., A quantitation method for mass spectrometry imaging. Rapid Communications in Mass Spectrometry 2011, 25, 503-510.

148. Goodwin, R. J. A.; Mackay, C. L.; Nilsson, A.; Harrison, D. J.; Farde, L.; Andren, P. E.; Iverson, S. L., Qualitative and Quantitative MALDI Imaging of the Positron Emission Tomography Ligands Raclopride (a D2 Dopamine Antagonist) and SCH 23390 (a D1 Dopamine Antagonist) in Rat Brain Tissue Sections Using a Solvent-Free Dry Matrix Application Method. Analytical Chemistry 2011, 83, 9694-9701.

149. Landgraf, R. R.; Garrett, T. J.; Prieto Conaway, M. C.; Calcutt, N. A.; Stacpoole, P. W.; Yost, R. A., Considerations for quantification of lipids in nerve tissue using matrix-assisted laser desorption/ionization mass spectrometric imaging. Rapid Communications in Mass Spectrometry 2011, 25, 3178-3184.

150. Crossman, L.; McHugh, N. A.; Hseih, Y.; Korfmacher, W. A.; Chen, J., Investigation of the profiling depth in matrix-assisted laser desorption/ionization imaging mass spectrometry. Rapid Communications in Mass Spectrometry 2006, 20, 284-290.

151. Hatsis, P.; Brombacher, S.; Corr, J.; Kovarik, P.; Volmer, D. A., Quantitative analysis of small pharmaceutical drugs using a high repetition rate laser matrix-assisted laser/desorption ionization source. Rapid Communications in Mass Spectrometry 2003, 17, 2303-2309.

152. Persike, M.; Karas, M., Rapid simultaneous quantitative determination of different small pharmaceutical drugs using a conventional matrix-assisted laser desorption/ionization time-of-flight mass spectrometry system. Rapid Communications in Mass Spectrometry 2009, 23, 3555-3562.

153. Arnold, A.; Arrey, T. N.; Karas, M.; Persike, M., Fast quantitative determination of melamine and its derivatives by matrix-assisted laser desorption/ionization time-of-flight mass spectrometry. Rapid Communications in Mass Spectrometry 2011, 25, 2844-2850.

154. Persike, M.; Zimmermann, M.; Klein, J.; Karas, M., Quantitative Determination of Acetylcholine and Choline in Microdialysis Samples by MALDI-TOF MS. Analytical Chemistry 2010, 82, 922-929.

155. Blaze M.T., M.; Takahashi, L. K.; Zhou, J.; Ahmed, M.; Gasper, G. L.; Pleticha, F. D.; Hanley, L., Brominated tyrosine and polyelectrolyte multilayer analysis by laser desorption VUV postionization and secondary ion mass spectrometry. Analytical Chemistry 2011, 83, 4962-4969.

156. Gasper, G. L. MS Imaging of Antibiotics with Staph. epidermidis Bacterial Biofilms by Laser Desorption Postionization. Ph.D., University of Illinois at Chicago, Chicago, 2011.

157. Akhmetov, A.; Edirisinghe, P. D.; Hanley, L. In Quantitative proteomics via laser desorption photoionization mass spectrometry: Proof of principle study using iTRAQ tagging, Proceedings of the 59th ASMS Conference on Mass Spectrometry and Allied Topics, Denver, CO, June 5-9, 2011, 2011; Denver, CO, 2011; pp MP36, 586

158. Ghannoum, M.; O'Toole, G. A., Microbial Biofilms. ASM Press: Washington, D.C., 2004.

159. Sénéchal, A.; Catuogno, C.; Tabrizian, M., Quantification of initial adhesion of Enterococcus faecalis to medical grade polymers using a DNA-based fluorescence assay. Journal of Biomaterials Science: Polymer Edition 2005, 16, 112-126.

160. Kingshott, P.; Wei, J.; Bagge-Ravn, D.; Gadegaard, N.; Gram, L., Covalent attachment of poly(ethylene glycol) to surfaces, critical for reducing bacterial adhesion. Langmuir 2003, 19, 6912-6921.

161. Musk, D. J. J.; Hergenrother, P. J., Chemical countermeasures for the control of bacterial biofilms: Effective compounds and promising targets. Current Medicinal Chemistry 2006, 13, 2163-2177.

162. Aydin Sevinc, B.; Hanley, L., Antibacterial activity of dental composites containing zinc oxide nanoparticles. Journal of Biomedical Materials Research B 2010, 94B, 22-31.

163. Vasilev, K.; Sah, V.; Anselme, K.; Ndi, C.; Mateescu, M.; Dollmann, B. r.; Martinek, P.; Ys, H.; Ploux, L.; Griesser, H. J., Tunable Antibacterial Coatings That Support Mammalian Cell Growth. Nano Letters 2010, 10, 202-207.

164. Green, J.-B. D.; Fulghum, T.; Nordhaus, M. A., Review of immobilized antimicrobial agents and methods for testing. Biointerphases 2011, 6, MR13.

165. Rabea, E. I.; Badawy, E. T.; Stevens, C. V.; Smagghe, G.; Steurbaut, Chitosan as antimicrobial agent: Applications and mode of action. Biomacromolecules 2003, 4, 1457-1465.

166. Carlson, R. P.; Taffs, R.; Davidson, W. D.; Stewart, P. S., Anti-biofilm properties of chitosan-coated surfaces. Journal of Biomaterials Science: Polymer Edition 2008, 19, 1035-1046.

167. Fu, J.; Ji, J.; Yuan, W.; Shen, J., Construction of anti-adhesive and antibacterial multilayer films via layer-by-layer assembly of heparin and chitosan. Biomaterials 2005, 26, 6684-6692.

168. Anal, A.; Stevens, W., Chitosan-alginate multilayer beads for controlled release of ampicillin. International Journal of Pharmaceutics 2005, 290, 45-54.

169. Huang, J.-T.; Hannah-Qiuhua, L.; Szyszka, R.; Veselov, V.; Reed, G.; Wang, X.; Price, S.; Alquier, L.; Vas, G., Molecular imaging of drug-eluting coronary stents: method development, optimization and selected applications. Journal of Mass Spectrometry 2012, 47, 155-162.

170. Clemis, E. J.; Smith, D. S.; Camenzind, A. G.; Danell, R. M.; Parker, C. E.; Borchers, C. H., Quantitation of Spatially-Localized Proteins in Tissue Samples using MALDI-MRM Imaging. Analytical Chemistry 2012, 84, 3514-3522.

CURRICULUM VITA

MELVIN BLAZE MUTTIKAL THOMAS

SUMMARY:

Extensive experience in the area of method development and validation for the analysis of small molecules, antibiotics, metabolites and proteins in biological matrices, using state of the art separation and mass spectrometry techniques.

EDUCATION:

Ph.D., Analytical Chemistry, University of Illinois at Chicago, Chicago, Illinois, 2012

M.Sc., Analytical Chemistry, St. Joseph's College, Bangalore University, Bangalore, India, 2002

B.Sc., Physics, Chemistry and Mathematics, St. Joseph's College, Bangalore University, Bangalore, India, 2000

RESEARCH EXPERIENCE:

Graduate Research Assistant **Aug 2006 to present**
(University of Illinois at Chicago, Chicago, IL)

- *In situ* molecular imaging of small and large molecules in bacterial biofilms by matrix assisted laser desorption/ionization (MALDI-MS) and laser desorption post ionization mass spectrometry (LDPI-MS).
- Proteins and biomarker identification and imaging on intact bacterial biofilms by MALDI-MS and LDPI-MS.

Associate Research Scientist **Jan 2006 to Jul 2006**
(ADVINUS Therapeutics Pvt. Ltd, Bangalore, India)

- Initial setup of a functional GLP bioanalytical lab, installation of LCMS-MS and other analytical instruments for bioanalytical method development and validation.
- Writing SOP's for various instruments and experiments.
- HPLC and LCMS-MS Method development and validation for the quantification of drugs in human blood plasma for clinical pharmacokinetic studies.

Sr. Research Associate **Sep 2002 to Dec 2005**
(Aurigene Discovery Technologies Ltd, Bangalore, India)

- Purification and isolation of natural products from plant extracts by preparative HPLC.
- Identification, purification and characterization of New Chemical Entities (NCE's) and their metabolites by HPLC, LCMS-MS, FTIR and NMR.

- HPLC, LCMS-MS and extraction method development for the quantification of NCE's for preclinical Absorption, Distribution, Metabolism, Excretion and Toxicity studies (DMPK studies).
- HPLC and LCMS-MS method development for solubility, MDCK and Caco-2 permeability studies of NCE's.
- Metabolic stability studies by LCMS-MS with metabolite isolation by preparative HPLC and its characterization by LCMS-MS and NMR.
  LCMS-MS method development for cassette analysis of NCE's in preclinical pharmacokinetics studies.

CORE COMPETENCIES:

Instrumental Analysis:

- Extensive experience to apply state of the art analytical instruments LC-MS/MS, MALDI-MS, LDPI-MS, GC-MS, HPLC, FTIR, ATR-IR, NMR and UV-Vis instruments for efficient biomolecular and chemical analysis.

Chemical Analysis:

- Proficient in solvent-solvent extraction, protein precipitation, solid phase extraction, chemical tagging and purification by preparative HPLC.

Bacterial Cell Culture:

- Conversant with planktonic bacterial cell culture.
- Proficient in growing bacterial biofilm using drip flow bioreactor, membrane and static growth.

Software Skills:

- Proficient in ORIGIN (data analysis software), BioMap (MALDI-MS image analysis software), ChemStation, Analyst,, Millenium, MS fragmenter, ChemBioOffice, MS office, windows.

PUBLICATIONS:

1. **Melvin Blaze M.T.,** Artem Akhmetov, Berdan Aydin, Praneeth D. Edirisinghe, Gulsah Uygur, and Luke Hanley: Quantification of Antibiotic in Biofilm-Inhibiting Multilayers by 7.87 eV Laser Desorption Postionization MS Imaging. Submitted to **Analytical Chemistry**.
2. **Melvin Blaze M.T.,** Berdan Aydin, Ross Carlson, and Luke Hanley: Identification and Imaging of Peptides and Proteins on *Enterococcus Faecalis* Biofilms by Matrix Assisted Laser Desorption Ionization Mass Spectrometry. Submitted to **The Analyst**.
3. Slobodan Milasinovic, Yaoming Liu, Chhavi Bharadwaj, **Melvin Blaze M.T.,** Robert J. Gordon and Luke Hanley: Feasibility of Depth Profiling of Animal Tissue by Ultrashort Pulse Laser Ablation. **Analytical Chemistry 2012 (84) 3945**
4. **Melvin Blaze M. T.,** Lynelle K. Takahashi, Jia Zhou, Musahid Ahmed, Gerald L. Gasper, F. Douglas Pleticha, and Luke Hanley: Brominated Tyrosine and Polyelectrolyte Multilayer Analysis by Laser Desorption Vacuum Ultraviolet Postionization and Secondary Ion Mass Spectrometry. **Analytical Chemistry** 2011 (83) 4962

5. D.S Samiulla, V. V. Vaidyanathan, P. C. Arun, G. Balan**, M. Blaze**, *et.al*: Rational Selection of Structurally Diverse Natural Product Scaffolds with Favorable ADME Properties for Drug Discovery. **Molecular Diversity** 2005 (9) 131.

PRESENTATIONS:

1. 7.87 eV Laser Desorption Postionization MS Imaging to Quantify Small Molecule Antibiotics on Intact Colony Biofilms. **Melvin Blaze M.T.,** Chhavi Bhardwaj, and Luke Hanley.
Poster presentation: 60th ASMS Conference on Mass Spectrometry and Allied Topics. Vancouver, Canada. (May 2012)

2. *In-situ* tryptic digestion of bacterial biofilm for protein identification and imaging by MALDI –MS. **Melvin Blaze M. T**., Berdan Aydin and Luke Hanley.
Poster presentation: 59th ASMS Conference on Mass Spectrometry and Allied Topics. Denver, Colorado. (May 2011)

3. Ionization energy lowering in clustered species demonstrated by tunable photon energy LDPI-MS. **Melvin Blaze M. T**., Lynelle K.T., Jia Z., Musahid A., Gerald G., and Luke Hanley.
Poster presentation: 58th ASMS conference on mass spectrometry and Allied Topics. Salt Lake City, Utah. (June 2010)

4. Alginate-chitosan multilayer film with bound antibiotic as a model system for depth profiling by C60+ ion sputtering. Melvin Blaze M. T., F. Douglas. P and Luke Hanley.
Poster presentation: Pittcon. Chicago, Illinois. (March 2009)